2009-08-12

# Experimental Characterization of Flow Induced Vibration in Turbulent Pipe Flow

Andrew S. Thompson
*Brigham Young University - Provo*

BYU ScholarsArchive Citation

Thompson, Andrew S., "Experimental Characterization of Flow Induced Vibration in Turbulent Pipe Flow" (2009). *All Theses and Dissertations*. 1906.
https://scholarsarchive.byu.edu/etd/1906

# EXPERIMENTAL CHARACTARIZATION OF FLOW INDUCED VIBRATION IN TURBULENT PIPE FLOW

by

Andrew S. Thompson

A thesis submitted to the faculty of
Brigham Young University
in partial fulfillment of the requirements for the degree of

Master of Science

Department of Mechanical Engineering
Brigham Young University
December 2009

BRIGHAM YOUNG UNIVERSITY

# GRADUATE COMMITTEE APPROVAL

of a thesis submitted by

Andrew S. Thompson

This thesis has been read by each member of the following graduate committee and by majority vote has been found to be satisfactory.

| | |
|---|---|
| Date | R. Daniel Maynes, Chair |
| Date | Jonathan D. Blotter |
| Date | Julie Vanderhoff |

BRIGHAM YOUNG UNIVERSITY

As chair of the candidate's graduate committee, I have read the thesis of Andrew S. Thompson in its final form and have found that (1) its format, citations, and bibliographical style are consistent and acceptable and fulfill university and department style requirements; (2) its illustrative materials including figures, tables, and charts are in place; and (3) the final manuscript is satisfactory to the graduate committee and is ready for submission to the university library.

| | |
|---|---|
| Date | R. Daniel Maynes<br>Chair, Graduate Committee |

Accepted for the Department

Larry L. Howell
Graduate Coordinator

Accepted for the College

Alan R. Parkinson
Dean, Ira A. Fulton College of Engineering
and Technology

# ABSTRACT

## EXPERIMENTAL CHARACTARIZATION OF FLOW INDUCED VIBRATION IN TURBULENT PIPE FLOW

Andrew S. Thompson

Department of Mechanical Engineering

Master of Science

This thesis presents results of an experimental investigation that characterizes the wall vibration of a pipe with turbulent flow passing through it. Specifically, experiments were conducted using a water flow loop to address three general phenomena. The topics of investigation were: 1) How does the pipe wall vibration depend on the average flow speed, pipe diameter, and pipe thickness for an unsupported pipe? 2) How does the behavior change if the pipe is clamp supported at various clamping lengths? 3) What influence does turbulence generation caused by holed baffle plates exert on the pipe response?

A single pipe material (PVC) was used with a range of internal diameters from 5.08 cm to 10.16 cm and diameter to thickness ratios ranging from 8.90 to 16.94. The

average flow speed that the experiments were conducted at ranged from 0 to 11.5 m/s. Pipe vibrations were characterized by accelerometers mounted on the pipe wall at several locations along the pipe length. Rms values of the pipe wall acceleration and velocity time series were measured at various flow speeds. Power spectral densities of the accelerometer data were computed and analyzed. Concurrent wall pressure fluctuation measurements were also obtained.

The results show that for a fully developed turbulent flow, the rms of the wall pressure fluctuations is proportional to the rms of the wall acceleration and each scale nominally as the square of the average fluid velocity. Also, the rms of the pipe wall acceleration increases with decreasing pipe wall thickness. When changes were made in the pipe support length, it was observed that, in general, pipe support length exercises little influence on the pipe wall acceleration. The influence of pipe support length on the pipe wall velocity is much more pronounced. A non-dimensional parameter describing the pipe wall acceleration is defined and its dependence on relevant independent non-dimensional parameters is presented.

Turbulence was induced using baffle plates with various sizes (2.54 cm to 0.159 cm) and numbers of holes drilled through them to provide a constant through area of 35.48 $cm^2$ for each plate. Cavitation exists at high speeds for the largest holed baffle plates and this significantly increases the rms of the pipe wall acceleration. As the baffle plate hole size decreases, vibration levels were observed to return to levels that were observed when no baffle plate was employed. Power spectral densities of the accelerometer data from each baffle plate scenario were also computed and analyzed.

# ACKNOWLEDGMENTS

I came to Dr. Daniel Maynes as a physics undergraduate student to advise me as I completed my final project. While working with him, Dr. Maynes informed me of this project and that he was looking for a prospective graduate student to work on it. I accepted and have thoroughly enjoyed what I have been able to learn through the course of completing this thesis. I would like thank to Dr. Maynes for giving me this opportunity. And also for essentially giving me the reigns of this work; which, under his guidance, allowed me to gain knowledge, experience, and confidence that I would not have been able to gain any other way.

I would also like to thank Dr. Jonathan Blotter for adding his time, direction, expertise, and equipment which also made it possible to complete this project and to understand what some of the data were saying. To Dr. Julie Vanderhoff, thank you for being willing to be a part of my committee when I just asked out of the blue. Also, I would like to thank Genscape Inc. and Control Components Inc. for their interest in this project and for the funding that made it possible.

Finally, I would like to thank my wife Nicole for the patience and love she has given me as I have completed my thesis. She has always been very supportive of my endeavors and I do not think I could have succeeded without her encouragement.

TABLE OF CONTENTS

# LIST OF TABLES

# LIST OF FIGURES

# 1 Introduction

Conveying fluids through pipes has been a very important aspect of human civilization for thousands of years. In recent decades transporting gas, water, oil and other fluids has made many economic activities possible. However, in the U.S. about 60% of the pipelines have been in use for over 25 years and are becoming prone to failure [1]. One of the contributing sources of failure in pipe systems is loss of integrity due to fatigue loading caused by excessive vibration [2]. One example of this occurred on January 27, 2000. At about 12:12 p.m. a Marathon Ashland pipe ruptured near Winchester, Kentucky releasing 11,644 barrels of crude oil onto a golf course and into nearby Two Mile Creek. A post-accident investigation determined that its probable cause was fatigue cracking due in part to fluctuating pressures within the pipe, Fig. 1-1 [3].

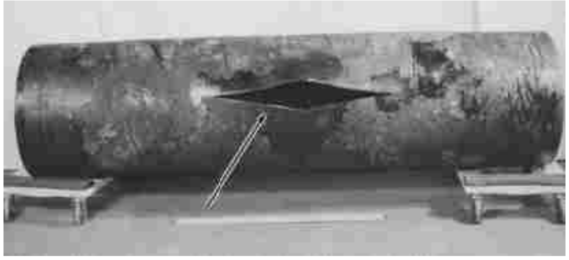

**Figure 1-1: Photograph of the ruptured pipe from the NTSB accident brief. The arrow indicates the rupture site [3].**

It has been well documented that pipe vibration levels increase as the flow dynamic pressure increases [2]. A dependency of flow rate on the induced vibration levels has also been observed [2]. Experimental and numerical techniques have been used by several research groups to try to investigate this dependency with varying success. Although each investigation has yielded different results, each has also concluded that pipe vibration is a direct result of the inherent spatially and temporally varying pressure at the pipe wall [2].

Although vibrations can lead to unwanted consequences, the monitoring of vibration levels can also be used to provide non-intrusive flow sensing. Several types of flow sensors have been developed over the centuries, with the earliest being developed over 2100 years ago as simple siphon tubes attached to a constant head reservoir [4]. More modern flow sensors include, among others, orifice and venturi meters, flow nozzles, vortex shedding meters, turbine meters, and Coriolis flow meters. These types of sensors require interrupting the flow, which, for some applications, is not always possible. A non-intrusive flow sensing technique has been expressed by several researchers and has broad application throughout industry [2, 5, 6]. As a specific example, Genscape Inc., a provider of energy generation and transmission data to energy traders, power plant and pipe line owners and operators, and regulatory agencies, monitors gas and oil flows which help energy traders develop market/price forecasting models, determine supply and demand tightness in regional markets, understand price drivers, and provide flow data in U.S. pipelines [7]. As a third party entity, it is not permissible for them to potentially compromise a pipe’s structural integrity by installing and maintaining intrusive flow sensors; so a non-intrusive flow sensing technique would allow them to provide the necessary data to their customers without compromising the infrastructure. Non-intrusive techniques could also be used to characterize the stresses and loading in a piping system to predict catastrophic failures, such as the January 2000 accident, or monitor the flow of corrosive substances that would quickly render an intrusive flow sensor inoperable [2].

## 1.1 Objective

The objective of this research was to characterize the pipe wall vibrations caused by fully-developed turbulent pipe flow. The influence of pipe diameter and thickness, and pipe length was also explored. This was done by conducting an experimental study that utilized pipe-wall mounted accelerometers and pressure transducers to determine the relationship between these factors. Specifically, pressure fluctuation and vibration level measurements were made in various diameters and thicknesses of PVC pipe with several clamping support distances. Also, pipe vibration measurements due to different levels of induced turbulence were conducted by inserting baffle plates into the flow field.

## 1.2 Hypothesis

It is clear that understanding how pipe vibration levels depend on flow dynamics and pipe characteristics is important. According to other studies, the characteristic vibration level, *A’*, which is defined as the standard deviation of the pipe acceleration time series, can be expressed as [8]:

$$A' = f(V_f, D, t, L, \rho_f, \rho_p, E, \ldots) \tag{1-1}$$

Where $V_f$ is the average fluid velocity, $D$ is the internal pipe diameter, $t$ is the pipe thickness, $L$ is the pipe length, $\rho_f$ is the fluid density, $\rho_p$ is the pipe density, and $E$ is the modulus of elasticity of the pipe. As previously stated, vibration levels have been observed to increase with increased dynamic pressure ($\rho_f V_f^2$). Because dynamic pressure is a function of fluid velocity, it is expected that vibration levels will increase as the square of the fluid velocity and flow rate. Because surface area increases with *D*, it is also expected that vibration levels will increase as pipe diameter increases. As pipe thickness decreases, it expected that vibration levels will increase because the pipe walls should be able to respond more easily to changes in the local dynamic pressure. Because changes in the pipe support length can affect the natural response of the pipe, it is expected that this parameter will also affect the vibration levels, but will not have as strong of an influence as the previously described parameters. Finally, because baffle plates are designed to induce turbulence in the flow, they are expected to increase vibration levels.

## 1.3 Scope and Thesis Outline

Pipe vibration levels were quantified for average fluid speeds ranging from 0 -11.5 m/s, with water as the working fluid. Flow through schedule 40 and 80 PVC pipe test sections of diameters 5.08 cm -10.16 cm and diameter to thickness ratios ranging from 8.9 -16.9 were characterized. These results are compared to a similar study conducted at Idaho State University. The effects on pipe vibration levels due to wall mounted clamp supports of varying distances was also investigated. Finally, the effects of baffle plates of varying hole size, inserted into the flow, was examined.

Because only one fluid and pipe material was examined in this study, dependency of vibration levels on pipe density, fluid density, and pipe modulus of elasticity was not addressed. Also, the range of available pipe diameters and thicknesses is limited to standard sizes and one cannot be changed without also changing the other. Thus, the individual influence of these two parameters individually is somewhat confounded.

The remainder of this thesis is organized as follows:

Chapter 2 contains a literature review and background information. It describes how vibration levels are expected to scale with influential variables. Literature that describes turbulent external flow past cylinders and of internal turbulent flow in pipes is reviewed. Finally, the results of a similar study done at Idaho State University will be summarized.

Chapter 3 details the experimental facility and experimental process.

Chapter 4 presents the results of the experiments performed.

Chapter 5 summarizes the conclusions of this research and discusses possible areas of future research.

# 2 Background

This chapter details previous work that has been conducted to characterize flow induced vibrations. First, a summary of work done on external turbulent flow past cylinders is described. It will be seen that some of the results are applicable to internal pipe flow and are discussed in Section 2.1. Next, work focusing on internal pipe flow will be reviewed and is contained in Section 2.2. Section 2.3 considers how turbulence induced pipe vibrations are expected to scale with flow and pipe characteristics. Finally, section 2.4 will give a detailed review of a similar study done at Idaho State University.

## 2.1 External Turbulent Flow Past Cylinders

Related work, which has relevance in the nuclear power industry, has explored external turbulent flow past cylindrical rods with the flow direction aligned with the rod axis. In a work by Paidoussis [9], the behavior of cylinders in both cross flow and axial flow are described. Paidoussis states that the behavior of an array of cylinders in cross flow exhibit three main characteristics; first, at low flow velocities is responding chiefly to turbulent buffeting; observing that as fluid velocity increases, the vibration level increases as the fluid velocity squared. Then as the flow velocity continues to increase, a peak develops as the cylinders respond to such phenomenon as vortex shedding and resonance. Finally, as the flow velocity continues to increase, a fluid elastic instability develops and the cylinders are expected to respond with large amplitude motions.

Turbulent fluid flow, which is made up of eddies of various sizes and energies, coupled with the flow periodicity that results as a fluid moves around a cylinder set up forced vibrations in the cylinder. These forced vibrations are made up of non-resonant components that are present at all flow velocities and resonant components that exist in the frequency band near the cylinders' natural frequency. In the resonant frequency band, the cylinders extract energy from the fluctuating pressure field near the cylinders [9]. Others [9] found that away from the resonant frequency band, the cylinders response was proportional to the fluid velocity squared, as stated above.

Addressing axial flow around cylinders, Paidoussis states that vibrations observed below the threshold of fluid elastic instabilities are also widely accepted to be caused by pressure fluctuations in the flow field, similar to cylinders in cross flow. These pressure fluctuations are made up of near and far field components with the near field consisting of local pressure fluctuations associated with the boundary layer and the far field consisting of acoustic disturbances. It is also shown that cylinders in axial flow respond in a similar fashion to cylinders in cross flow, *i.e.*, responding proportionally to the fluid velocity squared except near the resonant frequency band and above the fluid elastic instability.

In a work by Reavis [10], the author calculates the response of fuel elements in parallel flow making use of experimental data from Burgreen *et al.* [10] and empirical correlations derived via dimensional analysis of beam motion by Burgreen and

Paidoussis [10]. The available data described the pressure fluctuations in a turbulent boundary layer. Similar to the works described above, the fuel element's response is forced by the fluctuating pressure field in the turbulent boundary layer.

These previous works show that the vibration response of cylinders placed in turbulent flow is due to the pressure fluctuations in the boundary layer. They also show the vibration levels are proportional to the average fluid velocity squared. Though not discussed in detail here, the correlations mentioned above include average fluid velocity, rod diameter, fluid density, and mass per unit length of the rod as dependant variables[10]. Similar factors are also expected to be important in turbulent flow through pipes.

## 2.2 Internal Turbulent Pipe Flow

### 2.2.1 Pipe Flow Characteristics

Fully developed turbulent pipe flow is made up of eddies and vortices of various sizes, ranging from the same order of magnitude as the inner pipe diameter to the Kolmogorov scale. The turbulent kinetic energy contained in the eddies increases with flow velocity, resulting in greater pressure fluctuations [2]. The largest eddies are the result of whatever mechanism is responsible for the turbulence generation (*i.e.* wall shear, jets, *etc*) [10]. Here the transfer of energy is from the mean flow to the large eddies [2]. These large eddies are also the most energetic and transfer their energy into smaller eddies which in turn transfer energy to smaller eddies, until dissipation takes place at the Kolmogorov scale (the smallest turbulent length and time scales) [2, 10]. This all takes place within the boundary layer, which for fully developed pipe flow is across the entire inner pipe diameter. Because these fluid packets have various amounts of kinetic energy, as they approach the pipe wall the energy is converted into another form. Some portion is converted into heat, but most of it is converted into pressure and pressure fluctuations, a form of potential energy [5].

Calculating the power spectral density, PSD, of the turbulent field reveal structures that are common for a wide range of turbulent flows. Figure 2-1 illustrates the spectral decay in a region known as the inertial subrange (the red line) where $E_{11}$ is the energy spectrum function, $k_1$ is wave number and is related to frequency by the fluid velocity, $\varepsilon$ is the rate of energy dissipation, $v$ is the kinematic viscosity, and $\eta$ is the Kolmogorov scale. As hypothesized by Kolmogorov, turbulent energy in the inertial subrange cascades from large scales (low frequencies) to small scales (high frequencies) without significant production or dissipation [12]. In the inertial subrange, the wave number extent increases with Reynold's number and decays as $k_1\eta$ [13, 12, 14]. Also, because wave number is related to frequency ($f$) by the fluid velocity, the frequency extent in the inertial subrange will decay as $f^{-5/3}$. Although the -5/3 relationship is pervasive through turbulent research, the cascade explanation has come with some criticism because among other things the -5/3 law has never been able to be extracted from the Navier-Stokes equations [15]. Even with arguments against it, the -5/3 relationship is supported experimentally in many types of turbulent flows. It will be expected that for the results presented in this thesis, there should also be a -5/3 roll-off in the PSD of the pipe vibrations, due to their proportionality to the pressure fluctuations.

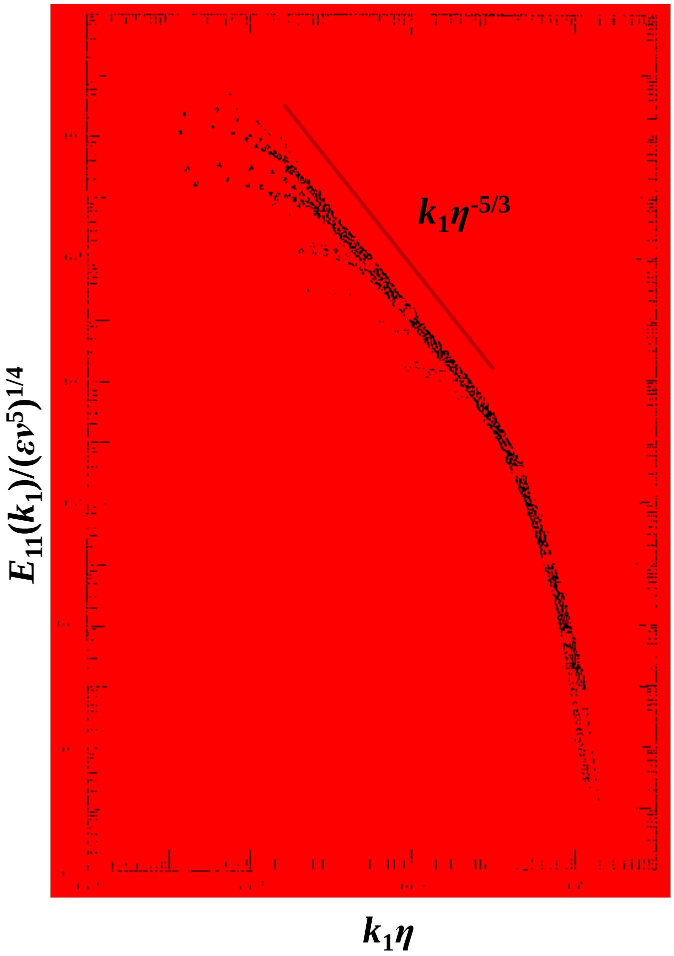

**Figure 2-1: -5/3 power law roll-off in inertial subrange of various turbulent flows. The horizontal axis represents the non-dimensional frequency and the vertical axis represents the non-dimensional PSD [13].**

A work by Evans *et al.* [5] shows how the turbulence induced pipe vibrations relate to the pressure fluctuations in the fluid for the purpose of developing a non-intrusive flow sensing technique. The analysis by Evans *et al.*[5] is based on a 1-D model of a beam in bending. The result of this analysis demonstrates that the pipe vibrations are proportional to the pressure fluctuations. Also demonstrated is that the square of the fluctuations in flow rate are proportional to the pressure fluctuations, which leads to the implication that the standard deviation of the pipe vibrations is proportional to the average flow rate squared.

Utilizing the quadratic relationship between flow rate and pipe vibrations, Awawdeh, *et al.* attempt to develop a sensor network to monitor changes in pipe flow rate[1]. Using a wireless sensor network to collect data, accelerometers were attached to 10.82 cm inner diameter water conveying steel pipes. Time series vibration data were collected at no flow and two other flow rates. It is shown that changes in flow rate can be tracked non-invasively using accelerometers mounted on the pipe wall [1]. The experimental setup for this study did not describe vibration isolation of the test section from other vibration sources and thus may be subject to other sources of signal noise.

Kim and Kim developed a method for measuring flow rate in a pipe by utilizing an external exciter and three accelerometers [6]. The accelerometers were placed equal distances from each other along the length of 3 cm inner diameter, steel, water conveying pipe. The pipe was excited with white noise up to 55 kHz with a shaker and the system was run at four flow rates from 0 to 3.08 L/s. The effects of the moving internal fluid through the shaker excited pipe caused a shift in the axial wave number (Doppler shift) that was converted to flow rate. A Gaussian fit was applied to the histogram of each measurement configuration at discrete frequencies and then compared to the histogram of the actual flow rate, and it was found that the Gaussian fits coincided with the actual flow rates within 12% uncertainty [6]. The experimental setup used for this thesis differs from the work done by Kim. Specifically, the pipe is not excited by white noise and the accelerometers are not positioned as described by Kim. However, this thesis does show that there is a coupling between internal pipe flow and pipe vibration that can be utilized as a non-intrusive flow sensing technique.

### 2.2.2 Orifice Induced Vibrations

Large amplitude vibrations were observed in particular flow regimes in a French nuclear power plant. These unwanted vibrations were attributed to cavitation induced by single hole orifices. Conducting experiments to try to explain and reduce the large amplitude pipe vibrations Caillaud *et al.* found that the vibrations were caused by supercavitation at the orifice, significantly disturbing the flow [16].

Qing *et al.* studied orifice induced wall pressure fluctuations and pipe vibrations[17]. The study was performed by mounting accelerometers and dynamic pressure transducers before and after an orifice plate to measure structural vibrations and wall pressure fluctuations. The pipe was 9.0 cm internal diameter stainless steel, and three orifice plates were used, with orifice diameters of 2.3 cm, 2.74 cm, and 3.02 cm (a no orifice plate condition was also used). Three flow rates were investigated, which translated into flow speeds of 0.65 m/s, 0.87 m/s and 1.09 m/s. The root mean square (rms) and power spectral density (PSD) of the pressure measurement time series were then calculated. It was found that without an orifice plate the rms of the pressure fluctuations remained nearly the same at each measurement point. Adding an orifice plate results in a sharp rise in the rms values of the fluctuating pressure, indicating that the flow is significantly disturbed by the orifice plates. Figure 2-2 illustrates the non-dimensionalized PSD vs. Strouhal number ($St = fD/V_f$, where $f$ is frequency, $D$ is inner pipe diameter, and $V_f$ is fluid velocity) 1.7 pipe diameters downstream from the 3.02 cm orifice, where the maximum pressure fluctuations were observed to occur. As the flow passes through the orifice, the flow contracts and re-expands downstream. An eddy was found to appear on the backside of the orifice due to cavitation. The PSD shows that the flow's energy content is below 400 Hz, $St \approx 6.2$, and is concentrated below 71 Hz, $St \approx 1.1$. Further downstream less energy is concentrated in this low frequency range, and the rms drops to nearly the same level as the no orifice condition, indicating that the orifice disturbance is localized to the vicinity of the orifice plate [17].

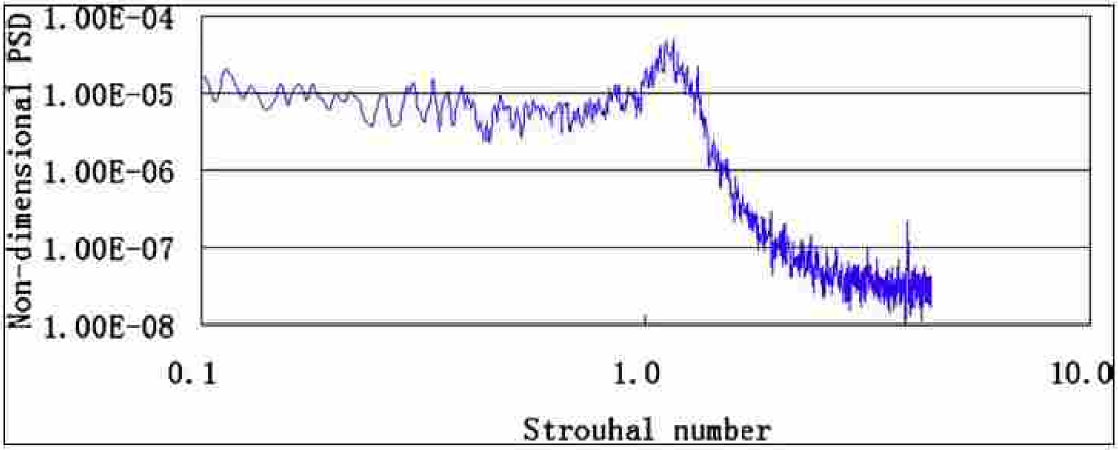

**Figure 2-2: Non-dimensionalized PSD 1.7 pipe diameters downstream from an orifice plate [17].**

The goal of a subsequent work by Qing was to develop empirical equations of the fluctuating pressure PSD [18]. The results conclude that cavitation can be avoided by increasing the hole size of the orifice plate, but the induced pressure fluctuations, which stimulate pipe vibration, cannot be eliminated. Also, the near field turbulence caused by the localized disturbance affects the flow up to six pipe diameters downstream. Finally, pressure fluctuations increase as flow rate increases or as the diameter of the orifice hole decreases [18].

In contrast to the works by Qing *et al.* [17, 18], in this thesis baffle plates with multiple holes were used to induce turbulence over a significantly larger range of flow speeds and multiple pipe diameters. It is expected however, that cavitation will be caused by the baffle plates and that pressure fluctuations, and by extension pipe vibrations, will increase dramatically. It is also expected that the PSD will behave in a similar fashion to Fig. 2-2, with the majority of the energy below 400 Hz.

A study by Moussou provided an estimation of the vibrations of a water conveying pipe subjected to orifice plate induced turbulent excitations [19]. It was shown that the cavitation induced vibrations can be directly identified by plotting the dimensionless pipe vibration PSD. Specifically, cavitation adds a broad increase to the spectrum with an amplitude that depends on the incipient cavitation [19]. This localized increase may be similar to the hump observed in Fig. 2-2 and is expected in the baffle plate experiments performed for this thesis.

## 2.3 Scaling Relations

Evans showed that the standard deviation of the pipe vibrations scaled as the standard deviation of the pressure fluctuations ($A' \sim P'$) [5]. It was also stated that kinetic energy in the flow was converted into dynamic pressure near the wall. Referring to the definitions of kinetic energy and dynamic pressure respectively:

$$E_k \sim \frac{1}{2} m V_f^2 \tag{2-1}$$

$$P \sim \frac{1}{2}\rho V_f^2 \qquad (2\text{-}2)$$

in the above expressions $m$ is mass, $V_f$ is fluid velocity, and $\rho$ is fluid density. The dynamic pressure has units of kinetic energy per unit volume and it would be expected that the dynamic pressure fluctuations of the flow are proportional to the kinetic energy which goes as $V_f^2$, implying that $A' \sim V_f^2$.

Contained in Appendix C is a document by Maynes[20] that presents a scale analysis of turbulence induced pipe vibration in a straight pipe for both the pipe bending and expansion modes. The portion describing the scaling of the bending mode of pipe vibration is summarized here for convenience.

Because turbulent pipe flow induces pressure fluctuations at the pipe wall, these pressure fluctuations can be thought of as a loading function which causes deflection fluctuations in an elastic beam. The standard deviation of the deflection fluctuations ($\delta'$) should scale as

$$\delta' \sim \frac{F' L^3}{EI} \qquad (2\text{-}3)$$

With the unsteady loading represented by $F'$, $L$ is the pipe length between supports, $E$ is the modulus of elasticity, and $I$ is the area moment of inertia. The loading $F'$ should scale with $P'$ multiplied by a characteristic area, $D^2$, where $D$ is the inner pipe diameter. Further, $P'$ should scale as the flow dynamic pressure as defined in Eq. 2-2. Substituting this relationship into Eq. 2-3 gives

$$\delta' \sim \frac{\rho V_f^2 D^2 L^3}{EI} \tag{2-4}$$

Fluctuations in the velocity of the pipe wall are expected to scale as δ’ (Eq. 2-4) multiplied by the natural frequency of vibration of a pipe given by

$$\omega_n \sim \frac{1}{L^2}\sqrt{\frac{EI}{m}} \tag{2-5}$$

Where $m$ is the mass per unit length of the contained fluid and of the pipe, $m = \rho A + m_{pipe}$, and $A$ is the internal cross sectional area of the pipe. Multiplying Eq. 2-4 by Eq. 2-5 gives the scaling relationship for the pipe velocity fluctuations, $V_p$’

$$V_p' \sim \left(\frac{V_f^2}{\sqrt{\frac{E}{\rho}}}\right)\left(\sqrt{\beta}\right)\left(\frac{DL}{\sqrt{I}}\right) \tag{2-6}$$

Here $\beta$ is the ratio of fluid mass per unit length to total mass per unit length of the combined fluid and pipe defined as

$$\beta = \frac{1}{1 + \frac{\rho_p}{\rho}\left(\frac{4t}{D}\left(1 + \frac{t}{D}\right)\right)} \tag{2-7}$$

$t$ is the pipe wall thickness and $\rho_p$ is the density of the pipe material. By inspection, it can be seen that $\beta$ scales to the first order as $D/t$. Finally, multiplying Eq. 2-6 by Eq. 2-5 gives the fluctuations of pipe wall acceleration $A$’

$$A_p' \sim \frac{V_f^2 \beta}{L} \tag{2-8}$$

A similar scale analysis for the expansion modes yields [21]

$$A_p' \sim \frac{V_f^2 \beta}{D} \tag{2-9}$$

The analysis suggests that $\delta'$, $V'$, and $A'$ should scale with $V_f^2$ for both modes considered. As stated in Chapter 1 the influence of changing only pipe diameter without changing any other parameters is not possible, but Eqs. 2-8 and 2-9 suggest that $A'$ should scale with $\beta$ and $V'$ should scale as $\sqrt{\beta}$. The relations presented here will be compared to the experimental results of Pittard *et al.* in the next section.

## 2.4 Comparison of Scaling Relations to Experimental Data

Pittard *et al.* presented results of a study intended to explore the strong correlation between flow rate and measured pipe vibration [2]. The experimental portion of the study was done at Idaho State University (ISU) using a flow loop similar to the one that will be described in Chapter 3. Experiments were conducted in pipes of three different materials; PVC, aluminum, and stainless steel. A description of these pipe sections is contained in Table 2-1. Accelerometers were placed on the pipe wall and the standard deviation of the frequency averaged time series was measured at various flow rates. A characteristic of the ISU study that differentiates it from what will be presented in this thesis is that different pipe materials were used with a wide range of pipe densities (1400, 2200, and 7800 kg/m$^3$ for PVC, aluminum and stainless steel respectively) and moduli of elasticity (2.9,70, and 200 GPa respectively). Flow rates ranged from 0.0033 m$^3$/s to 0.025 m$^3$/s, resulting in a range of velocities from 0.4 m/s to 13.3 m/s.

**Table 2-1: Pipe material, diameters, and wall thicknesses for data of Pittard, *et al*[3].**

| **Pipe Section** | **Material** | ***D(m)*** | ***t(m)*** | ***D/t*** |
|---|---|---|---|---|
| **10.16 cm Sch** | PVC | 0.102 | 0.00602 | 16.94 |
| **7.62 cm Sch** | PVC | 0.0779 | 0.00548 | 14.22 |
| **7.62 cm Sch** | Aluminum | 0.0779 | 0.00548 | 14.22 |
| **7.62 cm Sch** | Stainless | 0.0779 | 0.00548 | 14.22 |
| **3.81 cm Sch** | Stainless | 0.041 | 0.00368 | 11.14 |

Figure 2-3 shows the standard deviation of the pipe vibration measured by an accelerometer, *A'*, as a function of $V_f$ (top panel) and average flow rate, *Q*, (bottom panel) and Fig. 2-4 shows the standard deviation of the pipe velocity, *V'*, as a function of $V_f$ (top panel) and *Q* (bottom panel)[3]. The results shown in these two figures suggest a power law dependence of *A'* and *V'* on $V_f$ (i.e. $Z' \sim V_f^m$, where *Z'* represents the respective variable of interest). A statistical analysis of the data reveals that for the *A'* data, *m* varies between 1.90 and 2.30 with an average of 2.16. This value is slightly greater (~8%) than the quadratic relationship predicted by Eqs. 2-8 and 2-9[2]. For *V'*, *m* varies from 1.61 to 1.75 with an average of 1.68. The values of *m* are the same when the data are plotted versus *Q*. Figures 2-3 and 2-4 also give a limited characterization of the combined influence of *D/t*. Specifically, the magnitude of *A'* when plotted as a function of $V_f$ is greater for the 10.16 cm PVC than for the 7.62 cm PVC pipe sections. This is also evident in the 7.62 and 3.81 cm stainless steel sections. This relationship is reversed when *A'* is plotted as a function of *Q*.

The data shown in Figs. 2-3 and 2-4 also suggest that the pipe vibration exhibit only a very modest dependence on the pipe material properties, $\rho_p$ and *E*. The data in the figures show only small variations between the 7.62 cm PVC, aluminum, and stainless steel pipe sections. The general trend shown in the data is that *A’* increases only modestly with decreased pipe density and/or modulus. An analysis done by Evans *et al.* [12] on the same pipe diameters and materials show that the properties of the pipe materials change the slope of *A’* when plotted vs. *Q*. Specifically, as $\rho_p$ and *E* increase, the slope of the *A’* curve is observed to decrease modestly. It is also indicated that the *D* dependence is not constant over the range of *Q*.

It is expected that the data presented in Chapter 4 will behave in a fashion similar to the data acquired at ISU. Specifically *P’* and *A’* are expected to scale with $V_f^2$ and *V’* is expected to scale nominally with $V_f^{1.6}$. Also, *A’* is expected to decrease as *D* increases when plotted as a function of $V_f$.

To summarize, the literature reviewed above concludes that vibrations of cylindrical rods placed in turbulent flow are due to fluctuating pressure loading. For internal pipe flow, the PSD of the turbulence energy decays as frequency to the -5/3 power in the inertial subrange. *P’* is proportional to *A’* which also scales as $V_f^2$ and this general relationship makes it possible to predict flow rate by measuring the pipe vibrations. It was also noted that *A’* decreases as *D* increases over the range of flow rates previously explored. Finally, the presence of an orifice plate produces turbulent disturbances that cause significant increases in *A’* and *P’*.

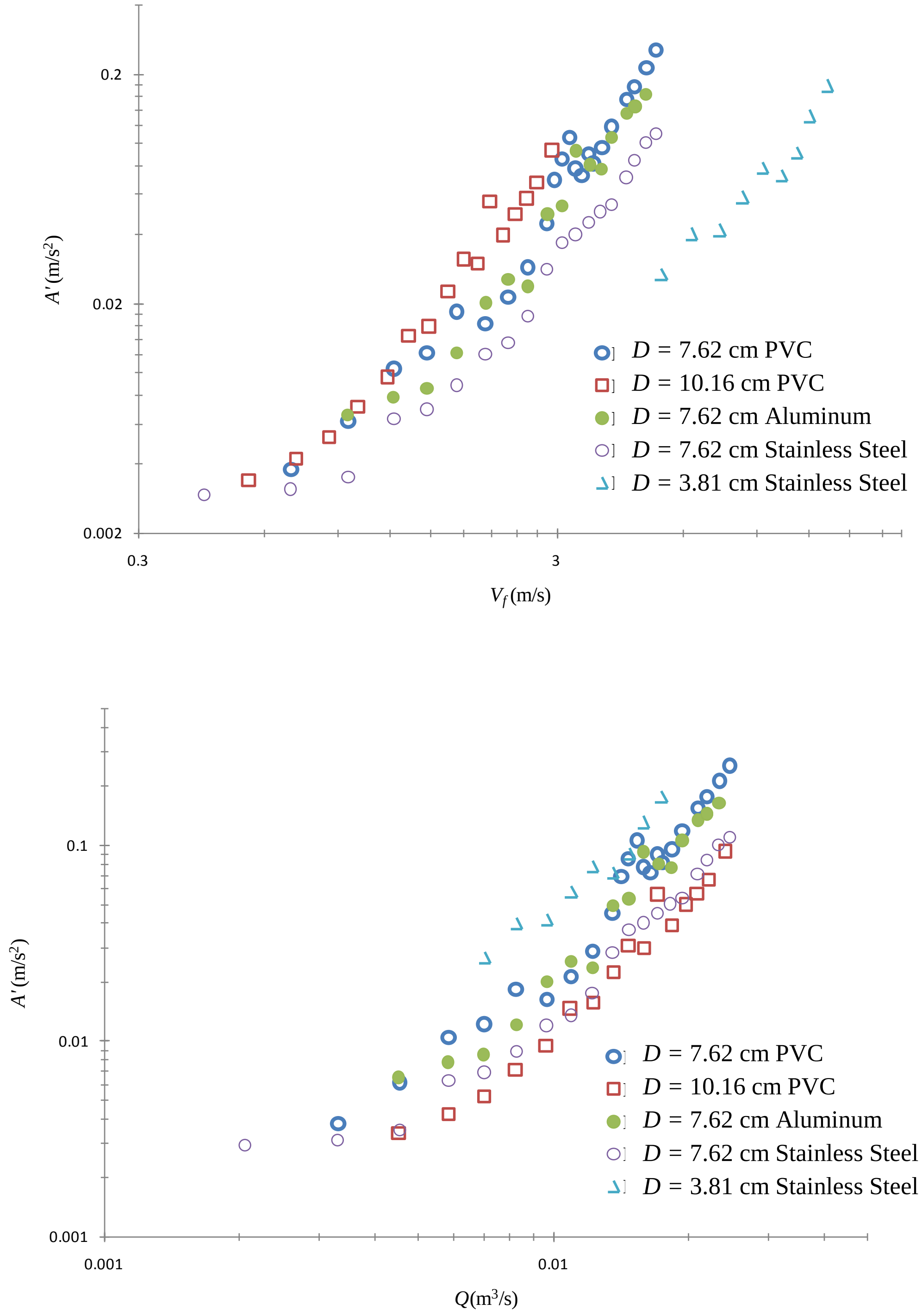

**Figure 2-3: $A'$ measured in m/s$^2$ as a function of $V_f$ (top panel) and $Q$ (bottom panel) for flow through five pipes of varying material and diameter as shown in the figure legends. Data obtained from Pittard, *et al.* [2].**

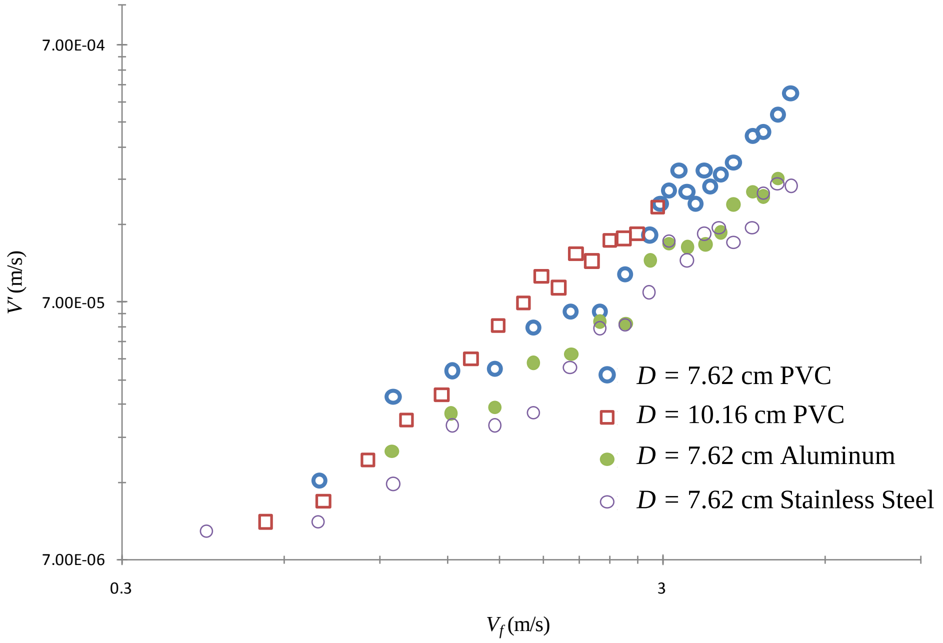

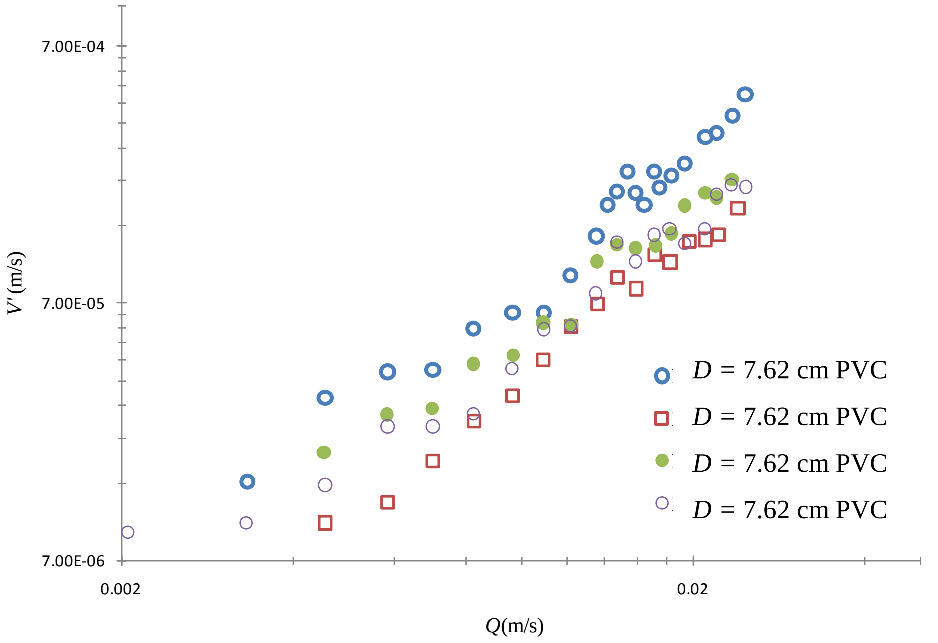

**Figure 2-4: $V'$ measured as a function of $V_f$ (top panel) and $Q$ (bottom panel) for flow through four pipes of varying material and diameter as shown in the figure legends. Data obtained from Pittard, *et al.* [3].**

## 2.5 Contributions

This work will result in the following contributions:

1. The dependency between wall acceleration (*A'*) and wall surface pressure fluctuations (*P'*) will be determined by direct measurement of each parameter.
2. rms values of the pipe wall acceleration and velocity will be characterized over a wide range of water speeds (0-11.5 m/s) and will provide greater understanding of the dependence of each of these parameters on the average flow speed. Previous studies have generally only focused on pipe wall acceleration.
3. The dependency of pipe diameter and thickness will be explored by considering flow through six pipes (5.08 cm, 7.64 cm, and 10.16 cm Schedule 40 and 80 pipes). The number of pipe sizes is larger than most previous studies and will provide greater understanding of the dependence of the rms values of the pipe wall acceleration and velocity on the pipe diameter and wall thickness.
4. The influence of varying the clamping length of the pipes of interest on the pipe acceleration will be characterized by conducting experiments with the pipes clamped at discreet points.
5. The influence of baffle plates of varying hole size on the vibration levels will be characterized using five different baffle plates. Although previous researchers have explored orifice plates, the vibration levels caused by systematically designed baffle plates has not previously been characterized.

A single pipe material (PVC) and fluid (water) was utilized in the experiments and consequently the dependence of pipe material and fluid density on the vibration levels is not possible. However, the amount of new data represents a significant contribution to the body of knowledge for turbulent flow through pipes with and without baffle plates. The results have applicability to both non-intrusive flow sensing and to design of pipe systems to withstand the fatigue loading they will encounter.

# 3 Experimental Facility

This chapter describes the hardware and data acquisition processes that were used to complete the experimental investigation. Sections 3.1 and 3.2 describe the components of the flow loop and test sections respectively. Sections 3.3 to 3.5 detail the instrumentation, measurement error analysis, and data acquisition hardware. Lastly, section 3.6 details how the experiments were conducted.

## 3.1 Water Flow Loop

Experiments were conducted in a water flow loop constructed for that purpose and is shown schematically in Fig. 3-1. Figures 3-2 to 3-6 are images of various portions of the facility and are described further in the following text. Water was circulated through the loop via a Bell and Gossett centrifugal pump with a maximum speed of 1800 RPM, driven by a 75 hp Marathon Electric 365T motor. The pump was placed on a concrete pad to help isolate its vibrations from the rest of the room. The pump speed was controlled by a Hitachi L300P 55kW, 75 hp variable frequency drive. The loop was filled by two open vertical vent columns shown in Figs. 3-2 and 3-3. These columns extend above the level of the flow loop to keep the system pressurized to approximately 3 kPa at no flow and prevent air from leaking into the system. These columns also served to vent entrained air bubbles resulting from the filling process and to prevent cavitation by maintaining nearly atmospheric pressure at the pump inlet and near bends where low pressure regions tend to develop.

The pump inlet is fed by 20.32 cm diameter schedule 80 PVC pipe (see Fig. 3-1 and Fig. 3-3). The pump outlets to 10.16 cm diameter schedule 80 pipe, which divides into a bypass branch and a main branch. Each branch is controlled by hand-actuated gate valves. The bypass line is a common fixture throughout the literature, providing a way to control flow rate without changing pump speed, but was not used for this research.

After the bypass branch junction, the main line then expands to 20.32 cm schedule 80 PVC to accommodate a flow conditioner (shown in Fig. 3-3) which minimizes swirl and breaks up pump-induced turbulence. The flow conditioner consists of a 7.62 cm thick piece of aluminum honeycomb caged between two cruciform aluminum rings; between the honeycomb and the downstream cruciform ring is a layer of PVC coated fiberglass mesh. Downstream of the second cruciform ring is another layer of fiberglass mesh and two more aluminum rings each with a layer of fiberglass mesh between them which provides for two more layers of fiberglass mesh. The rings and mesh are bolted together as a single unit. This robust design prevents the aluminum honeycomb from collapsing and being pushed through the flow loop when the flow rate is high.

After the flow conditioner, the pipe contracts to 10.16 cm schedule 80 pipe. After the contraction the pipe is connected to a flexible rubber coupler, Proco series 310 expansion joint. The coupler reduces structural vibrations transmitted to the test section from the pump and pipe components and is connected to the building by two wall mounts (one up-stream and one down-stream) to absorb low frequency pipe swaying. This arrangement is shown in Fig. 3-4.

The flow then either enters a 10.16 cm diameter, 6.096 m long developing region with a length to inner pipe diameter (*L/D* ~ 62) or is further reduced down to 5.08 cm diameter schedule 80 and passes into another rubber coupler and then into a 3.35 m long developing region of 5.08 cm schedule 80 pipe (*L/D* ~ 68). The developing regions allow the flow to become fully developed before entering the test section. Figures 3-2 to 3-6 show the 5.08 cm diameter configuration of the flow loop. A typical correlation for the development length for turbulent pipe flow is: [21]

$$\frac{L_e}{D} = 4.4Re^{\frac{1}{6}} \tag{3-1}$$

where $L_e/D$ is the ratio of entrance (developing) length to pipe diameter, and *Re* is the Reynold's number defined by:

$$Re = \frac{\rho V_f D}{\mu} \tag{3-2}$$

where $\rho$ is the fluid density, *D* is the inner pipe diameter, and $\mu$ is the dynamic fluid viscosity. According to Eq. 3-1, and for the largest *Re* explored in this study ($Re \sim 10^6$), Eq. 3-1 yields $L_e/D \sim 44$ indicating that the developing regions are more than sufficiently long enough to allow the flow to become fully developed.

After the developing region, the flow then passes into a test section, shown in Fig. 3-5, which is described in further detail in section 3.2. After the 5.08 cm test sections, the flow passes through a 1.22 m long segment of 5.08 cm schedule 80 pipe and another 5.08

cm diameter rubber coupler before re-expanding to 10.16 cm schedule 80 pipe. The 1.22 m long section provides for an *L/D* of 24 before the re-expansion to prevent disturbances induced by the re-expansion from propagating back up-stream (see Fig. 3-6). Data were taken using the 5.08 cm test sections with both the 10.16 cm developing region and the 5.08 cm developing region; the results will be discussed and compared in Chapter 4. After the test section, the flow then passes into 10.16 cm schedule 80 pipe and returns to the pump. On the return portion of the flow loop, a clear section of schedule 40 PVC is mounted in line to allow visual inspection of the flow and to ensure that air entrainment is not occurring.

## 3.2 Test Sections

The test sections consist of long interchangeable sections of 5.08 cm, 7.62 cm, and 10.16 cm diameter schedule 40 and 80 PVC pipe (see Fig. 3-5). For the 10.16 cm and 7.62 cm diameter test sections, the developing region diameter was 10.16 cm. For the 5.08 cm diameter test section, both the 10.16 cm and 5.08 cm diameter developing regions were used because there was concern that reducing from the 10.16 cm diameter developing region to the 5.08 cm diameter test section would cause pipe vibrations unrelated to this study. It was found that there was little difference between developing regions and this result is discussed further in Chapter 4. The actual pipe internal diameters, *D*, and wall thicknesses, *t*, of each test section are shown in Table 3-1. The test sections are hung supported from ceiling mounts using flexible cables that are free to swing. Along the wall adjacent to the test section are supports that can anchor each test section to the wall, allowing the investigation of how pipe vibration varies with clamping length.

A 0.159 cm hole was drilled into each test section at various axial locations along the test section length. PVC ports with a 0.635 cm tapped through hole were then glued onto the outside of the pipe at these locations to provide material to mount the pressure transducers (discussed in section 3.3). These ports can be seen as the dark rectangles in the photograph of the 10.16 cm schedule 40 test section (Fig. 3-5). Similar ports are employed on all of the other test sections. For the test sections associated with the 10.16 cm diameter developing region, the ports were located at 0.305 m, 0.610 m, 0.914 m, 1.524 m, 2.134 m. 3.048 m, and 5.791 m from the flange at the entrance of the test section. Accelerometers were also mounted at these same locations. The ports in the test sections associated with the 5.08 cm test section were located 0.305 m, 0.610 m, 1.219 m, 1.829 m, 2.743 m, and 5.486 m from the flange at the entrance of the test section.

**Table 3-1: Internal pipe diameters and wall thicknesses for experiments with PVC pipes.**

| **Pipe Schedule** | ***D* (m)** | ***t* (m)** | ***D/t*** |
|---|---|---|---|
| 5.08 cm Sch 80 | 0.0493 | 0.00554 | 8.899 |
| 7.62 cm Sch 80 | 0.0737 | 0.00762 | 9.672 |
| 10.16 cm Sch 80 | 0.0972 | 0.00856 | 11.355 |
| 5.08 cm Sch 40 | 0.0525 | 0.00391 | 13.427 |
| 7.62 cm Sch 40 | 0.0779 | 0.00548 | 14.215 |
| 10.16 cm Sch 40 | 0.102 | 0.00602 | 16.944 |

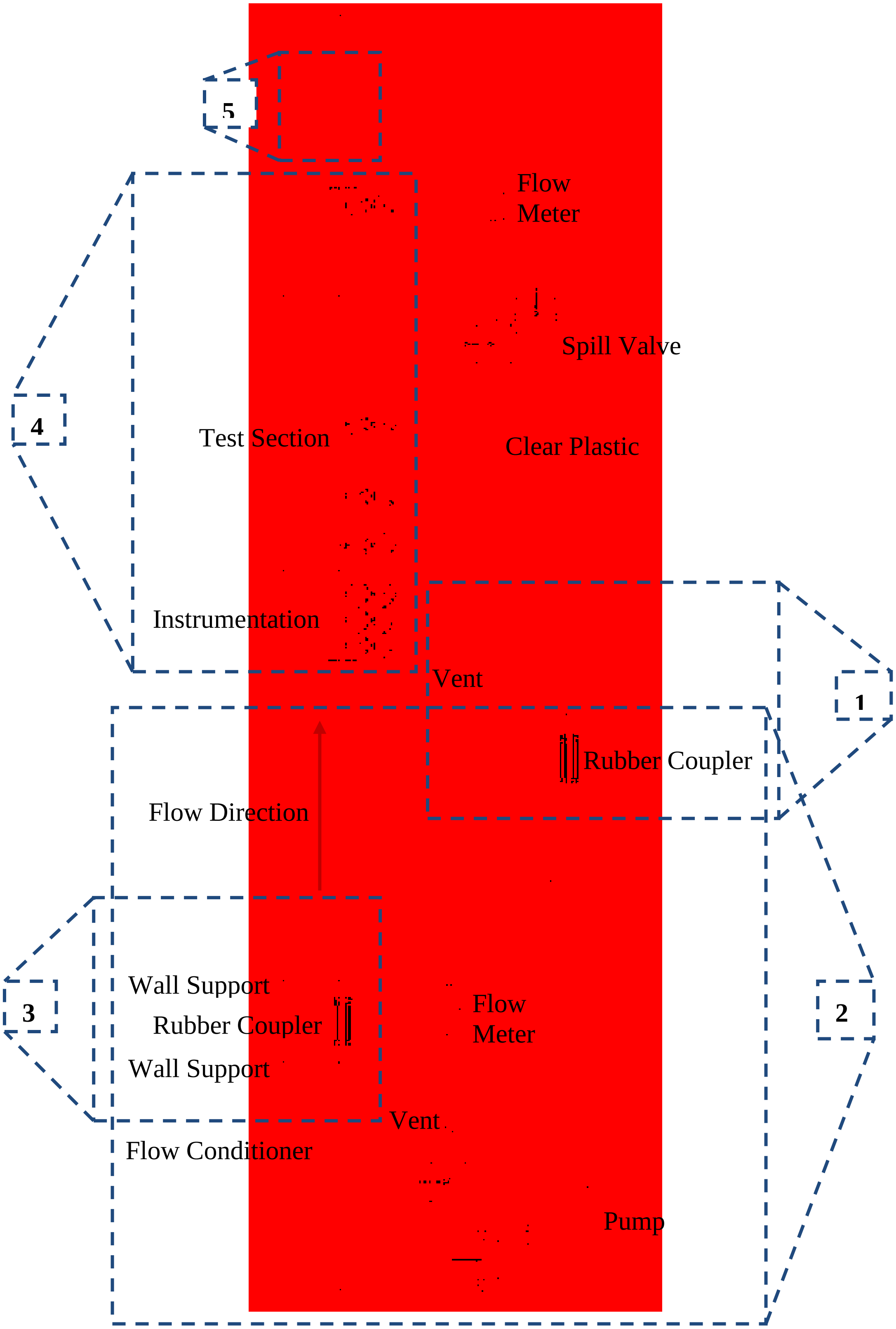

**Figure 3-1: Schematic diagram of flow loop with callouts corresponding to photographs below.**

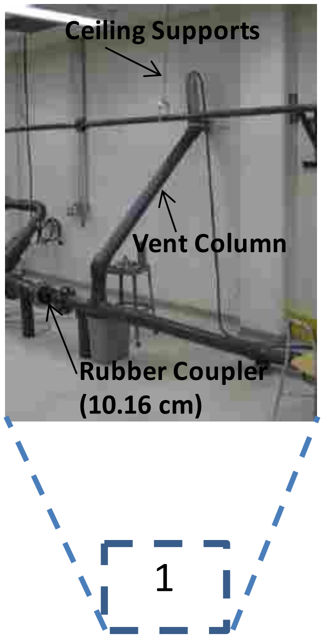

**Figure 3-2: Photograph of a vent column.**

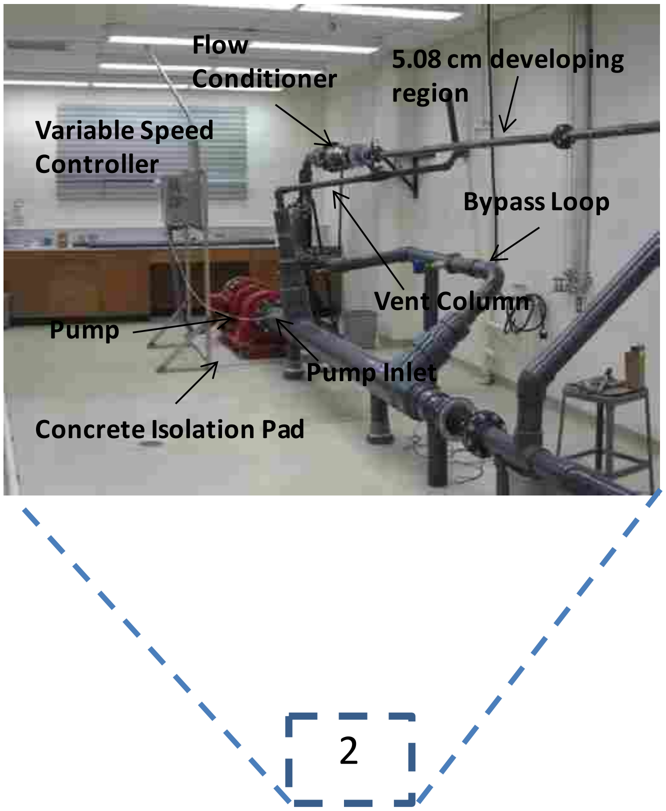

**Figure 3-3: Photographs of pump, bypass line, flow conditioner, 5.08 cm developing region and vent column.**

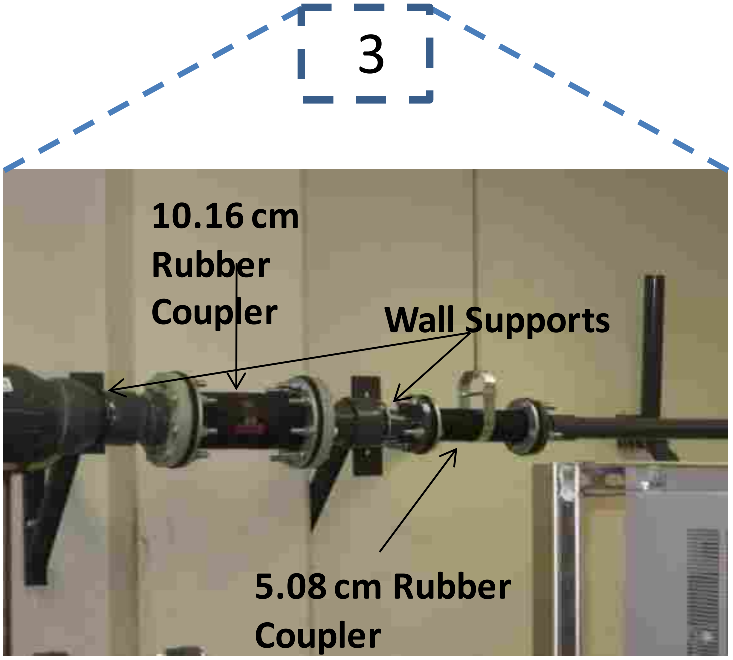

**Figure 3-4: Photograph of rubber couplers leading into the 5.08 cm diameter developing region.**

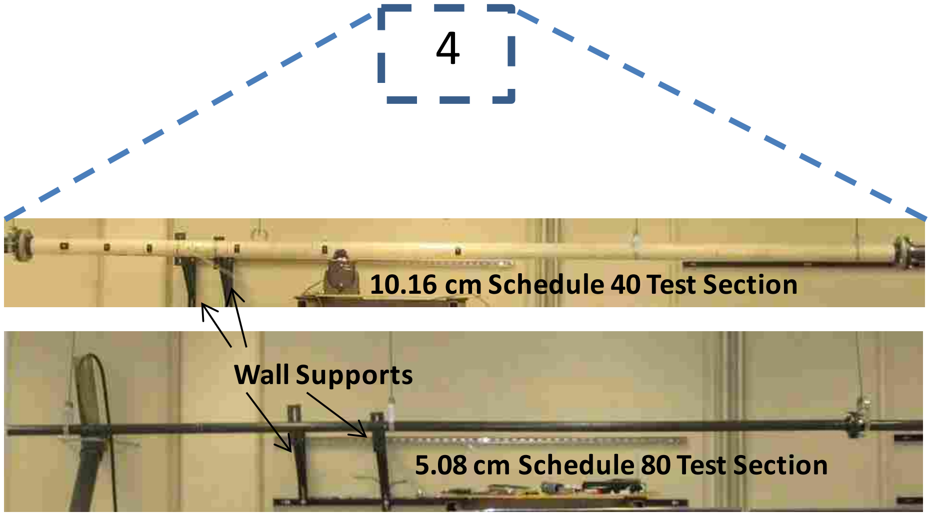

**Figure 3-5: Photograph of 10.16 cm and 5.08 cm test sections. Wall supports are shown in the background.**

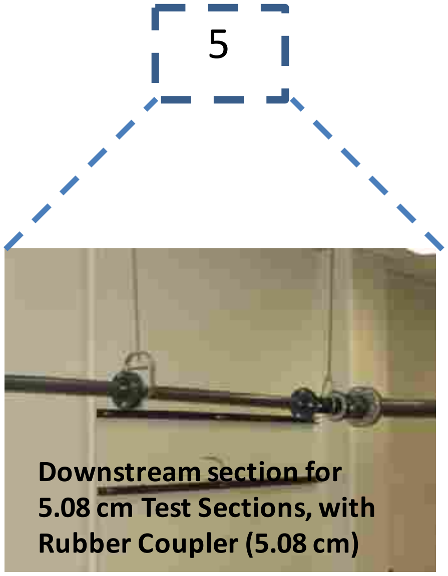

**Figure 3-6: Photograph of vibration isolation downstream of the 5.08 cm test section before re-expansion to 10.16 cm pipe.**

In order to produce various levels of turbulence in the test sections, baffle plates were inserted between the flanges that connected the end of 10.16 cm developing region and the test sections. The baffle plates are shown in Fig. 3-7. Five baffle plates were machined from 0.635 cm thick aluminum plate with 2.54 cm, 1.27 cm, 0.635 cm, 0.318 cm, and 0.159 cm holes drilled into them. The center pitch of the holes (distance between the center of one hole and the center of the next hole) was 3.2 cm, 1.6 cm, 0.8 cm, 0.4 cm, and 0.2 cm respectively. The through area of the holes in each baffle plate was constant and equal to 35.48 cm$^2$. This results in seven holes for the 2.54 cm baffle plate and 1793 holes for the 0.159 cm baffle plate. The ratio of the through area of the holes to pipe area, $A_h/A_p$, for the 10.16 cm diameter schedule 40 and 80 test sections is 0.434 and 0.478 respectively.

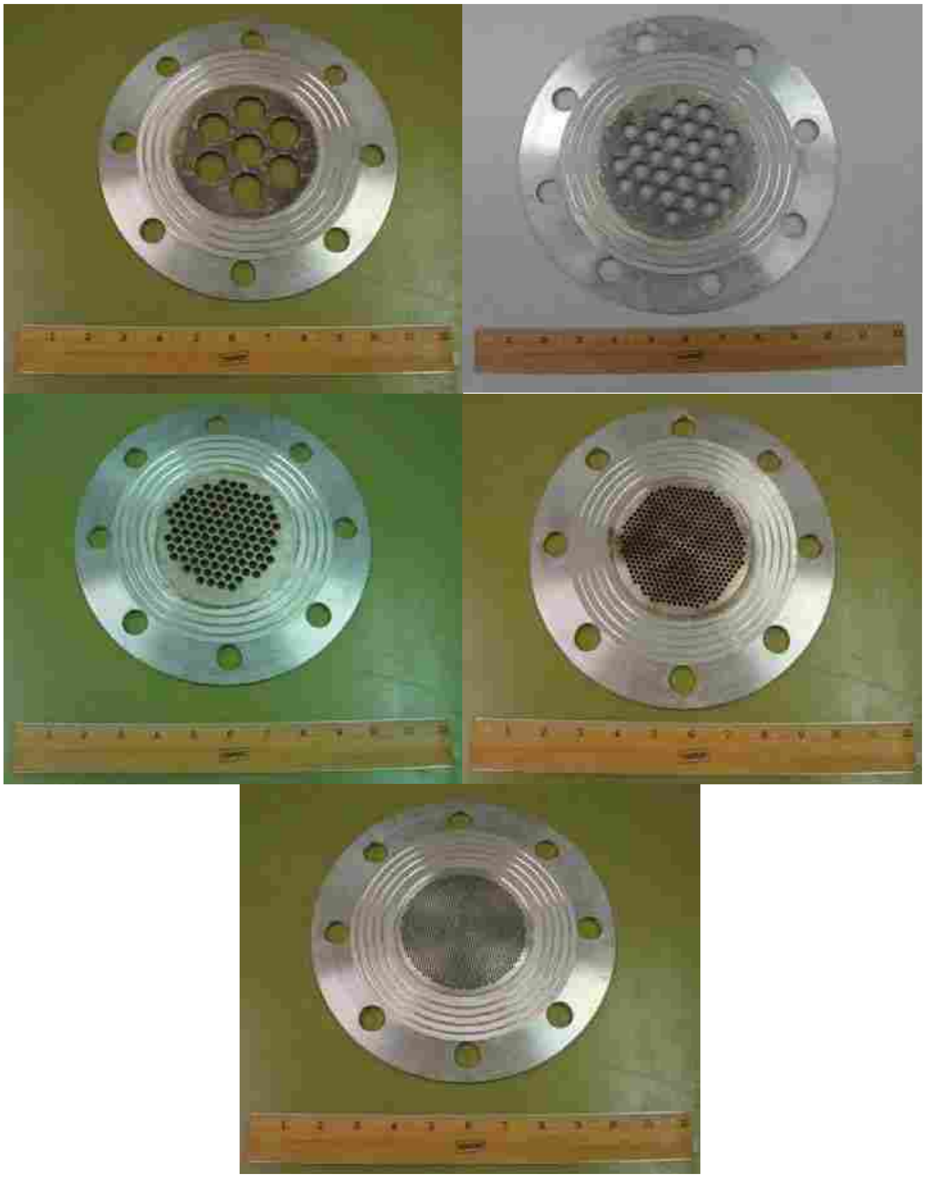

**Figure 3-7: Baffle plates used for experiments with 2.54 cm (top left), 1.27 cm (top right), 0.635 cm (middle left), 0.318 cm (middle right) and 0.159 cm (bottom) holes.**

## 3.3 Instrumentation

Two PCB 352B68 accelerometers with a measurement range of ± 491 m/s$^2$, a resolution of 1.5x10$^{-3}$ m/s$^2$, and sensitivity of 10.2 mV/(m/s$^2$) were used to measure pipe wall acceleration. Accelerometers were placed on opposite sides of the test section (forward and back) at the seven or five axial locations along the length of the test section described in section 3.2. A pressure transducer that measures fluctuations in the pressure field (PCB S102A02) with a measurement range of 690 kPa, a resolution of 14 Pa, and a sensitivity of 7.3 mV/kPa was mounted on the test section through the pressure ports described in section 3.2. This particular pressure transducer has a stainless steel diaphragm that resists corrosion that can result from being immersed in water and lead to the failure of the sensor.

On the return leg of the flow loop, and on the bypass line, an Omega FP6500 paddle wheel flow meter with a range of 0.1-12 m/s and an accuracy of ± 1.5% was used to measure the average velocity of the water through the pipe. Use of the continuity equation made it possible to measure the average fluid velocity through each test section. This is based only on the square of the ratio of the return leg diameter to test section diameter and a measure of the average velocity through the return leg of the flow loop. Total pressure drop across the length of the test section is also measured with two pressure gages; one placed just up-stream of the test section and the other just down-stream.

A PCB 086B01 impact hammer with a nylon tip was used to measure the frequency response of the test sections under varying support conditions.

## 3.4 Measurement Error Analysis

### 3.4.1 Pressure Fluctuation Uncertainty Analysis

It is known that several factors can introduce error into wall pressure measurements. These factors include the effects of hole-size, tapping depth, and the conditions at the edge of the tapped orifice due to burrs. Pressure measurements at the wall are given by [22]:

$$p_w = p_{mw} - \Pi \tau_w \tag{3-3}$$

Where $p_w$ is the true pressure at the wall, $p_{mw}$ is the pressure measured at the wall, $\Pi$ is the pressure error discussed below, and $\tau_w$ is the wall shear stress defined as:

$$\tau_w = \frac{\rho V_f^2 f}{8} \tag{3-4}$$

Where $f$ is the Darcy friction factor. The literature provides correlations of experimental pressure error data due to hole-size, tapping depth, and orifice edge effects. These are presented as a function of the tapping diameter in wall units, $d_s{}^+$, which is defined as:

$$d_s^+ = \frac{u_\tau d_s}{\nu} \tag{3-5}$$

where $u_\tau$ is the friction velocity based on the wall shear stress:

$$u_\tau = \sqrt{\frac{\tau_w}{\rho}} \tag{3-6}$$

$d_s$ is the tapping diameter and $v$ is the kinematic viscosity of the fluid.

Using information in [21] the parameter $\Pi$ was estimated at a low and high velocity for each test section where $\Pi$ factors for the three contributing uncertainty influences (tap diameter, tap depth, and edge effects) are shown. These values are included in Table 3-2.

For all ports the tap diameter is 0.159 cm for a $d_s$ to $D$ ratio ranging from 0.016 to 0.031, with the larger value just outside the regime that the $\Pi_{\text{tap}}$ correlation is valid for. The tap depth is the thickness of each test section and is assumed to be a narrow tapping for the $\Pi_{\text{depth}}$ correlation. Finally, the burr height aspect ratio ($\varepsilon/d_s$) is assumed to be 0.032, the largest $\Pi_{\text{edge}}$ correlation given, because some of the pressure ports had some large burrs. It can be seen that the estimated pressure error at the high velocity values is very large, reaching about 4.5 kPa in the 7.62 cm diameter schedule 80 test section. The largest contributing factor is caused by edge effects; contributing on average 72.44% of the total pressure error, $\Pi_{\text{tot}}$.

It will be shown later that the values of $\Pi_{\text{tot}}\tau_w$ are on the same order of magnitude as the measured pressure fluctuations, indicating that pressure fluctuation comparisons between test sections, or even at different tap locations in the same test section, may not yield comparable information. The pressure measurements can however show how the measured pressure fluctuations vary with changes in fluid velocity at a fixed location and will be discussed further in Chapter 4.

The measurement uncertainty of the pressure transducer as stated by the manufacturer is ±7 Pa.

**Table 3-2: Pressure error estimates based on tap hole size, tapping depth, and orifice edge.**

| **Test Section** | $V_f$ **(m/s)** | $\tau_w$ **(Pa)** | $d_s^+$ | $\Pi_{tap}$ | $\Pi_{depth}$ | $\Pi_{edge}$ | $\Pi_{tot}$ | $\Pi_{tot}\tau_w$ **(Pa)** | $\Pi_{edge}/\Pi_{tot}$ **(%)** |
|---|---|---|---|---|---|---|---|---|---|
| **10.16 cm Sch 40** | 3.4 | 20.66 | 204.07 | 0.90 | 0.89 | 5.31 | 7.01 | 146.69 | 75.75 |
| | 6.7 | 70.70 | 377.48 | 1.79 | 2.04 | 9.65 | 13.48 | 952.80 | 71.59 |
| **10.16 cm Sch 80** | 4 | 27.96 | 237.38 | 1.06 | 1.12 | 6.15 | 8.32 | 232.74 | 73.92 |
| | 7.7 | 92.12 | 430.88 | 2.09 | 2.31 | 10.98 | 15.39 | 1417.75 | 71.35 |
| **7.62 cm Sch 40** | 5.7 | 55.44 | 334.25 | 1.56 | 1.77 | 8.57 | 11.90 | 659.68 | 72.02 |
| | 10.8 | 177.58 | 598.25 | 3.11 | 2.80 | 15.17 | 21.08 | 3743.00 | 71.96 |
| **7.62 cm Sch 80** | 6 | 61.47 | 351.97 | 1.65 | 1.88 | 9.01 | 12.55 | 771.37 | 71.79 |
| | 11.5 | 201.19 | 636.76 | 3.36 | 2.84 | 16.13 | 22.32 | 4491.26 | 72.27 |
| **5.08 cm Sch 40** | 4.5 | 38.91 | 280.02 | 1.28 | 1.41 | 7.21 | 9.90 | 385.17 | 72.83 |
| | 9 | 136.59 | 524.67 | 2.65 | 2.66 | 13.33 | 18.64 | 2545.41 | 71.51 |
| **5.08 cm Sch 80** | 4.8 | 44.24 | 298.59 | 1.37 | 1.54 | 7.68 | 10.59 | 468.32 | 72.52 |
| | 9.7 | 158.42 | 565.05 | 2.90 | 2.75 | 14.34 | 19.99 | 3166.36 | 71.74 |

### 3.4.2 Accelerometer Uncertainty Analysis

The instrument accuracy of the accelerometers is $\pm 7.8\text{x}10^{-4}$ m/s$^2$ as stated by the manufacturer.

## 3.5 Data Acquisition

A PC-based data acquisition system consisting of a multi-channel National Instruments data acquisition module was used to collect acceleration, flow rate, and fluctuating pressure time series data. For the accelerometer and pressure fluctuation time series data, the rms values of the time series were computed. These values are referred to here as *A'* and *P'* respectively and represent typical magnitudes in the pipe wall acceleration and internal surface pressure fluctuations. The accelerometer data were also integrated to yield pipe velocity (integrated once). Subsequently the rms values of the pipe velocity, *V'* was also computed. All of the sensors were sampled for 10 second intervals at a sample rate of 5000 Hz. To prevent low frequency drift in the accelerometers and pressure transducer, 2 Hz and 20 Hz high pass filters were applied respectively.

## 3.6 Experimental Process

Experiments were conducted in the following manner. For each unsupported test section, the pump was powered to a speed that was nominally 70% of the pump maximum flow rate. At this pump speed, the flow was allowed to become steady, and then 10 seconds of time series data were acquired. The pump speed was then decreased slightly and for each scenario considered this was repeated at 24-29 discrete flow rates.

For each test section, the accelerometer and pressure transducer were placed at the first pressure port location where *A'* and *P'* data were collected as stated above. The sensors were then moved to the next pressure port location and the process was repeated until data were collected along the entire test section length.

Experiments were then performed using the wall mounted pipe clamp supports. The first pipe clamp was placed 1.07 m from the flange connecting the developing region to the test section. The second support was placed 3.69 m away from the first.

This was considered a full support separation. The accelerometers were then placed at one half and one quarter of this resulting support separation (having the accelerometers in the same location, but without the wall supports was considered having no support). Again, the process of data collection was repeated for this configuration. Without moving the first support, the downstream support would then be moved to half of the full separation case. The distance between the wall supports was designated as a fraction of the full support case (full support, half support, quarter support, eighth support, and sixteenth support), with one accelerometer at one half of the support separation and the other at one quarter of the support separation. Experiments were then conducted in the same manner described above. Subsequently, the baffle plates were inserted and experiments were repeated in the manner described above. Table 3-3 illustrates the experiments that were conducted for each test section.

**Table 3-3: List of experiments conducted. Where X's signify that an experiment was conducted at the listed conditions and O's indicate no experiment.**

| **Experiment** | **5.08 cm Sch 40** | **5.08 cm Sch 80** | **7.62 cm Sch 40** | **7.62 cm Sch 80** | **10.16 cm Sch 40** | **10.16 cm Sch 80** |
|---|---|---|---|---|---|---|
| **Unsupported** | **X** | **X** | **X** | **X** | **X** | **X** |
| **Full Support** | **X** | **X** | **X** | **X** | **X** | **X** |
| **1/2 Support** | 0 | 0 | 0 | 0 | **X** | 0 |
| **1/4 Support** | **X** | **X** | **X** | **X** | **X** | **X** |
| **1/8 Support** | 0 | 0 | 0 | 0 | **X** | 0 |
| **1/16 Support** | 0 | 0 | 0 | 0 | **X** | 0 |
| **2.54 cm Baffle Plate** | 0 | 0 | 0 | 0 | **X** | **X** |
| **1.27 cm Baffle Plate** | 0 | **X** | 0 | **X** | **X** | **X** |
| **0.635 cm Baffle Plate** | **X** | 0 | **X** | 0 | **X** | 0 |
| **0.318 cm Baffle Plate** | 0 | **X** | 0 | **X** | **X** | 0 |
| **0.159 cm Baffle Plate** | 0 | 0 | 0 | 0 | **X** | 0 |

# 4 Results

This chapter presents and discusses the experimental results obtained using the water flow loop described in Chapter 3. These results will also be compared to the conclusions drawn by other researchers detailed in Chapter 2. Section 4.1 presents the results obtained from pipe test sections unclamped by the wall supports (no support). The behavior of the wall pressure and accelerometer fluctuations is described. This is done by analyzing the rms values of the fluctuating pressure and acceleration time series signals (*P'* and *A'*) and the Power Spectral Density (PSD) of the acceleration signal. Section 4.2 then presents a similar analysis of acceleration measurements with various pipe clamping distances. Section 4.3 compares the effects of various non-dimensional parameters on *A'*. Section 4.4 then presents the effects on pipe vibration of placing baffle plates with various hole sizes into the flow.

## 4.1 Unsupported Pipe

Experiments described in this section were conducted on an unsupported pipe (*i.e.* without using pipe clamping). The accelerometers and pressure transducer were placed at the positions described in section 3.2. Data were acquired as described in section 3.5.

### 4.1.1 Wall Pressure Fluctuations

The total pressure drop, $\Delta P$, was measured in the 7.62 cm and 10.16 cm diameter schedule 80 test sections by taking the difference of static pressure measurements made with bourdon tube style pressure gages placed near the test section entrance and exit. Figure 4-1 shows the average of $P'$ along the test section length as a function of $\Delta P$ for the 7.62 cm schedule 80 test section. The data exhibit a nearly linear relationship, with the magnitude of the pressure fluctuations on the order of 2% of the total pressure drop over the length of the test section. A least squares power law fit of the data over the range $\Delta P > 20$ kPa yields $P' \sim \Delta P^m$ where $m \sim 1.1$. Although not shown, the $P'$ vs. $\Delta P$ behavior for the 10.16 cm schedule 80 pipe is similar, where $m \sim 1.1$. It is expected that this behavior would be the same for the other test sections. The implication here is that the average wall pressure fluctuations along the test section length scales nearly linearly with the total average pressure drop.

For fully-developed turbulent pipe flow, the total pressure drop may be expressed as [23]

$$\Delta P = \frac{f L \rho V_f^2}{2D} \tag{4-1}$$

The Reynold's number range of the data of Fig. 4-2 ($V_f > 2.2$ m/s) is roughly $2.01 \times 10^5 \leq Re \leq 7.58 \times 10^5$. Over this range of $Re$ the friction factor for a hydraulically smooth pipe is very nearly approximated by the expression, [21] $f \approx 0.316/Re^{0.25}$ . Substituting this relation for the friction factor into equation 4-1 yields

$$\Delta P \approx \frac{0.158 L \rho^{0.75} V_f^{1.75} \mu^{0.25}}{D^{1.25}} \tag{4-2}$$

where $\mu$ is the absolute fluid viscosity. Based on the data shown in Fig. 4-1 and the relationship shown in equation 4-2, it can be shown that $P' \sim \Delta P \sim V_f^2$. This is what was implied in section 2.3.

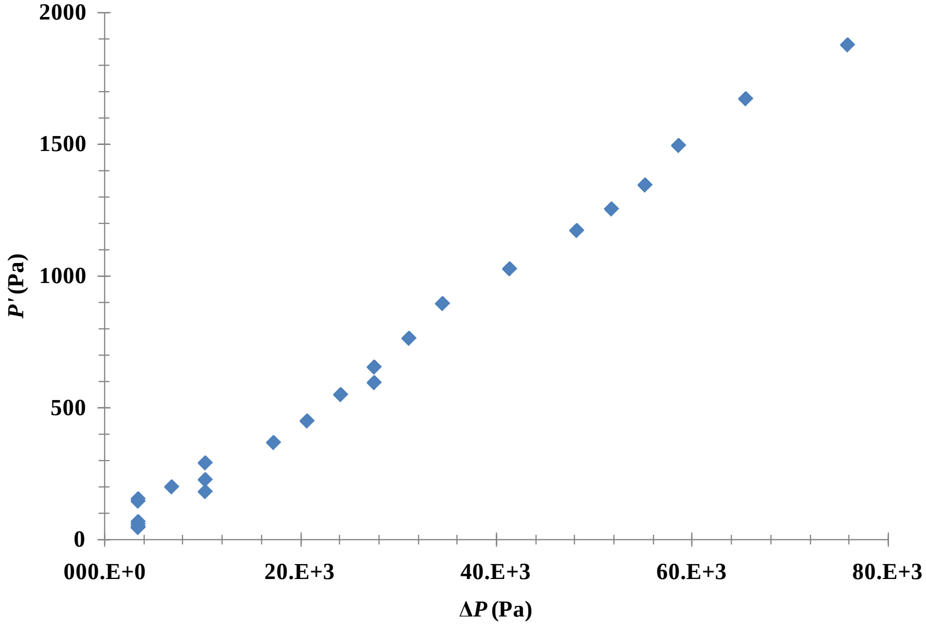

**Figure 4-1: *P′* as a function of the total pressure drop, Δ*P*, across the test section for the Schedule 80 7.62 cm test section.**

Shown in Fig. 4-2 is $P'$ as a functions of the average fluid speed (top panel) and the average flow rate (bottom panel) in the pipes. Results are shown for all six test sections listed in Table 3-1. The plots represent an average of the $P'$ measurements over the six discrete axial locations along the pipe where pressure data were acquired. At low speeds some scatter exists in the data due to resolution limits of the sensors. At higher speeds however, ($V_f > 2$ m/s) the trend in the data is similar for all test sections. Namely, the $P'$ vs. $V_f$ trend exhibits a power law relation, $P' \sim V_f^m$. A least squares fit to each data set shown in Fig. 4-2 over the range $V_f > 2.5$ m/s reveals that $m$ varies from 1.91 to 2.07 with an average value of 2.02. There appears to be no systematic variation in $m$, and the difference between $m$ and the expected value of 2.0 is less than 5%. Performing an analysis of variance between the determined values of $m$ and the expected value of 2.0 provides sufficient evidence to conclude that the variation in $m$ is insignificant. This result is in excellent agreement with the analysis of the $P'$ vs. $\Delta P$ data shown in Fig. 4-1 and Eqs. 4-1 and 4-2 and provides two independent measures showing that $P'$ scales directly with the average fluid dynamic pressure ($\rho V_f^2$).

When plotted as a function of $V_f$, the $P'$ data for the 10.16 cm diameter schedule 40 test section shows the largest magnitude at a given $V_f$. The magnitude of the $P'$ data 10.16 cm test sections appears to be larger than the data for the 7.62 cm test sections, which are larger than the data for the 5.08 cm test sections. As expected, however, there seems to be no systematic variation in $P'$ with diameter to thickness ratio ($D/t$). When plotted as a function of $Q$ (which is a function of $D$ and $V_f$), the behavior of the magnitude of $P'$ in the test sections appears to be reversed, with the data for the 5.08 cm schedule 80 test section showing the largest $P'$ magnitude at a given $V_f$. Due to the large uncertainty associated with the pressure measurements, comparison of the $P'$ magnitude between test sections is somewhat suspect.

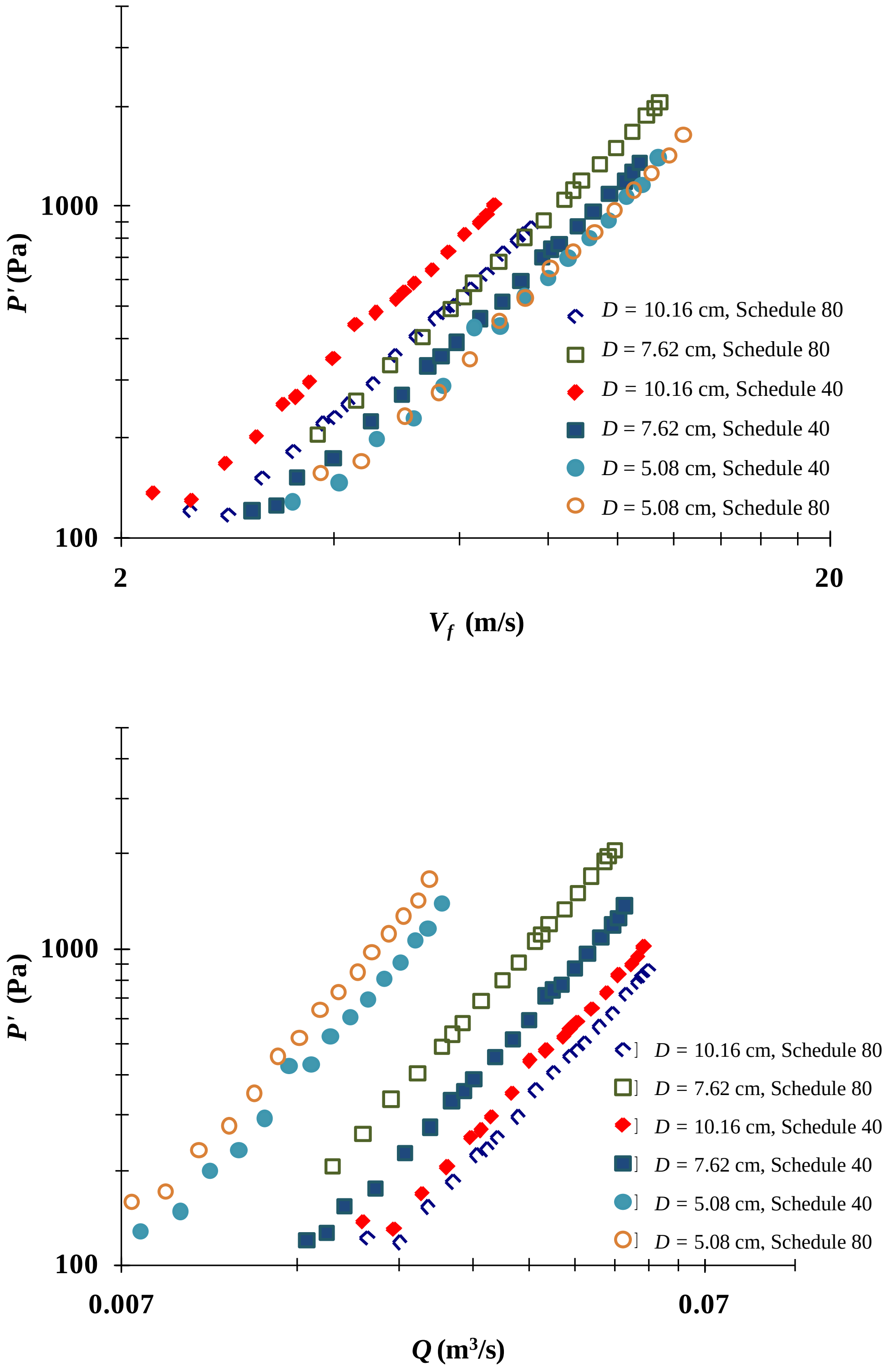

**Figure 4-2: *P′* as a function of the average fluid speed, $V_f$ (upper panel), and average flow rate, *Q* (lower panel), for flow through the six test sections.**

### 4.1.2 Accelerometer Measurements

#### 4.1.2.1 *A'* as a Function of *P'*

Figures 4-3 and 4-4 show *A'* and *V'* respectively as a function of *P'* for each of the six test sections. The trend in the data is similar to that shown in Fig. 4-2. For both *A'* and *V'* the data exhibit power law relations, $Z' \sim P'^m$, where *Z'* represents *A'* or *V'*. A least squares fit of the data in Fig. 4-3 shows that *m* varies from 0.95 to 1.04 with an average value of 1.01. The variation in *m* is again considered insignificant. This implies that *A'* scales as $V_f^2$ as suggested in section 2.3.

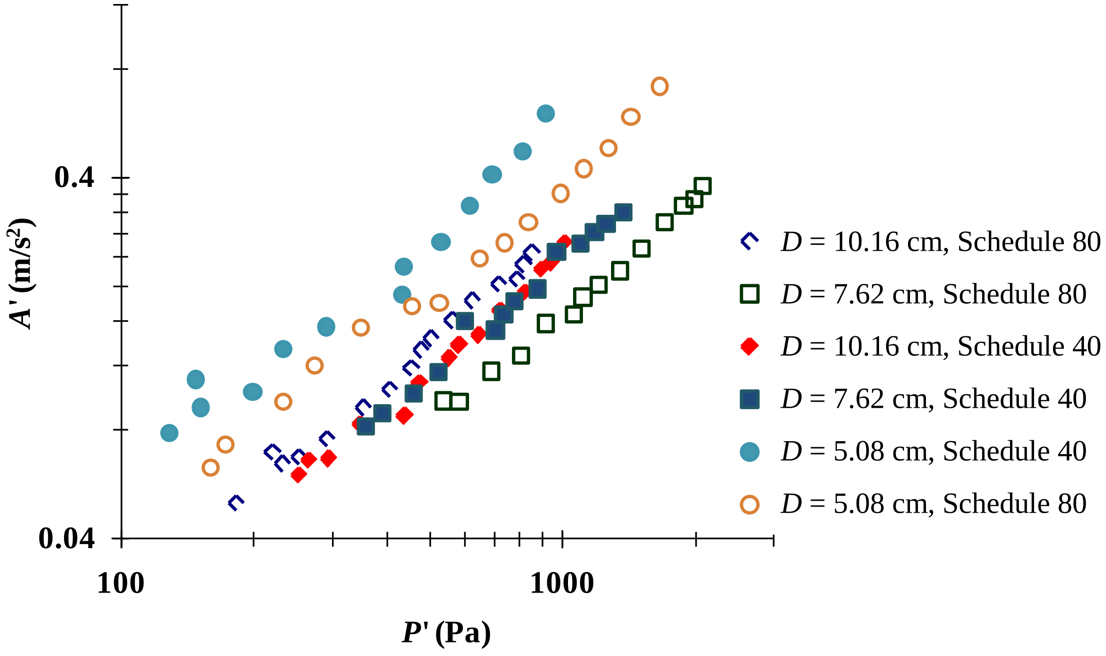

**Figure 4-3: *A'* as a function of *P'* for flow through the six test sections.**

Repeating a least squares fit for the data in Fig. 4-4 shows that *m* varies from 0.78 to 0.92 with an average value of 0.81. Raising *P'* (i.e. $V_f^2$) to this average power shows that *V'* scales nominally as $V_f^{1.62}$. According to the data presented by Pittard *et al.* presented in section 2.4, it was expected that *V'* should scale nominally as $V_f^{1.6}$, which is in excellent agreement with the result presented here.

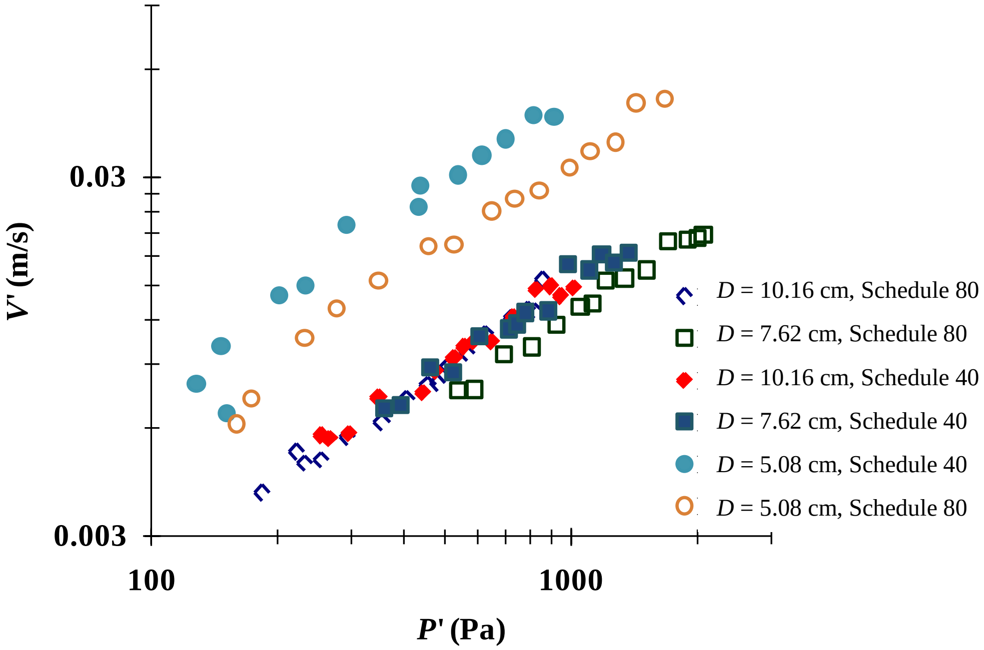

**Figure 4-4: *V'* as a function of *P'* for flow through the six test sections.**

#### 4.1.2.2 *A'* as a Function of $V_f$

Figure 4-5 shows *A'* as a function of $V_f$ along the length of the 10.16 cm schedule 40 test section, where *x/D* is the ratio of the distance from the test section entrance to inner pipe diameter. Data are shown at *x/D* = 3, 6, 9, 15, 21, 30, and 57. The data in this figure show a similar power law behavior as the *A'* vs. *P'* data of section 4.1.2, of the form $A' \sim V_f^m$. Above a speed of nominally 3.5 m/s where the level of pipe vibration is elevated above background levels, *m* varies in the range from 1.91 to 2.39 for the seven *x/D* locations, with an average value of 2.14. The data also exhibit little variation in *A'* with *x/D* position and no systematic pattern in the variation exists. Similar behavior is observed for the other test sections explored. Because of this, the *A'* and *V'* data for each test section (supported and unsupported) will be averaged over all *x/D* locations in subsequent figures.

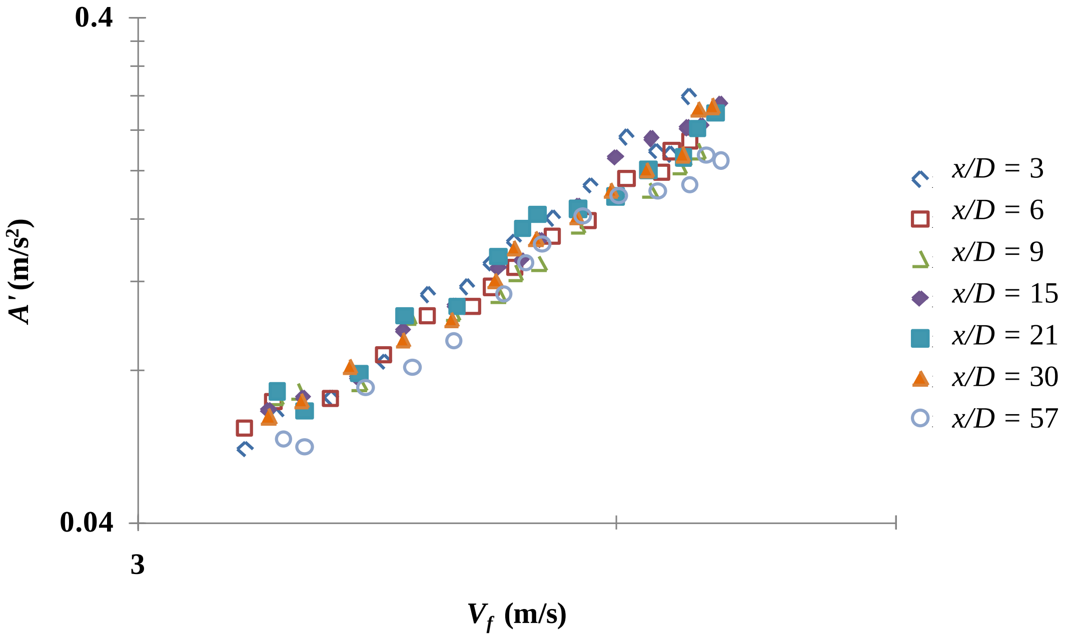

**Figure 4-5:** ***A'*** **as a function of** ***$V_f$*** **at seven** ***x/D*** **locations along the length of the 10.16 cm schedule 40 test section.**

Figure 4-6 shows *A'* averaged over all *x/D* measurement positions as a function of $V_f$ and *Q* for each test section considered. Similarly, Fig. 4-8 presents *V'* averaged over all *x/D* measurement positions as a function of $V_f$ and *Q* for each test section considered. The data in these figures show similar power law behavior as the *V'* vs. *P'* data of section 4.1.2.1. Above 3.5 m/s, *A'* and *V'* exhibit a power law dependencies of the form $Z' \sim V_f^m$. For *A'*, *m* varies from 1.94 to 2.19, with an average value of 2.06. Performing an analysis

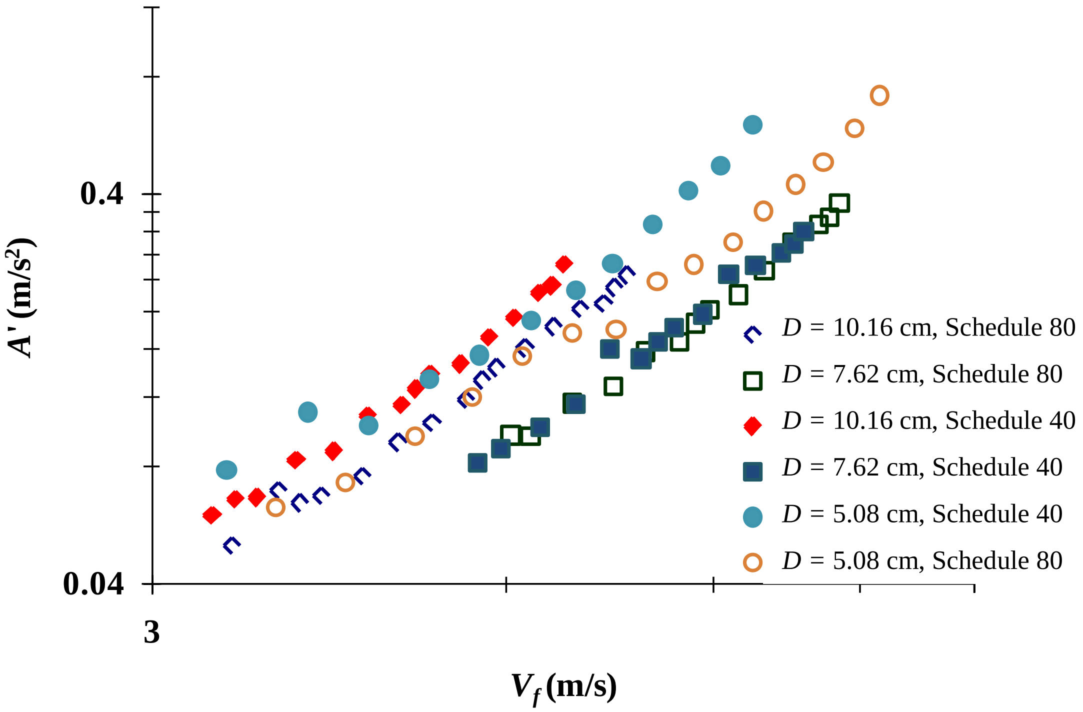

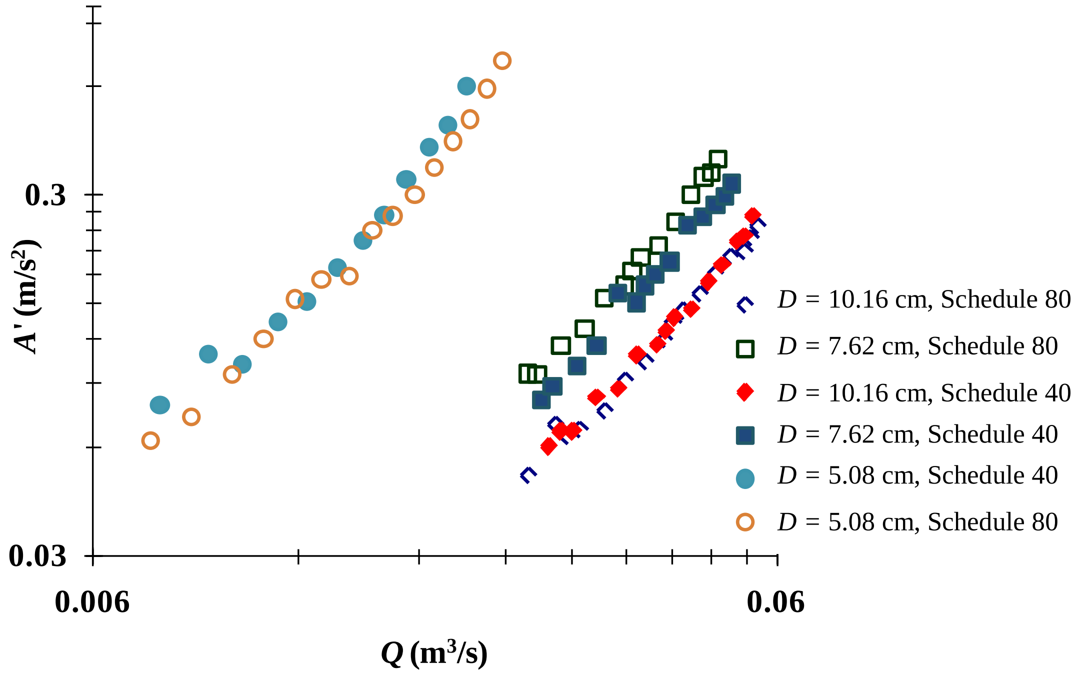

**Figure 4-6: *A'* as a function of $V_f$ (top panel) and *Q* (bottom panel) for flow through the six test sections considered.**

of variance on the values of *m* and the expected value of 2.0 indicates that the variation in *m* is insignificant. When plotted as a function of $V_f$, the magnitude of *A'* at a given $V_f$ is nominally 50% greater for the 10.16 cm and 5.08 cm test sections than for the 7.62 cm test sections. Recall from section 2.4 that Evans *et al.*, using a flow loop similar to the one described in Chapter 3, obtained average values of the power law exponent *m* for *A'* and *V'* of 2.16 and 1.68 respectively. These values are only marginally greater than the values of *m* for the current data, differing by about 8% and 5%, respectively.

Modest variation between schedule 40 and 80 data sets exist for each pipe diameter, with the general trend being an increase in *A'* with decreasing schedule size. The wall thickness for all of the schedule 80 test sections is in the range 39-42% greater than for the schedule 40 test sections, while the diameters differ in the range 3-6% respectively. Surprisingly, the *A'* vs. $V_f$ data of Fig. 4-6 does not exhibit a systematic variation with pipe diameter. The data for the intermediate diameter size (7.62 cm) lies lower than for the other two diameter sizes.

When *A'* is plotted as a function of *Q*, the behavior appears somewhat different, although the values of the power law exponent *m* ($A' \sim Q^m$) remain the same. Here the magnitude of *A'* is systematic with pipe diameter where the 10.16 cm test section data lies below the 7.62 cm test section which lies below the 5.08 cm test section data.

Figure 4-7 presents *A'* as a function of the pipe diameter to thickness ratio, *D/t*, for each test section and a constant fluid velocity of 6.7 m/s. Although there are only two points for each pipe diameter, the trend illustrates that *A'* increases with increasing *D/t* although the dependency is not the same for varying pipe diameter. Similar conclusions can be drawn from the data of Fig. 4-6 (top panel).

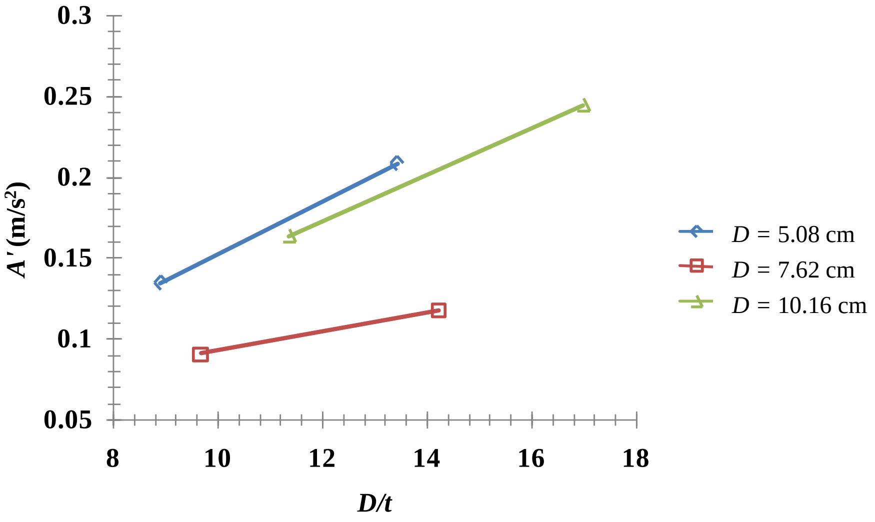

**Figure 4-7: *A'* as a function of *D/t* at $V_f \approx$ 6.7 m/s for each the three diameter pipes considered.**

Figure 4-8 shows *V'* as functions of $V_f$ (top panel) and *Q* (bottom panel) for each of the six test sections. The values of the power law exponent *m* ($V' \sim V_f^m$) range from 1.51 to 1.72, with an average value of 1.64. Again, the variation is deemed to be non-systematic. This is also in good agreement with the expected scaling of $V_f^{1.6}$, as stated in section 4.1.2.1, based on the *V'* vs. *P'* data. Further, this is in good agreement with the experimental results of Pittard *et al.*[2] presented in section 2.4. When plotted as functions of $V_f$ (top panel) and *Q* (bottom panel), *V'* behaves very similarly to the *A'* data. Specifically, the *V'* vs. $V_f$ data does not exhibit a systematic variation with pipe diameter. However, when *V'* is plotted as a function of *Q* the magnitude of *V'* is systematic with pipe diameter, where the 10.16 cm test section data lies below the 7.62 cm test section data which lies below the 5.08 cm test section data. A notable difference is that

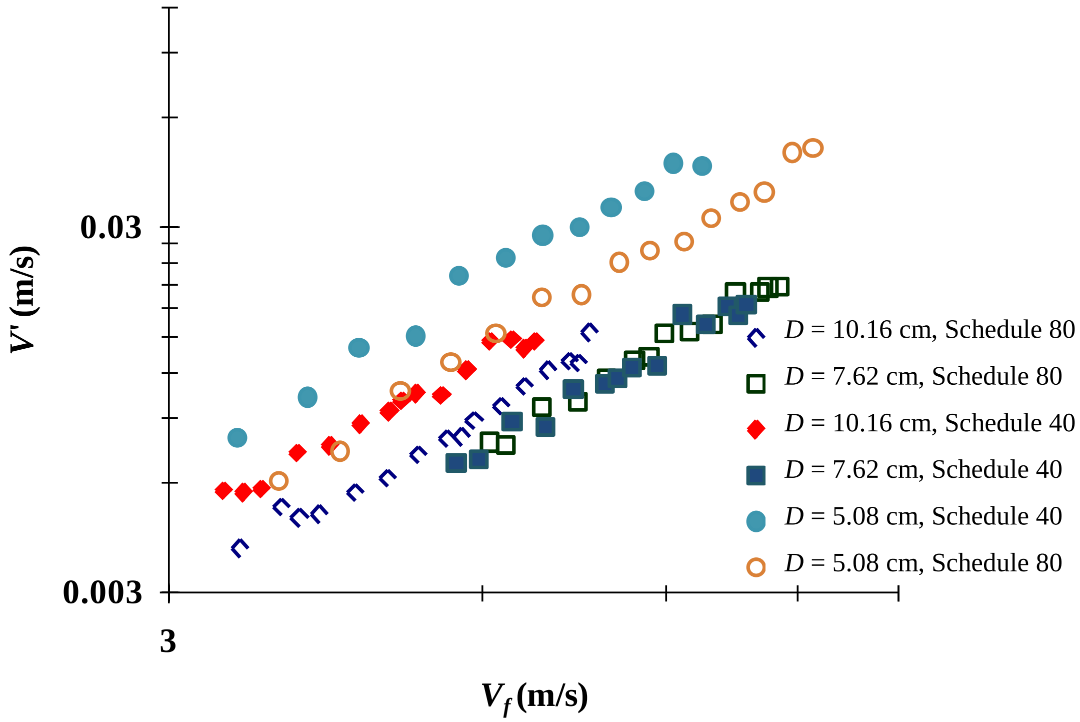

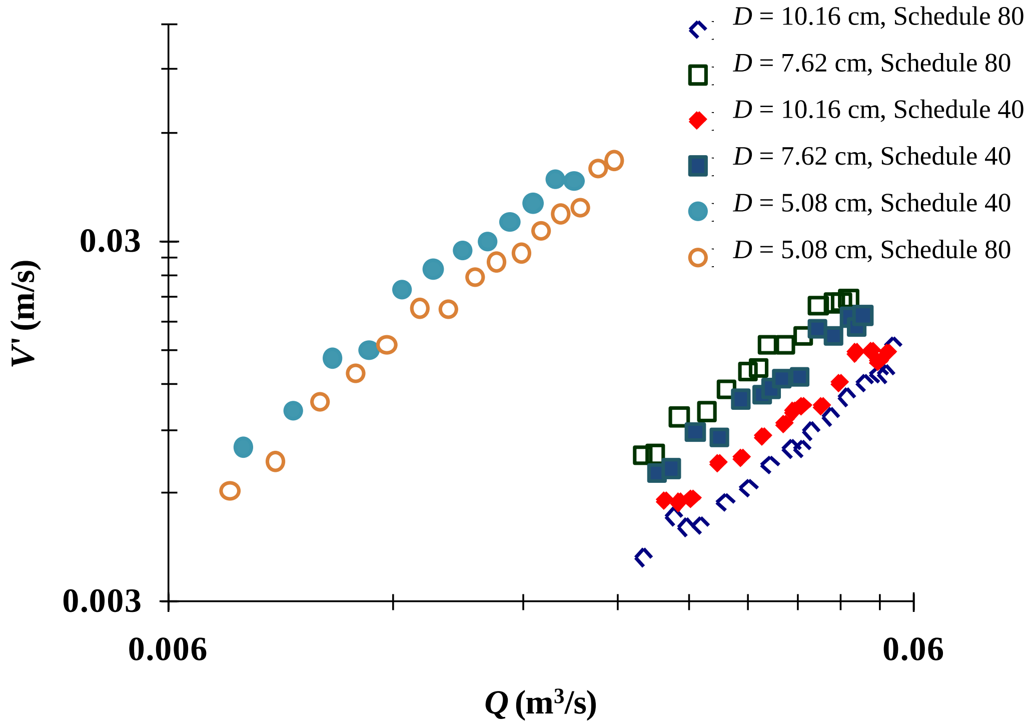

**Figure 4-8: $V'$ as a function of $V_f$ (top panel) and $Q$ (bottom panel) for flow through the six test sections considered.**

there is more separation in the relative magnitudes of $V'$ between the 5.08 cm and 10.16 cm data sets, with the relative magnitude of the 5.08 cm data being noticeably larger than the 10.16 cm data, when compared to $A'$ vs. $V_f$.

#### 4.1.2.3 Acceleration Spectra

Power spectral densities (PSDs) were computed from the acceleration time series data for each test section and at several velocities. Each PSD was then compared to the frequency response of the corresponding test section which was excited with the impact hammer described in section 3.3.

Frequency response data were collected by placing an accelerometer half way down the length of a stationary water filled test section and striking the pipe several times with the hammer adjacent to the accelerometer. Two seconds of data were collected per impact at a rate of 5000 Hz. The pipe was struck five times and the resulting spectra were averaged together. This average is referred to hereafter as the natural pipe response.

The PSDs were calculated for each data set by breaking the 10 seconds of acceleration data into two second segments to keep the frequency resolution the same as for the impact hammer data. These data segments were then normalized by dividing each time segment by its standard deviation ($A'$) and are referred to as $A_{norm}$. The PSD was then calculated by squaring the Fast Fourier Transform (FFT) of each $A_{norm}$ and the five PSDs were then averaged together. Finally, so that the integral of each averaged PSD would equal one, it was divided by the square of its sample rate [23]. This normalized PSD is referred to as $\tilde{A}$.

Figures 4-9 and 4-10 show $\tilde{A}$ for the 7.62 cm schedule 40 test section at average flow speeds of 3.08, 4.96, (Fig. 4-9) 8.05, and 10.8 m/s (Fig. 4-10). Also included is the natural pipe response and a line that indicates the -5/3 characteristic of turbulence decay. At the lower velocities shown in it is possible to see peaks in $\tilde{A}$ that correspond to peaks in the natural pipe response. A notable feature of this plot is that although the $\tilde{A}$ vs. $f$ distribution exhibits a modestly steeper decay than -5/3 at 3.08 and 4.96 m/s ($f^{-2.24}$ at no flow), this decay appears to approach $f^{-5/3}$ as the flow speed increases. Also, between 400-500 Hz, a characteristic rise occurs at both flow speeds due to excitation of the natural pipe response. Because of these corresponding rises, it appears that at these low flow speeds the pipe response is sensitive to excitation in the pipe's natural frequencies.

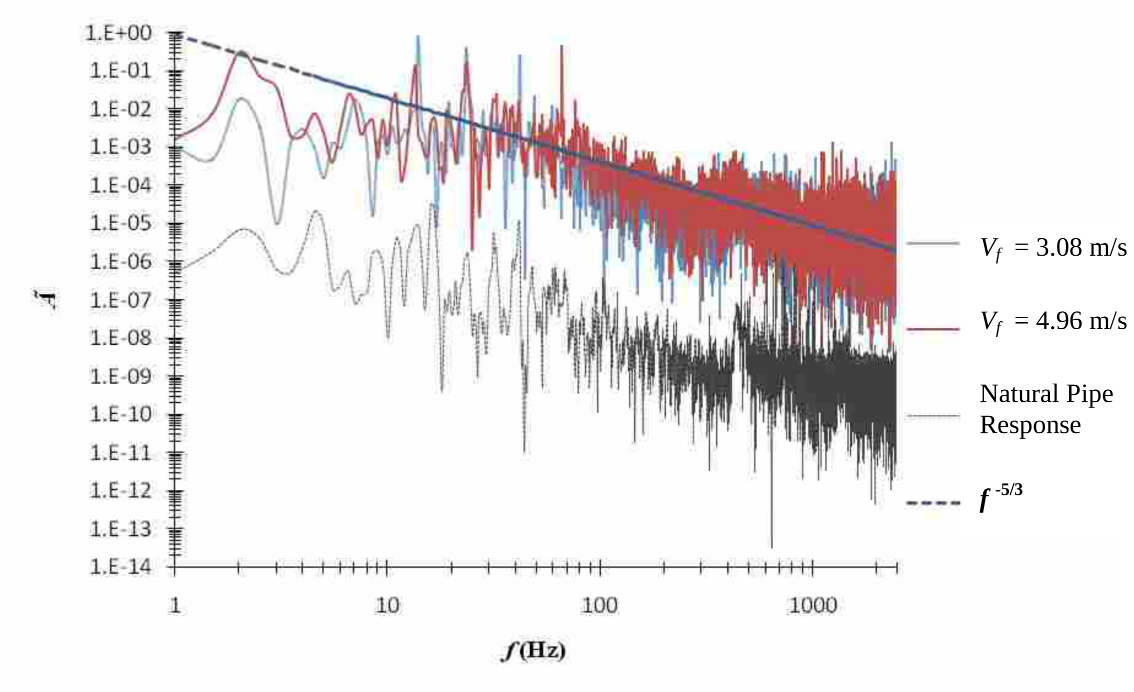

**Figure 4-9: PSD for 7.62 cm schedule 40 test section with flow at speeds of 3.08 and 4.96 m/s. Also included is a line indicating a -5/3 relationship and the natural pipe response for reference.**

At the higher flow speeds shown in Fig. 4-10, the spectra decay with a -5/3 relation and there is little to differentiate the $V_f$ = 8.05 and $V_f$ = 10.78 m/s spectra. Specifically, there is no difference in the slope of the roll-off between the two spectra. Also, the peaks in $\tilde{A}$ at lower velocities associated with the natural pipe response are significantly attenuated at the higher velocities, as is the low frequency content. The data suggest that a greater fraction of the energy exists due to excitation at the natural pipe response or low frequency pipe swaying. This increased low frequency energy content appears to obscure the expected turbulent decay. However, at higher flow speeds, the energy content shifts to a higher frequency range and the pipe vibrations detected by the accelerometers appear to be due to the local turbulent fluctuations at the wall which decay nominally as $f^{-5/3}$.

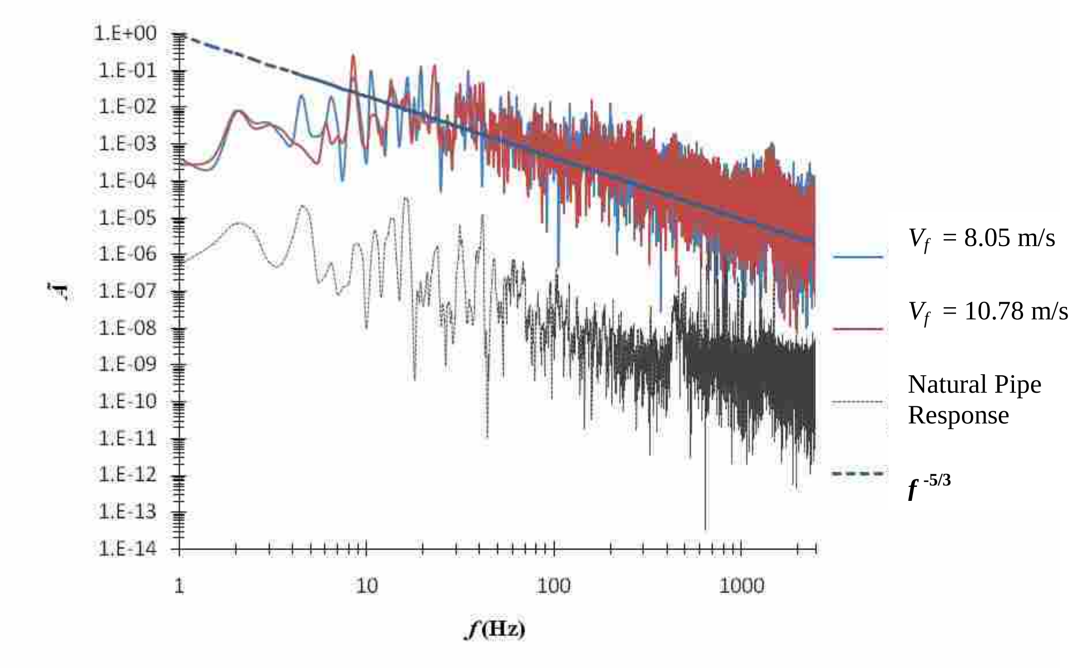

**Figure 4-10: PSD for 7.62 cm schedule 40 test section with flow at speeds of 8.05 and 10.78 m/s. Also included is a line indicating a -5/3 relationship and the natural pipe response for reference.**

Figure 4-11 shows $\tilde{A}$ for the 7.62 cm schedule 40 and 80 test sections at nearly the same flow speed. Decreasing *D/t* from 14.22, for the 7.62 cm schedule 40 test section, to 9.67, for the 7.62 cm schedule 80 test section, does not appear to change the behavior of the spectra. Similar to the data of Figs. 4-9 and 4-10, the decay begins at about 40 Hz and exhibits a decay of nominally $f^{-5/3}$.

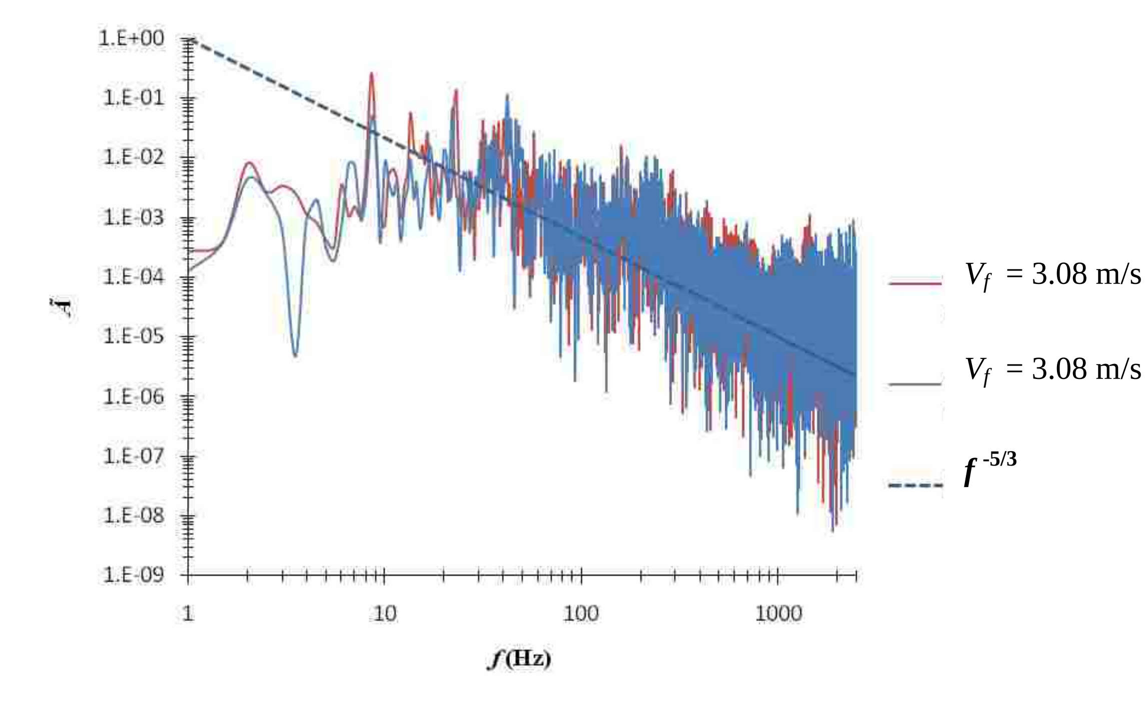

**Figure 4-11: PSD for 7.62 cm schedule 40 and 80 test sections with average flow speeds of 10.78 m/s and 10.98 m/s, respectively. Also included is a line indicating a -5/3 relationship and the natural pipe response for reference.**

Lastly, Fig. 4-12 illustrates the $\tilde{A}$ behavior for the 5.08 cm, 7.62 cm, and 10.16 cm schedule 40 test sections at a nominally constant flow speed of 6.7 m/s. Each $\tilde{A}$ has been multiplied by a base 10 factor (100 for the 5.08 cm test section, 0.1 for the 7.62 cm test section, and $1\text{x}10^{-3}$ for the 10.16 cm test section) to separate the data sets. There is a spike in the $\tilde{A}$ data at about 280 Hz for the 10.16 cm test section due to excitation in the natural pipe response at the same frequency; however the $\tilde{A}$ data from each test section decays nominally as expected. Although not shown, similar to the $\tilde{A}$ data presented in Fig. 4-9, the decay of $\tilde{A}$ is nominally steeper than $f^{-5/3}$ at low flow speeds.

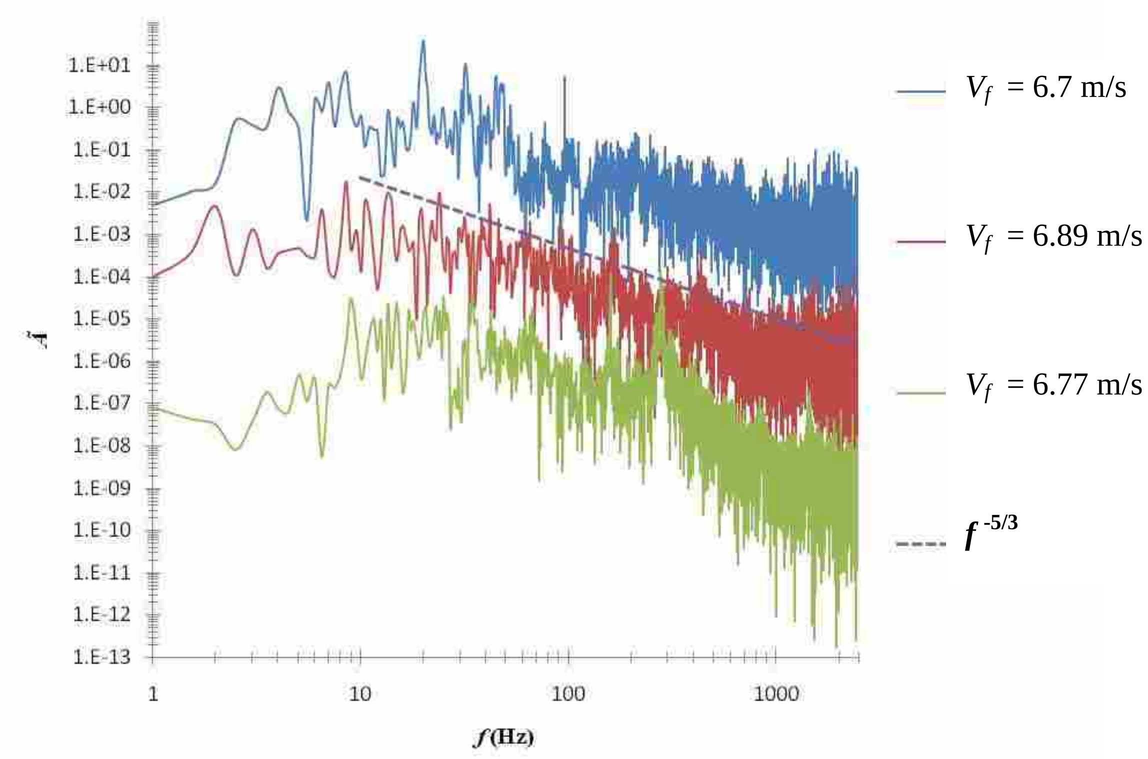

**Figure 4-12: PSD for the 5.08, 7.62, and 10.16 cm schedule 40 test sections at a flow speed of nominally 6.7 m/s. Each data set has been multiplied by 100 (5.08 cm test section), 0.1 (7.62 cm test section), and 1x10$^{-3}$ (10.16 cm test section) to allow each data set to be delineated.**

To summarize, it was shown in this section that for a pipe with no clamping supports, $P'$ scales with $A'$, which in turn scales with the fluid dynamic pressure ($\sim V_f^2$). It was also shown that $V'$ scales with $V_f^{1.6}$. Also, $A'$ was observed to increase with increased $D/t$. Finally, $\tilde{A}$ is influenced by to the natural pipe response at low flow speeds and was observed to decay steeper than $f^{-5/3}$. At high flow speeds, however, $\tilde{A}$ is less sensitive to the natural pipe response and the pipe vibrations appear to be due to local turbulent fluctuations which decay nominally as $f^{-5/3}$.

## 4.2 Pipe Wall Supports

### 4.2.1 Pipe Vibration vs. Support Length for the 10.16 cm Schedule 40 Pipe

Subsequent to the experiments in the unsupported test sections, experiments were conducted employing the wall mounted clamp supports as described in section 3.6 to investigate the influence of support length on *A'*. Figure 4-13 illustrates how *A'* varies with the six support separation lengths in the 10.16 cm schedule 40 test section. For the experiments, accelerometers were placed exactly half way between the supports. Similar to the no wall support cases, these data exhibit a power law dependency ($A' \sim V_f^m$) above a flow speed of 3.5 m/s. The value of *m* here varies from 1.97 to 2.89 with an average value of 2.34. For the no support and full support cases *m* is very near 2.0, while the half and quarter support cases exhibit values of $m \approx 2.19$ and 2.18, respectively. The shortest support cases (eighth and sixteenth) however, have values of *m* approaching 3.0 (2.72 and 2.89, respectively) indicating that the magnitude of *A'* exhibits a greater dependence on $V_f$ when the support length is very short. Although there is some variation in the value of *m* with clamp support length, it can be seen that each data series is quite similar, with the magnitude of *A'* being the least for the full support case at high flow speeds.

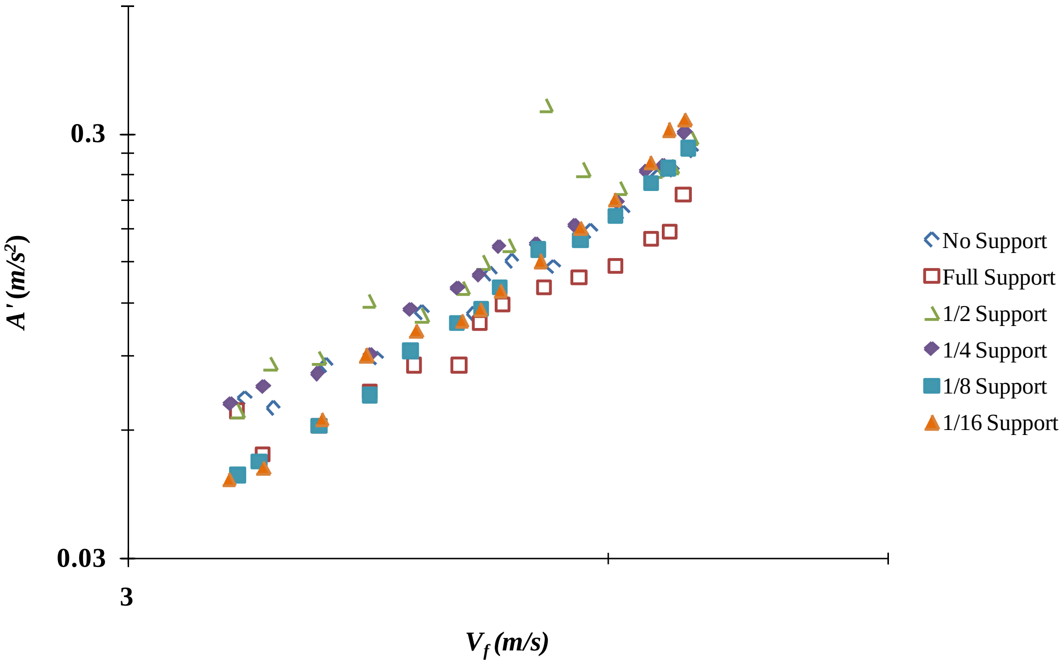

**Figure 4-13:** ***A'*** **as a function of** $V_f$ **for various wall support distances in the 10.16 schedule 40 test section.**

Figure 4-14 illustrates how *A'* varies with pipe clamp support length to pipe diameter ratio (*L/D*) at four flow speeds (3.51 m/s, 4.26 m/s, 5.78 m/s and 6.73 m/s). At flow speeds of 6.73 m/s and 5.78 m/s, it appears that the magnitude of *A'* slightly increases as *L/D* decreases ($A' \sim (L/D)^{-0.07}$), however at the lower flow speed of 3.51 m/s, *A'* appears to slightly decrease as *L/D* decreases ($A' \sim (L/D)^{0.14}$) and is nominally flat at a flow speed of 4.26 m/s. However, the *A'* dependence on pipe clamp length appears to be modest and not constant with *L/D* or average flow speed.

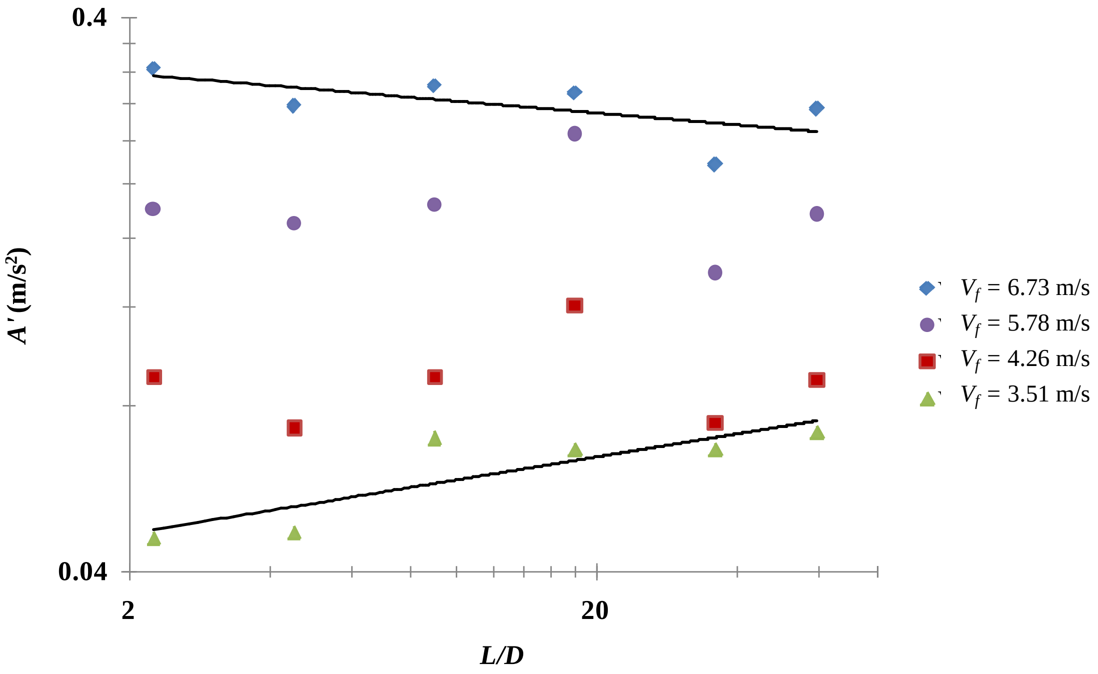

**Figure 4-14: *A'* as a function of *L/D* for four flow speeds in the 10.16 cm schedule 40 test section. The solid lines represent the trend in the data at $V_f$=6.73 and 3.51 m/s**

The influence of *L/D* on *V’* is notably different than for the *A’* data. Figure 4-15 gives *V’* as a function of $V_f$ for six pipe clamping length support scenarios and with the 10.16 cm schedule 40 test section. The values of *m* ($V' \sim V_f^m$) vary from 1.01 to 1.77 with an average value, over the six clamping lengths, of 1.42. The average of *m* is about 1.65 for the longest wall support cases, but drops to an average of 1.11 for the eighth and sixteenth support cases. This is in contrast to the *A’* data where a modest increase with decreasing support length was observed. Further, the data illustrate that the magnitude of *V’* decreases as the distance between the wall supports decreases. This is also apparent in Fig. 4-16 which illustrates how *V’* varies with *L/D* at four constant flow speeds. Also evident in Fig. 4-16 is an increase in the magnitude of *V’* with $V_f$ and *L/D*.

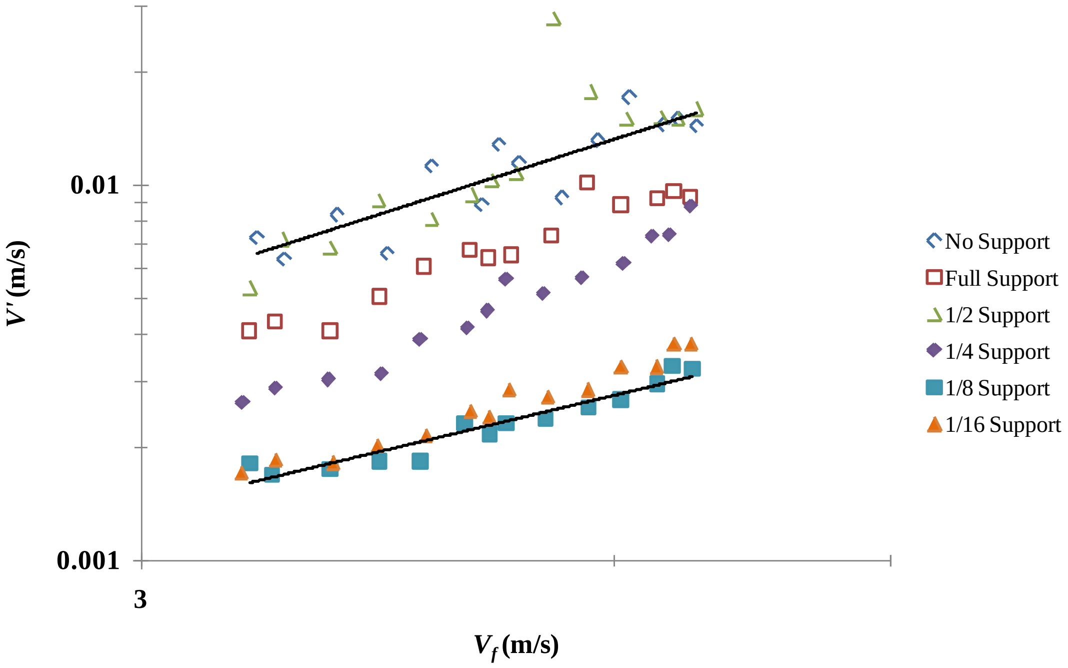

**Figure 4-15:** ***V'*** **as a function of** ***$V_f$*** **for each pipe clamp length in the 10.16 cm schedule 40 test section. The solid lines illustrate how** ***V'*** **trends with** ***$V_f$*****.**

The difference in the behavior of the *A'* and *V'* data is important. Although the *A'* vs. $V_f$ data are quite similar for all pipe clamp lengths, the *V'* vs. $V_f$ data show notable differences. At shorter clamping length the pipe velocity is reduced whereas the pipe acceleration remains nominally the same as for the long pipe. It should be noted, however, that the wall supports are not perfect boundary conditions. Several meters of pipe exist on either side of the supports which may mean that a stronger *L/D* relationship may be confounded by bending and other vibrational pipe modes that may be transmitted through the pipe due to the extra length of pipe on either side of the supports. The clamping length cases that will be examined in more detail through the rest of this thesis are the no support case (freely hung), full wall support case, and quarter wall support case.

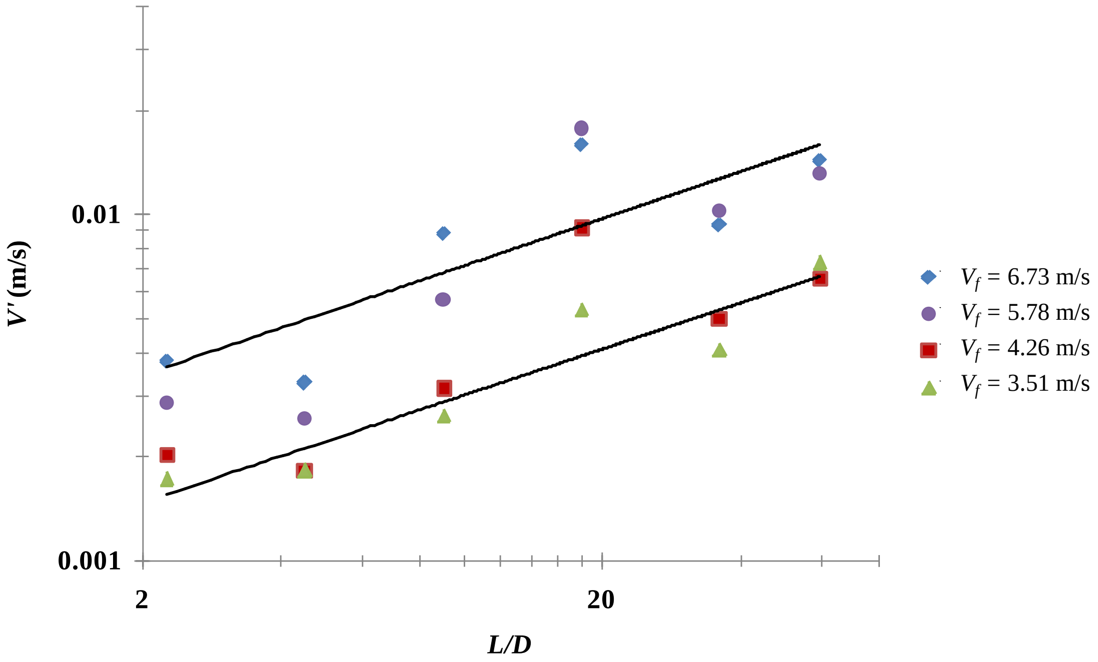

**Figure 4-16: $V'$ as a function of $L/D$ for four flow speeds in the 10.16 cm schedule 40 test section. The solid lines represent the trend in the data at $V_f$ =6.73 and 3.51 m/s.**

### 4.2.2 Pipe Vibration for Varying Clamping Lengths and all Test Sections

The effect of clamp support length on *A'* and *V'* for each test section was also investigated. As described in section 3.6, a 3.69 m subsection was defined in each test section beginning 1.07 m from the test section entrance. This 3.69 m subsection is what is considered a full support length. The downstream wall support was then moved to a quarter of the full support length (quarter support). An accelerometer was then placed half way between the wall supports. For the no support case, the accelerometer remained in the same position as for the full support case.

It is important to recall that for the 5.08 cm diameter test sections, developing regions of both $D$ = 5.08 cm and 10.16 cm were employed. This was done to explore contraction effects when transitioning from a larger diameter pipe to a smaller diameter pipe. Figure 4-17 presents $A'$ vs. $V_f$ in the 5.08 cm test section. Two sets of data are shown; one corresponding to the condition where the upstream pipe contracts from 10.16 cm and the other where no contraction exists. The data of Fig. 4-17 illustrate that the contraction exerts negligible influence on the magnitude of $A'$ for the no wall support case. The full wall support case exhibits similar behavior. For the quarter wall support case, a modest increase in $A'$ is observed for the condition where the contraction exists. The implication here is that using either developing region should not appreciably affect the data. Generally, a contraction was avoided in all experiments, except for the baffle plate experiments described in section 4.3 where the developing region was always $D$ = 10.16 cm.

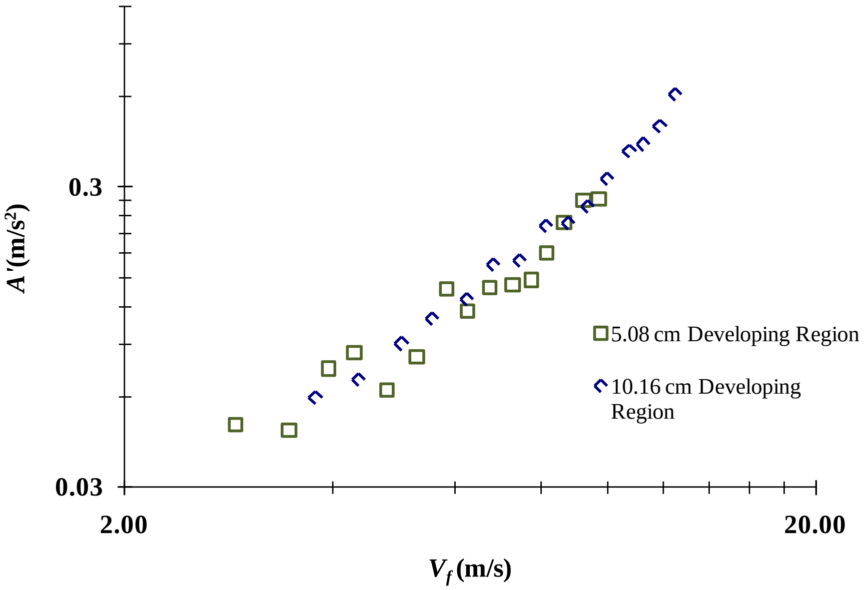

**Figure 4-17: *A'* as a function of $V_f$ for the *D* = 5.08 cm schedule 80 test section with *D* = 5.08 cm and 10.16 cm developing regions and for the unsupported pipe case.**

Conducting experiments on each test section with the three wall support conditions described above (no support, full support, and quarter support) yield the similar power law behavior described for the unsupported pipe. Table 4-1 lists the average value of all six test section power law fit exponents (*A'* and *V'* ~ $V_f^m$), *m*, under the three clamping conditions. It also shows the standard deviation in *m* between each of the six test sections. The standard deviations for the *V'* data is the greatest, however (except for the standard deviation in the values of *m* for the quarter support *V'* data) the values of *m* are within one standard deviation of the mean values presented in Table 4-1. A 3% difference in the value *m* for the *A'* data between the no clamp support case and the full clamp support case exists and very little difference in the behavior of the two data sets is observed when it is plotted. There is however, a modest increase of the value of *m* for the quarter wall support case when compared to the no wall support case. This is consistent with the behavior observed in section 4.2.1 for the 10.16 cm schedule 40 test section.

**Table 4-1: Average of each of the six test section power law exponents, *m*, (*A'* and *V'* ~ $V_f^m$) for each of the three clamping support lengths (no clamping, full clamping, and quarter clamping). Also displayed is the standard deviation of *m* over the six test sections.**

| | *m* | | | |
|---|---|---|---|---|
| | ***A'*** | ***σ*** | ***V'*** | ***σ*** |
| **No Wall Support** | 1.97 | 0.09 | 1.64 | 0.33 |
| **Full Wall Support** | 1.92 | 0.2 | 1.44 | 0.32 |
| **Quarter Wall Support** | 2.26 | 0.22 | 1.40 | 0.38 |

The behavior observed in section 4.2.1 also appears to hold for *V'* where *m* is observed to decrease with decreasing *L/D*. The value of *m* for the no wall support case is nominally 1.60 with a 14% and 17 % decrease in the value of *m* for the full and quarter wall support cases, respectively.

Figure 4-18 compares the dependence of *A'* on the ratio *D/t* for each test section at the three clamp support lengths and a constant flow speed of 6.70 m/s. For all three pipe diameters, the data exhibit an increase in the magnitude of *A'* as *D/t* increases. The *A'* vs. *D/t* behavior is nominally the same for all three clamp lengths for the *D* = 7.62 cm conditions with a smaller magnitude than the other pipe diameters. The greatest spread exists for the *D* = 10.16 cm pipe diameter. Although the data presented in Fig. 4-18 is at the same flow speed (6.7 m/s) the flow rates for these pipe diameters vary, with the lowest flow in the 5.08 cm test sections and the highest in the 10.16 cm test sections. It can be seen that the *D/t* dependence on *A'* is not constant with fluid speed. It is also apparent that *D/t* ratio on *A'* is not constant with support length, suggesting differences in the pipe response are caused by the pipe clamp support length. This was also evident in the data presented in Fig. 4-14.

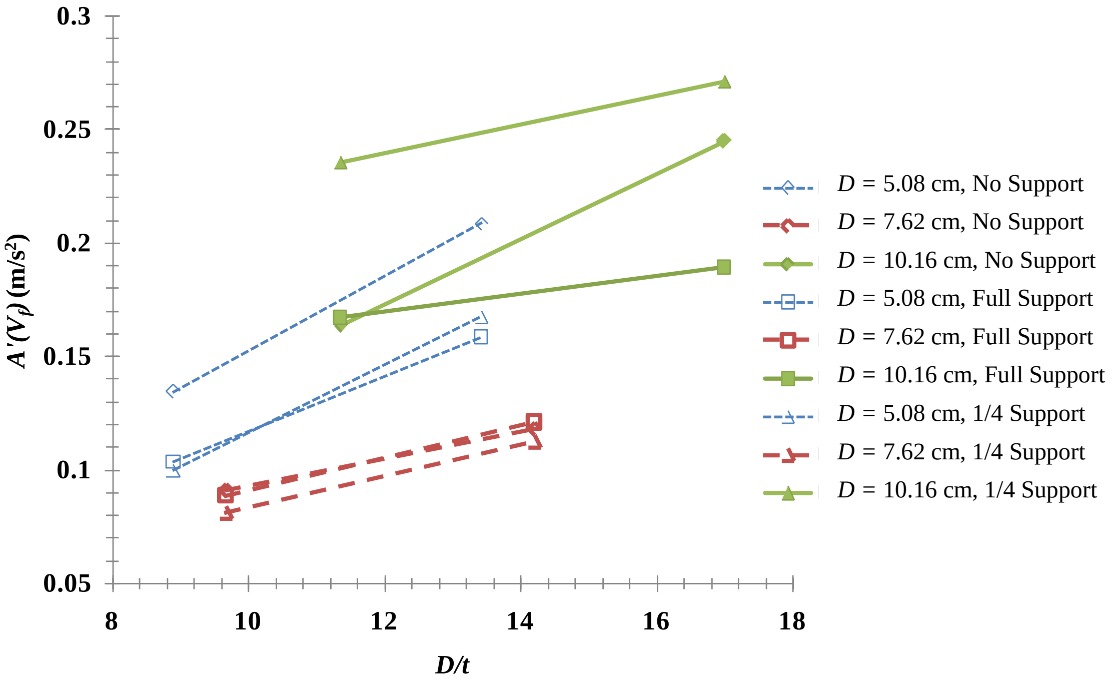

**Figure 4-18: *A'* vs. *D/t* at a flow speed of 6.70 m/s for each test section diameter (5.08 cm, 7.62 cm, and 10.16 cm) and the three clamping support lengths (no support, full support, quarter support).**

To summarize, it was observed in the previous section that the dependence of *A'* on *D/t* is not constant with flow rate, and that *A'* is also influenced only weakly by *L/D*. *L/D* does, however, have a greater influence on *V'*, where *V'* generally increases as *L/D* decreases. It was also observed that *V'* has a decreasing dependence on $V_f$ as the clamping length decreases.

### 4.2.3 Accelerometer Spectra for Varying *L/D*

The accelerometer spectra for varying clamping lengths are now briefly explored. Figure 4-19 shows a comparison of $\tilde{A}$ for the unsupported and quarter supported 7.62 cm schedule 40 test section. The flow speed for both support conditions is nominally 10.8 m/s. $\tilde{A}$ has been multiplied by 1 x $10^3$ to separate the data sets on the figure for easier comparison. The most apparent difference between the unsupported and quarter support data is that the quarter support data exhibits a broad local rise in $\tilde{A}$ from about 40-70 Hz. This broad increase appears to be due to excitation in the natural pipe response in this same frequency range. This behavior is observed in all flow speeds, but becomes more distinguishable as flow speed increases. Above this frequency, the decay in $\tilde{A}$ follows the same pattern observed in the unsupported test section data. Namely, the decay is steeper than an $f^{-5/3}$ power law at low velocities, and approaches an $f^{-5/3}$ decay as velocity increases.

It is also apparent from the data of Fig. 4-19 that low frequency vibrations have been significantly attenuated in the quarter wall support length. This short wall clamping length appears to behave somewhat as a high pass filter. The data suggests that the pipe response is more strongly influenced by the natural pipe response for the quarter support case than for the unsupported case (Fig. 4-10). This likely occurs because the natural pipe response for the quarter support case contains more energy at higher frequencies. This sensitivity to the natural pipe response at short separation distances may hamper the ability to infer turbulent flow behavior at the pipe wall.

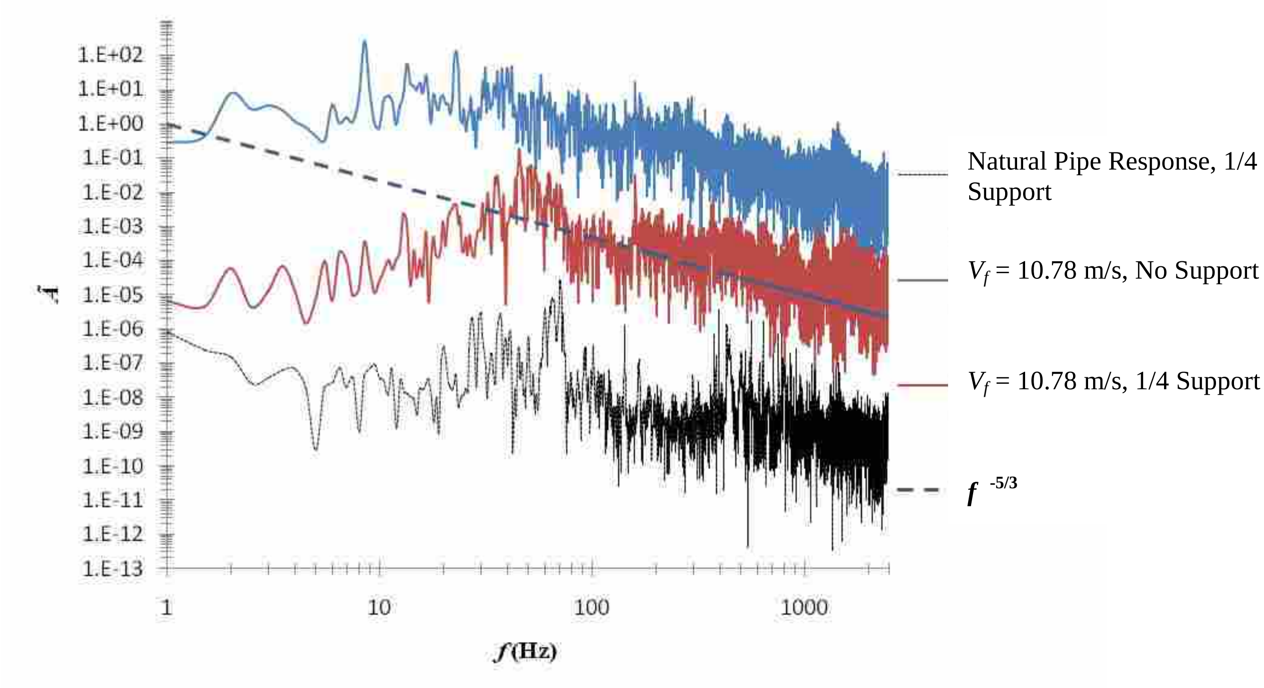

**Figure 4-19: Comparison of $\tilde{A}$ vs. $f$ for unsupported and quarter support 7.62 cm schedule 40 test sections with a flow speed of 10.78 m/s. The unsupported case has been multiplied by 1000 to make comparison easier.**

Although not shown, the full support case exhibits similar behavior and sensitivity to the natural pipe response as the unsupported case, suggesting that there is little difference in the observed behavior of *A'* between the unsupported case and the longest wall support case (full wall support). This appears to signify that the distance between wall supports affects the pipe wall acceleration more as the distance between the supports becomes shorter.

## 4.3 Non-dimensionalization of *A’*

It has been previously shown that *A’* scales nominally as $V_f^2$ and *D/t*. In general, the rms of the pipe wall acceleration can be written as a function of all the variables that exert influence:

$$A^{'} = f\left(V_f, D, t, L, \rho, \mu, \rho_{eq}, \omega_n, E\right) \tag{4-3}$$

where $\omega_n$ is a natural frequency of each pipe section and contains dependence of the pipe material modulus, *E*, and $\rho_{eq}$ is the equivalent density of the water filled pipe, which is defined as [24]

$$\rho_{eq} = \frac{\rho\pi\left(\frac{D}{2}\right)^2 + \rho_p 2\pi\left(\frac{D}{2}+\frac{t}{2}\right)t}{2\pi t\left(\frac{D}{2}+\frac{t}{2}\right)} \tag{4-4}$$

Recasting this set of dimensional variables into non-dimensional form following the standard approach yields the following set of non-dimensional variables.

$$A^{*} = \frac{A^{'}t}{V_f^2} \tag{4-5}$$

$$Re = \frac{\rho V_f D}{\mu} \tag{4-6}$$

$$t^{*} = \frac{t}{D} \tag{4-7}$$

$$L^{*} = \frac{L}{D} \tag{4-8}$$

$$\rho^{*} = \frac{\rho_{eq}}{\rho} \tag{4-9}$$

$$E^* = \frac{E}{\rho V_f^2} \tag{4-10}$$

$$\omega^* = \frac{\omega_n D}{V_f} \tag{4-11}$$

The natural frequency for pipe bending, $\omega_n$, should scale as:

$$\omega_n \sim \frac{D}{L^2}\sqrt{\frac{E}{\rho_{eq}}} \tag{4-12}$$

Whereas for radial expansion and compression modes it should scale as:

$$\omega_n \sim \frac{1}{D}\sqrt{\frac{Et}{D\rho_{eq}}} \tag{4-13}$$

The non-dimensional pipe acceleration can then be expressed as a function of the non-dimensional variables listed in Eqs. 4-5 to 4-10:

$$A^* = f(Re, t^*, L^*, \rho^*, E^*, \omega^*) \tag{4-14}$$

In a parallel numerical investigation of this same phenomena, Shurtz observed that the $A^*$ normalization is the appropriate non-dimensionalization of $A'$ [24]. By holding all of the non-dimensional variables listed in Eqs. 4-6 to 4-11 constant while varying one at a time, Shurtz [24] was able to determine the first order effects of each of the non-dimensional variables on $A^*$. These effects are listed in Table 4-2 as power law fits of data ($A^* \sim Z^{*m}$) that was obtained using a numerical model, where $Z^*$is one of the non-dimensional variables listed in Eqs. 4-6 to 4-11. The table shows that all of the non-dimensional variables, except $\rho^*$, have a very weak influence of $A^*$. In the present experiments it is impossible to hold all but one of the pipe non-dimensional independent parameters constant. However, it is still useful to explore how $A^*$ depends on each parameter.

**Table 4-2: The values of $m$ corresponding to $A^* \sim Z^{*m}$ power law determined by a numerical simulation of flow induced pipe vibrations presented by Shurtz [24].**

| | $A^*$ |
|---|---|
| $Re$ | -0.18 |
| $t^*$ | 0.04 |
| $L^*$ | -0.16 |
| $\rho^*$ | -1.00 |
| $E^*$ | 0.10 |
| $\omega^*$ | -0.35 |

Figure 4-20 illustrates $A^*$ as a function of $Re$ for the six test sections examined, for the unsupported scenario and for $2\text{x}10^5 \leq Re \leq 8\text{x}10^5$. The magnitude of $A^*$ for the 10.16 cm test sections is greater than for the 7.62 cm and 5.08 cm test sections. It is also apparent that the $A^*$ data for the 10.16 cm test sections collapse onto each other and appear nominally flat. The $A^*$ data for each of the 7.62 cm and 5.08 cm test sections are also observed to collapse onto each other, but appear to decrease slightly with increasing $Re$. The values of $m$ corresponding to $A^* \sim Re^m$ power law fits to the data show that the dependence of $A^*$ on $Re$ is nominally very weak ($m \sim -0.018$). The weak dependence of $A^*$ on $Re$ implies that $A^*$ is nominally constant with $Re$ when the test section is unclamped.

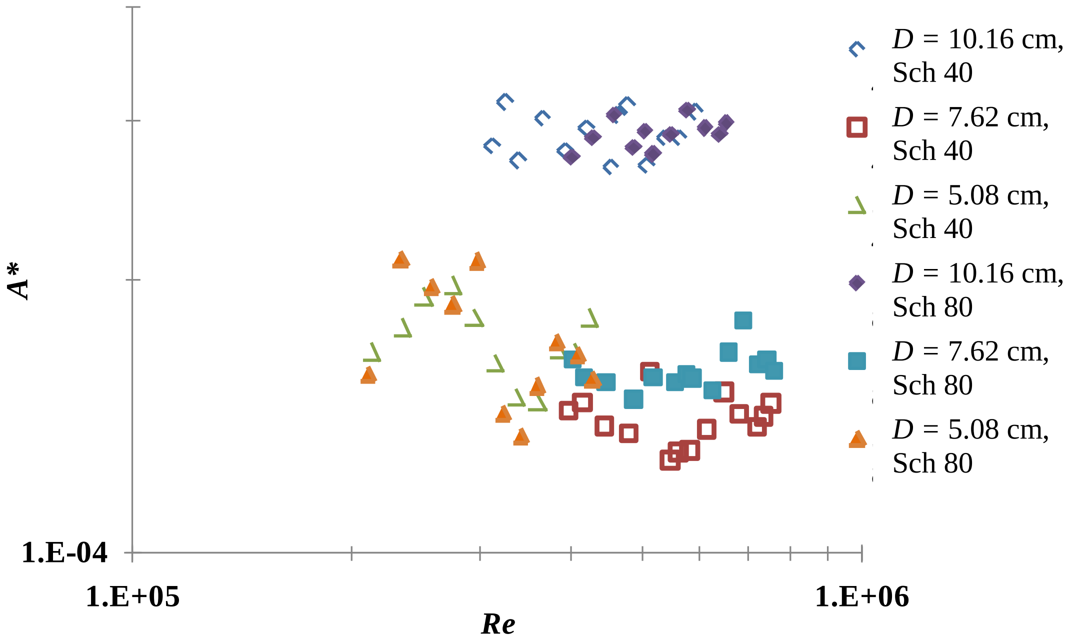

**Figure 4-20: *A** vs. *Re* for each of the six test sections considered and for no clamping support.**

Figure 4-21 illustrates the same conditions as Fig. 4-20 for the full clamp support case. The magnitude of the $A^*$ data for the 10.16 cm schedule 80 test section is greater than for the 10.16 cm schedule 40 test section. The magnitude of $A^*$ for the 7.62 cm test sections (which collapse onto each other) is also slightly greater than for the 5.08 cm test sections (which also collapse onto each other). The values of $m$ corresponding to $A^* \sim Re^m$ power law fits to the data show that the depedence of $A^*$ on $Re$ is also nominally very weak for the full clamp support ($m$ ~ -0.021).

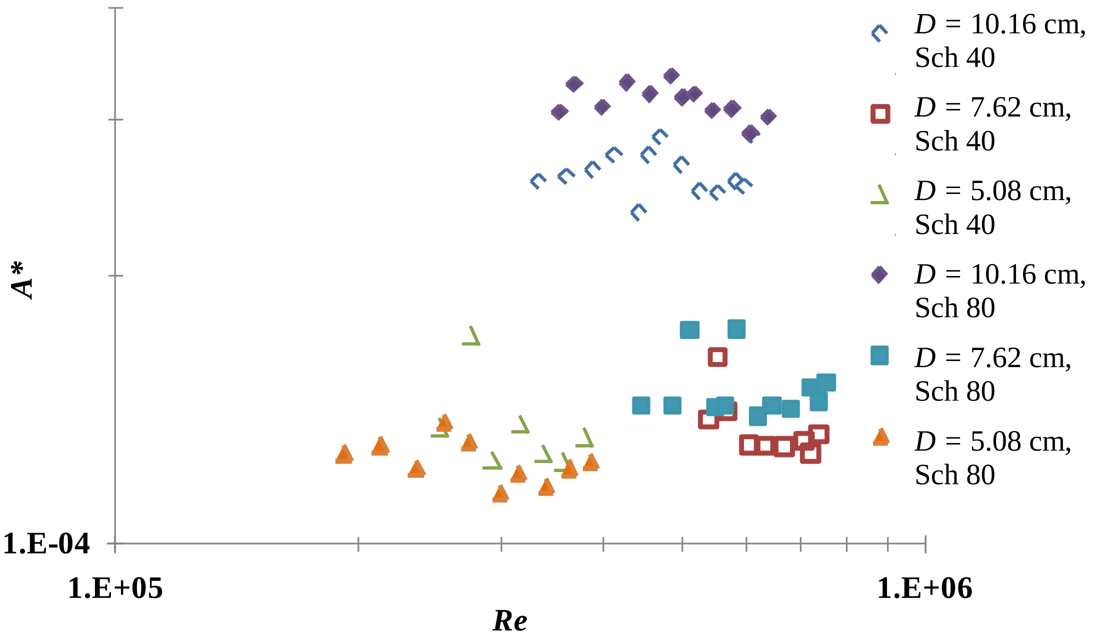

**Figure 4-21: *A** vs. *Re* for each of the six test sections considered and for full clamping support.**

Figure 4-22 illustrates the same conditions as Fig. 4-20 for the quarter clamp support case. The magnitude of $A^*$ for the 10.16 cm test sections with the quarter clamping length is greater than for the same test sections with longer clamping lengths. Also, $A^*$ exhibits a slight increase in its dependence on *Re* for the 7.62 cm and 5.08 cm test sections. The values of *m* corresponding to $A^* \sim Re^m$ power law fits to the data show that the dependence of $A^*$ increases nominally at $m \sim 0.22$ with increasing *Re* and is listed in Table 4-3.

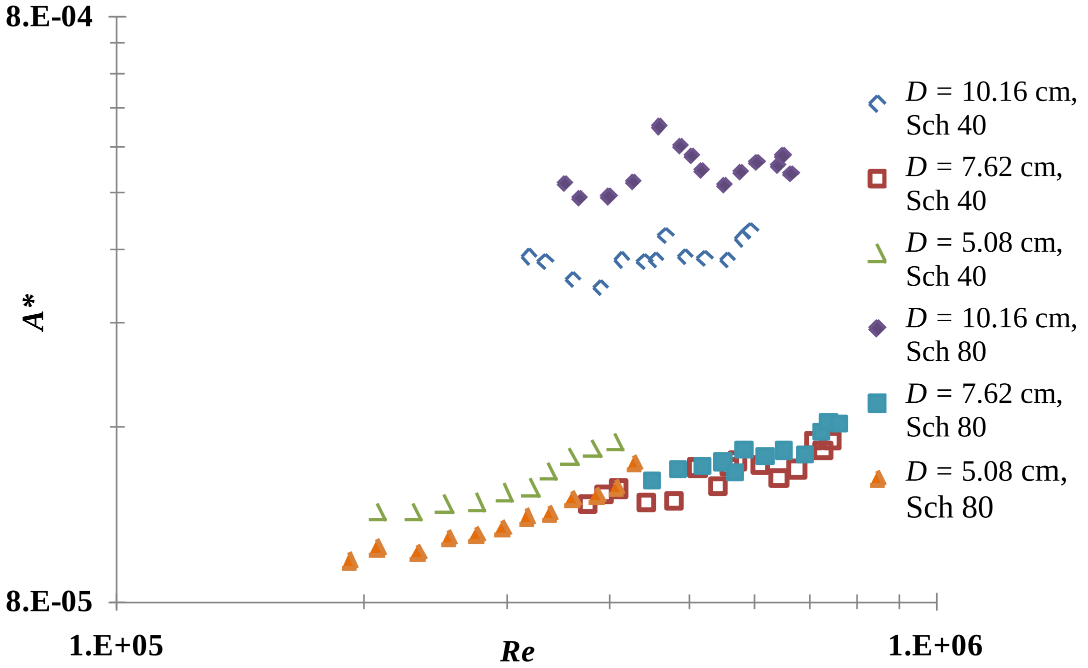

**Figure 4-22: *A** vs. *Re* for each of the six test sections considered and for the quarter clamping support.**

Table 4-3 lists the values of *m* corresponding to $A^* \sim Re^m$ power law fits to the data for each of the six test sections considered and for the three clamp support lengths (no support, full support, and quarter support). There appears to be no systematic pattern in the variation of the values of *m* among the test sections. However, on average there is no statistically significant difference in the values of *m* for the no support case and full support case and the average values of *m* suggest no dependence of $A^*$ on *Re*. In contrast, for the quarter clamping case a modest dependence on *Re* appears.

**Table 4-3: The values of *m* corresponding to $A^*\sim Re^m$ power law for each of the six test sections considered and the three clamping support lengths.**

| ***m*** | **Clamping Support Condition** | | |
|---|---|---|---|
| | **No** | **Full** | **Quarter** |
| **10.16 cm, Sch 40** | 0.012 | 0.157 | 0.12 |
| **10.16 cm, Sch 80** | 0.137 | -0.11 | 0.053 |
| **7.62 cm, Sch 40** | -0.09 | 0.012 | 0.189 |
| **7.62 cm, Sch 80** | 0.015 | -0.08 | 0.204 |
| **5.08 cm, Sch 40** | -0.11 | 0.094 | 0.41 |
| **5.08 cm, Sch 80** | -0.07 | -0.2 | 0.322 |
| **Average** | -0.018 | -0.021 | 0.22 |

The dependence of $A^*$ on *Re* is slightly different than that observed in the numerical simulations of Shurtz [24]. This is likely due to the fact that Shurtz considered a hydraulically smooth pipe and the results of the experiments show that the pipes employed exhibit behavior characteristic of rough pipes where the influence of *Re* is less pronounced.

The dependence of $A^*$ on $E^*$, $\omega^*_{bend}$, and $\omega^*_{radial}$ is nearly identical to that described above for *Re*. Namely, for the unsupported and full support scenarios no statistically significant variation of $A^*$ with each of the parameters exists. However, for the quarter support case a modest dependence exists in the data. In fact, for $\omega^*_{bend}$ and $\omega^*_{radial}$, the power-law fit exponents are very similar to those listed in Table 4-3 for *Re*. For $E^*$ the power law fit exponents are very nearly one half of those listed in Table 4-3 for *Re*.

Figure 4-23 illustrates $A^*$ as a function of $t^*$ for each of the three unsupported test section diameters. The values of $A^*$ for each respective test section have been averaged over a range of *Re* where negligible variation exists ($2\text{x}10^5 \leq Re \leq 8\text{x}10^5$). As with the $A^*$ vs. *Re* data, the magnitude of $A^*$ for the 10.16 cm test sections is greater than for the 5.08 cm test sections, which is also greater than for the 7.62 cm test sections. Also, $A^*$ appears nominally flat for the 10.16 cm and 5.08 cm test sections and modestly increases its dependence on $t^*$ for the 7.62 cm test sections. The values of *m* corresponding to $A^* \sim t^{*m}$ power law fits of the data show that the dependence of $A^*$ on $t^*$ is very weak ($m \sim 0.08$). This value is twice the value predicted by Shurtz [24], listed in Table 4-2.

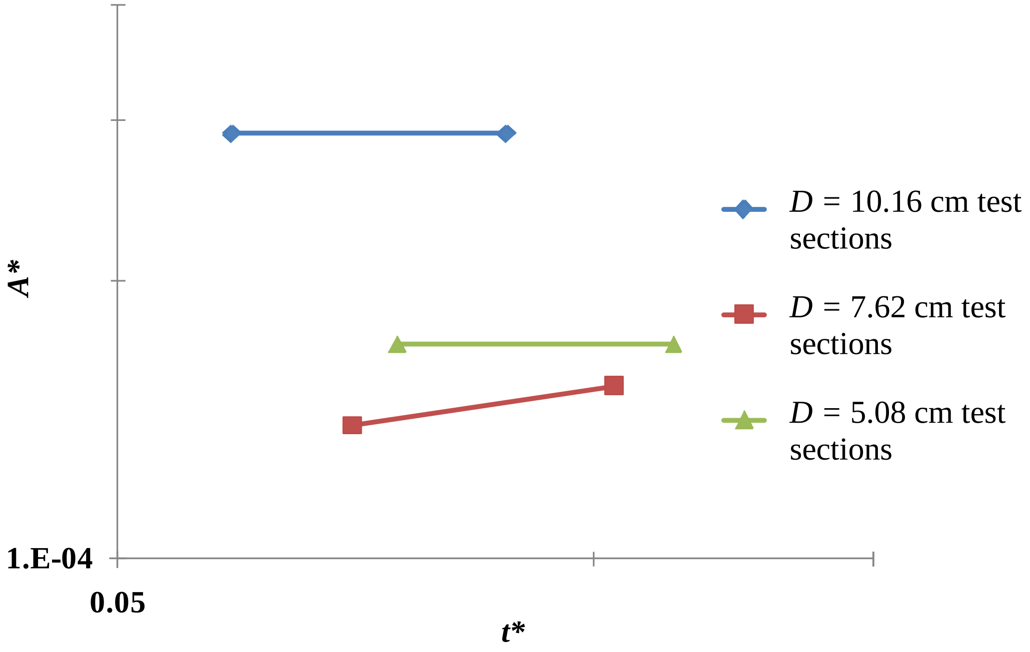

**Figure 4-23: $A^*$ vs. $t^*$ for the three pipe diameters for the unsupported pipe. The values of $A^*$ have been averaged over a range of *Re* where there was little variation in $A^*$.**

Figure 4-24 now illustrates $A^*$ as a function of $\rho^*$ for each of the three unsupported test section diameters. Like in Fig. 4-23, the values of $A^*$ for each respective test section have been averaged over the same *Re* range as listed for Fig. 4-23. The data shown in this figure also show the same pattern in the relative magnitudes of $A^*$ as was shown in Fig. 4-23. Specifically, the magnitude of $A^*$ is greatest for the 10.16 cm test sections followed by the 5.08 cm test sections and then by the 7.62 cm test sections. The values of *m* corresponding to $A^* \sim \rho^{*m}$ power law fits of the data show that the dependence of $A^*$ decreases as $\rho^*$ increases (nominally $m \sim -0.22$). Shurtz predicts a value of *m* of -1.0 [24]. Shurtz obtained this value by using a wider range in $\rho^*$ and by changing $\rho^*$ while keeping *D* and *t* the same [24], which was not possible to do for this research.

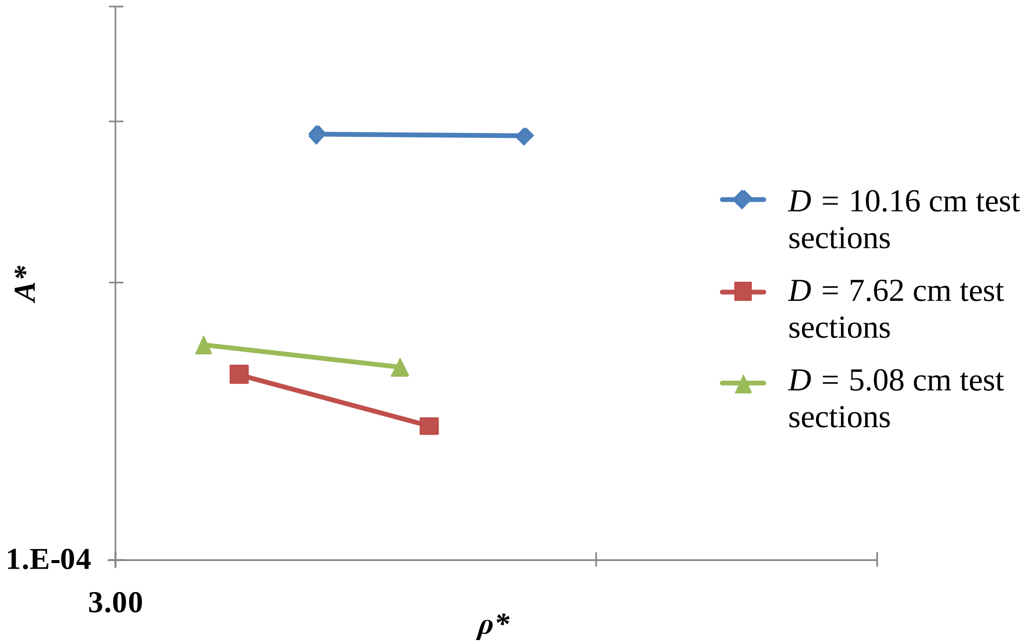

**Figure 4-24: $A^*$ vs. $\rho^*$ for the three pipe diameters for the unsupported pipe. The values of $A^*$ have been averaged over a range of *Re* where there was little variation in $A^*$.**

The results of the numerical investigation of Shurtz suggests that to a first order the pipe wall vibrations should scale as $A' \sim V_f^2/t^* \rho^*$ for an unsupported pipe [24]. Figures 4-25 and 4-26 illustrate $A'$ as a function of only $V_f^2/t$ and then of $V_f^2/t^* \rho^*$, respectively.

Figure 4-25 shows $A'$ as a function of $V_f^2/t$ for each of the six unsupported test sections considered. This figure also includes linear fits to the data with a zero intercept that pass through the schedule 40 and 80 test section data for each pipe diameter (10.16 cm, 7.62 cm, and 5.08 cm). This functional relationship causes $A'$ for the schedule 40 and 80 data from each diameter test section to collapse onto each other. This relationship does not, however, collapse the three pipe diameters onto each other. The magnitude of the collapsed 10.16 cm data is nominally twice the magnitude of the collapsed 5.08 cm data at a given $V_f^2/t$. Also, the magnitude of the collapsed 7.62 cm data is nominally 20% greater than the collapsed 5.08 cm data at a given $V_f^2/t$. The average of the values of $m$ corresponding to $A' \sim (V_f^2/t)^m$ power law fits for each of the six test sections is very nearly linear ($m \sim 0.99$), justifying the linear fit curves. Because this functional relationship does not collapse the $A'$ data for the three pipe diameters onto each other, there is some other parameter that influences the behavior of $A'$ that has not yet been captured. It is expected that the $A' \sim V_f^2/t^* \rho^*$ relationship will capture more of that behavior and cause a better collapse of the data.

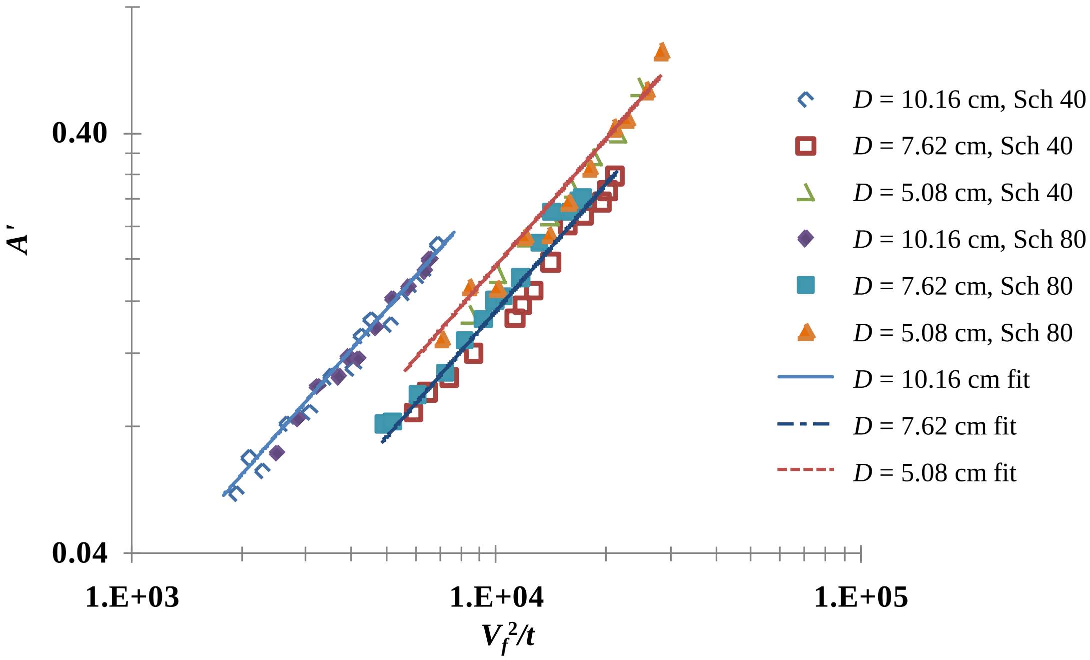

**Figure 4-25: *A'* vs. $V_f^2/t$ for each of the six unsupported test sections considered. Linear fit lines with zero intercept pass through the schedule 40 and 80 pipe section data for each diameter.**

Shown in Fig. 4-26 is *A'* as a function of $V_f^2/t^*\rho^*$ for each of the six unsupported test sections considered. This figure also includes linear fit curves with a zero intercept that pass through the schedule 40 and 80 test section data for each pipe diameter (10.16 cm, 7.62 cm, and 5.08 cm). This functional relationship does not cause as tight of a collapse of the schedule 40 and 80 data from the 10.16 cm and 5.08 cm diameter test sections as shown in Fig. 4-25. It does, however, cause the data from the 10.16 cm and 5.08 cm test sections to collapse onto each other. The 7.62 cm schedule 40 and 80 data also collapse onto each other, however, the magnitude of this collapsed data is nominally half of the 10.16 cm and 5.08 cm collapsed data. As illustrated by the linear fit lines, the 10.16 cm and 5.08 cm data collapse shown in Fig. 4-26 is tighter than the collapse of the

7.62 cm and 5.08 cm data shown in Fig. 4-25. This appears to imply that the parameter $V_f^2/t^*\rho^*$ captures more of the behavior of *A'* than the parameter $V_f^2/t$.

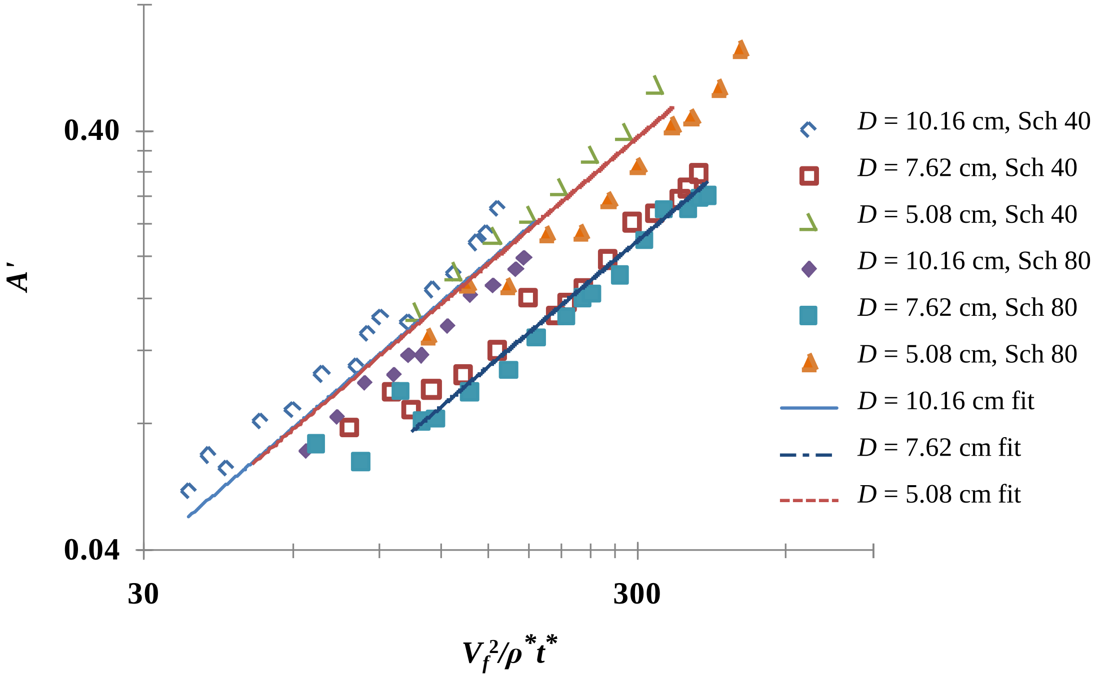

**Figure 4-26: *A'* vs. $V_f^2/\rho^*t^*$ for each of the six unsupported test sections considered. Linear fit lines with zero intercept pass through the schedule 40 and 80 pipe section data for each diameter test section.**

Figure 4-27 shows *A'* as a function of $V_f^2/t^*\rho^*$ for the data presented by Pittard *et al.* [2]. This functional relationship causes *A'* for each pipe material and diameter (except for the 3.81 cm stainless steel test section) to collapse onto one another. What is interesting to note is that although these data were collected from a different facility and the pipe moduli and densities vary greatly, the functional relationship, $A' \sim V_f^2/t^*\rho^*$, works very well to collapse most of the data.

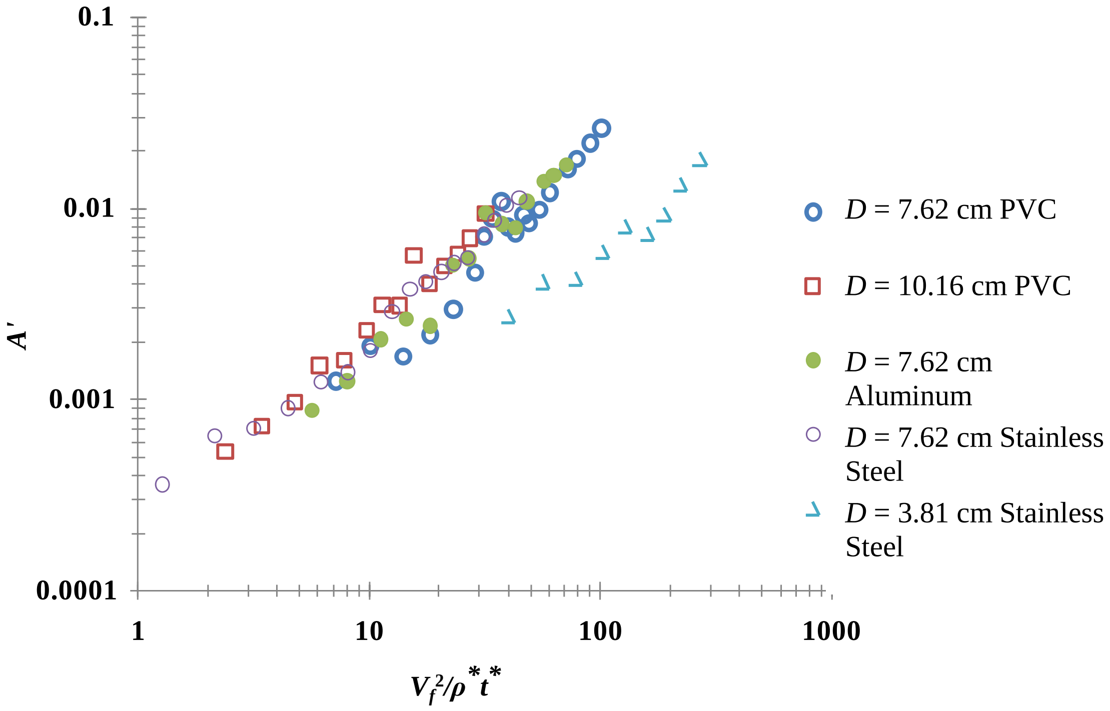

**Figure 4-27: *A'* vs. $V_f^2/\rho^* t^*$ for the data presented by Pittard *et al.* [2].**

Lastly, Figure 4-28 illustrates *A'* as a function of the correlation $V_f^{2.12}\beta D^{1.9}$ for each of the six unsupported test sections considered, where $\beta$ is defined in Eq. 2-7. Figure 4-29 shows the same correlation applied to the data presented by Pittard *et al.* [2]. This correlation was developed previously by performing a statistical analysis on the 10.16 cm and 7.62 cm schedule 40 and 80 data and is included here for completeness. Similar to Fig. 4-25, the correlation used for Fig. 4-28 cause some of the data to collapse. The difference is that in Fig. 4-28 the *A'* data for the 10.16 cm and 7.62 cm test sections collapse onto one another; whereas in Fig. 4-25, the *A'* data for the 5.08 cm and 7.62 cm test sections collapse onto one another. Also, in Fig. 4-28, the collapsed *A'* data for the 5.08 cm test sections is nominally three times greater than the collapsed 10.16 cm and

7.62 cm data. When this correlation is applied to the data of Pittard *et al.*[2] shown in Fig. 4-29, it causes the data from each pipe material to collapse fairly well. Although the 7.62 cm stainless steel data follows the same trend, its magnitude is slightly less than the rest of the collapsed data. The notable exception to the data collapse is the magnitude of the *A'* data from the 3.81 cm stainless steel test section, which is nominally three times less than the rest of the collapsed data. This correlation was developed previous to the acquisition of the data for the 5.08 cm test sections and while it yielded a good collapse of the original data, it is clear that it is not suitable for a large range of pipe diameters.

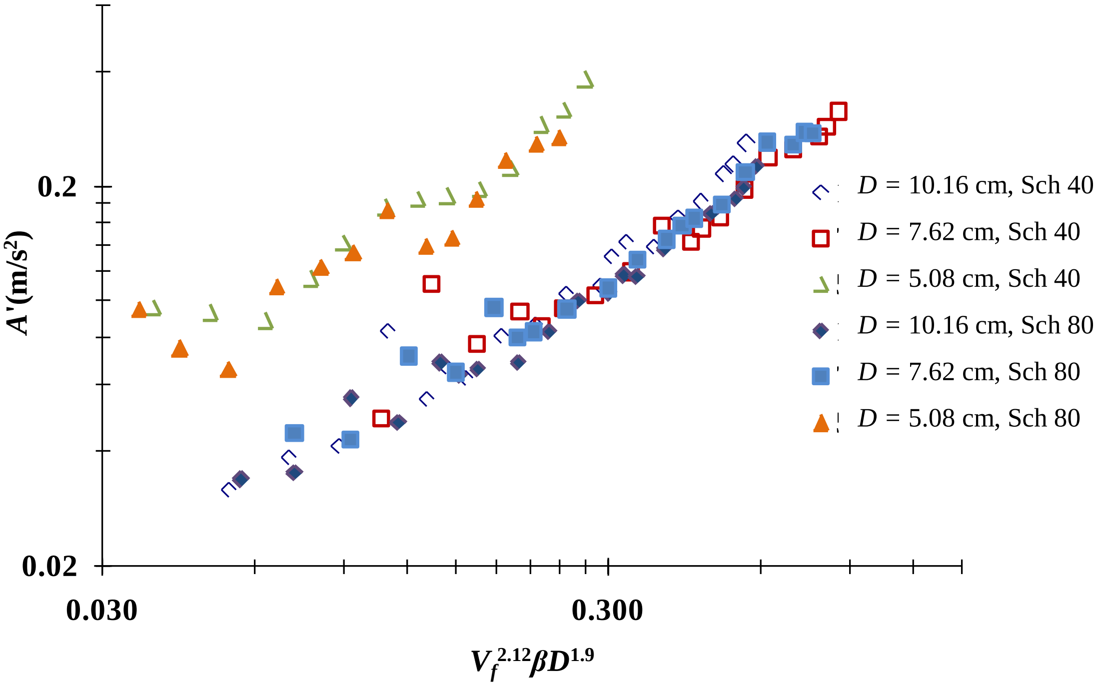

**Figure 4-28: *A'* vs. $V_f^{2.12}\beta D^{1.9}$ for each of the six unsupported test sections considered.**

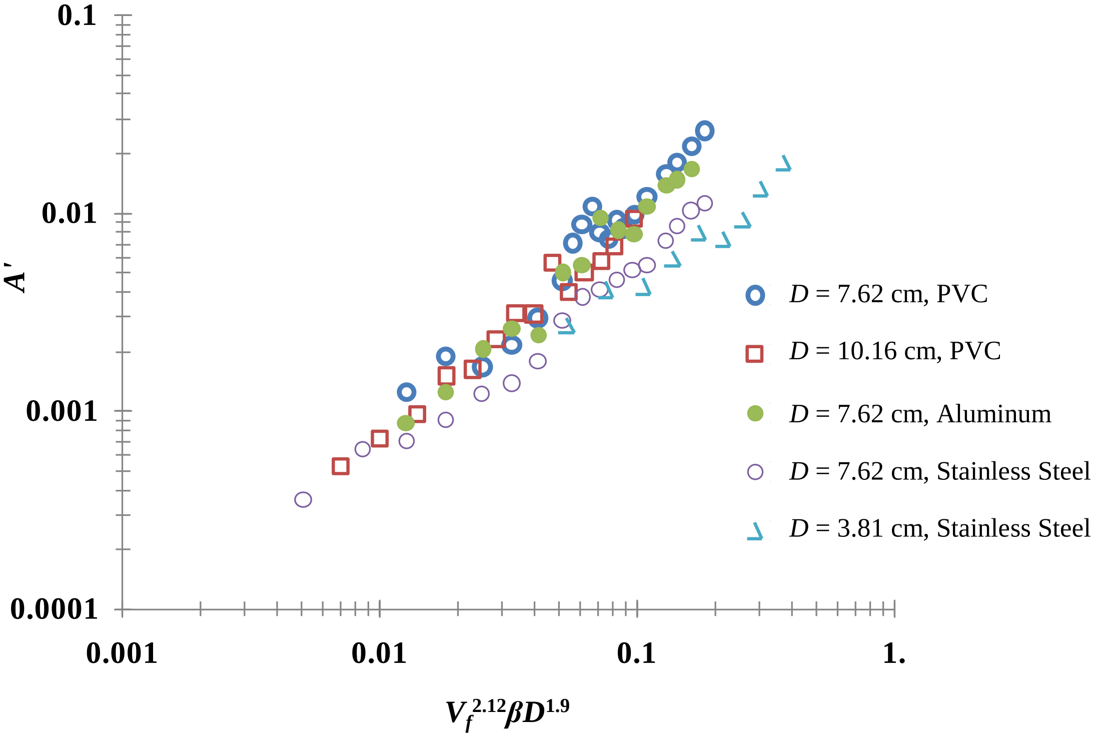

**Figure 4-29: $A'$ vs. $V_f^{2.12}\beta D^{1.9}$ for the data presented by Pittard *et al.* [2].**

It should be noted that holding one non-dimensional variable constant while changing the others was either very difficult or not possible for this research. For instance, it was not possible to vary pipe thickness while holding pipe diameter constant due to the standard pipe sizes that were used, this in turn would affect the other non-dimensional variables. What could be done for this research, however, was hold several dimensional parameters constant, such as pipe diameter and thickness, while changing flow rate.

To summarize, it was stated that the non-dimensional pipe wall acceleration, $A^*$, can be expressed as a function of the non-dimensional variables listed in Eqs. 4-6 to 4-11. Equation 4-14 is repeated here for convenience:

$$A^{*} = f(Re, t^{*}, L^{*}, \rho^{*}, E^{*}, \omega^{*})$$

Re-dimensionalizing $A^{*}$ gives:

$$A^{'} = \frac{V_f^2}{t} f(Re, t^{*}, L^{*}, \rho^{*}, E^{*}, \omega^{*}) \tag{4-15}$$

It was found that the non-dimensionalized pipe wall vibration, $A^{*}$, was a very weak function of $Re$, $t^{*}$, $E^{*}$, and $\omega^{*}$, showing good agreement with the numerical results of Shurtz [24]. Although experimental results varied greatly from the numerical results, it was found that $A^{*}$ had the strongest functional dependence on $\rho^{*}$. The variation between the numerical and experimental results was most likely due to the ability to numerically change one non-dimensional parameter without changing the others, thereby eliminating confounding results. The functional relationship of these non-dimensional parameters was weakest for the longest clamping support cases and became slightly more important as the clamping length became short. To a first order, the scaling $A' \sim V_f^2/t^{*}\rho^{*}$ provides a good estimate of the rms of the pipe wall acceleration for long or unsupported pipe sections.

## 4.4 Baffle Plate Influence

### 4.4.1 Various Baffle Plate Sizes

As discussed in section 3.2 baffle plates were inserted at the test section entrance as turbulence inducers. Five plates were used, each with a different diameter and number of holes drilled into them. The diameters of the holes were 2.54 cm, 1.27 cm, 0.635 cm, 0.318 cm, and 0.159 cm, with the hole diameter being how each baffle plate is distinguished in this thesis. The plates were fabricated so that the through area of the holes was 35.48 cm$^2$, resulting in various numbers of holes in each plate (*e.g.* seven holes for the 2.54 cm plate, 28 holes for the 1.27 cm baffle plate, 112 holes for the 0.635 cm baffle plate, 448 holes for the 0.318 cm baffle plate, and 1793 holes for the 0.159 cm plate). The 10.16 cm schedule 40 test section was the only test section used for the baffle plate experiments.

Figure 4-30 illustrates the effects on *A'* due to each baffle plate at various flow velocities and at a streamwise distance of 0.305 m from the baffle plate. The data is plotted versus the ratio of the baffle plate thickness to hole diameter. The data from each baffle plate is contained in the vertical columns of data, with the largest baffle plate on the left ($t_{baffle}/D_{hole}$ = 0.25).

It can be seen in Fig. 4-30 that the 2.54 cm and 1.27 cm baffle plates ($t_{baffle}/D_{hole}$ = 0.25 and 0.5 respectively) result in the largest increases in the magnitude of *A'*; although for all baffle plates the pipe acceleration increases. The largest increases are caused by cavitation that occurs in the largest baffle plates which was accompanied by audible noise. Evidence of cavitation can be seen to occur in Fig. 4-29 between a flow speed of 3.07 m/s and 3.72 m/s with the 2.54 cm baffle plate. At this $V_f$ the magnitude of *A'* suddenly jumps. Although not as apparent, cavitation appears to occur between 3.07 m/s and 3.97 m/s in the 1.27 cm baffle plate. What is also evident is that as $t_{baffle}/D_{hole}$ increases, the magnitude of *A'* decreases; apparently due to an upward shift in the velocity at which cavitation occurs and a reduction in the size of turbulent eddies formed. This shift can be seen as the baffle plate hole size decreases, with cavitation setting up only at the highest velocities in the 0.635 cm baffle plate and not at all in the smallest baffle plates.

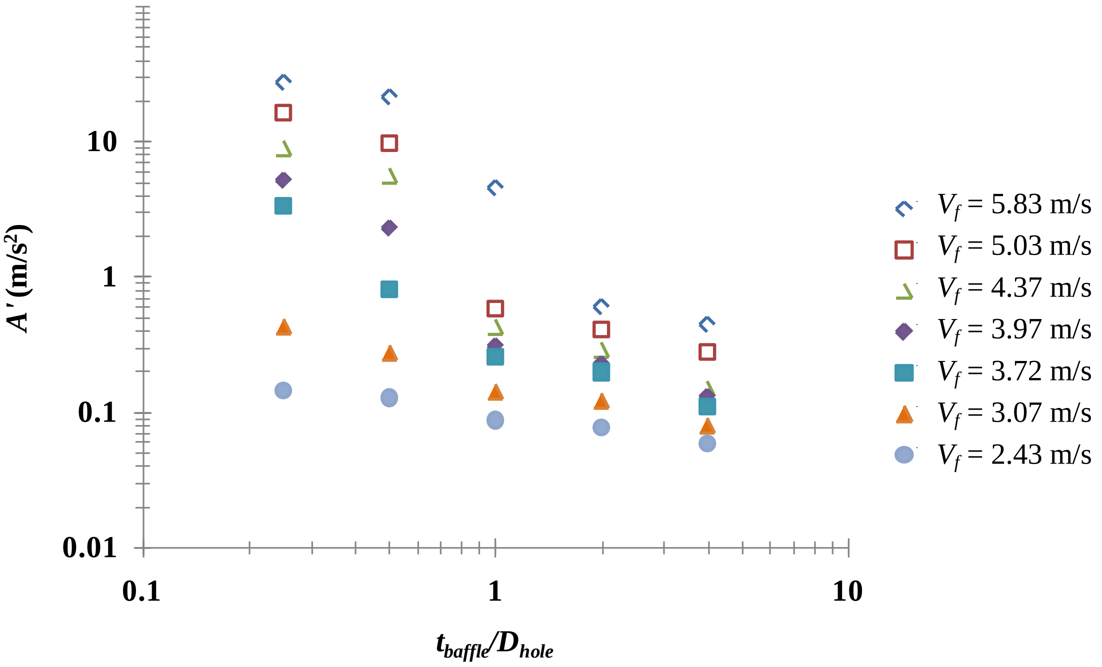

**Figure 4-30: *A′* as a function of $t_{baffle}/D_{hole}$ for various flow velocities in the 10.16 cm schedule 40 test section and each of the five baffle plates.**

Recall that Fig. 4-5 presents *A'* as a function of $V_f$ for seven locations along the length of the test section (*x/D*). For the no baffle plate scenario previously noted, in section 4.1.2.2, there is no systematic variation in *A'* with varying *x/D*. Figure 4-31 shows significantly different behavior for the 2.54 cm baffle plate scenario. The figure shows *A'* as a function of $V_f$ at various *x/D* locations along the test section. Also shown are data for the no baffle plate scenario. As previously stated, cavitation is occurring at the baffle plate holes, for this plate, and its effect on *A'* propagates down the entire length of the test section. Cavitation appears to be initiated at a fluid speed of about 3 m/s causing *A'* to rise rapidly with increasing $V_f$. At a flow speed of nominally 4 m/s, the rate of increase in *A'* levels off and becomes similar at all *x/D*. The magnitude of *A'* decreases with increasing *x/D* and decreases towards the vibration levels of the no baffle plate scenario at large *x/D*. A power law curve fit ($A' \sim V_f^m$) to the data above a flow speed of 4 m/s results in values of the power, *m*, ranging from 4.12 to 3.36 for the various *x/D* positions and is included in Table 4-4. At *x/D* = 3 and a flow speed of nominally 5.5 m/s, *A'* is observed to be about 300 times greater than for the no baffle plate case and at *x/D* = 57 (end of the test section), *A'* is nominally 20 times greater.

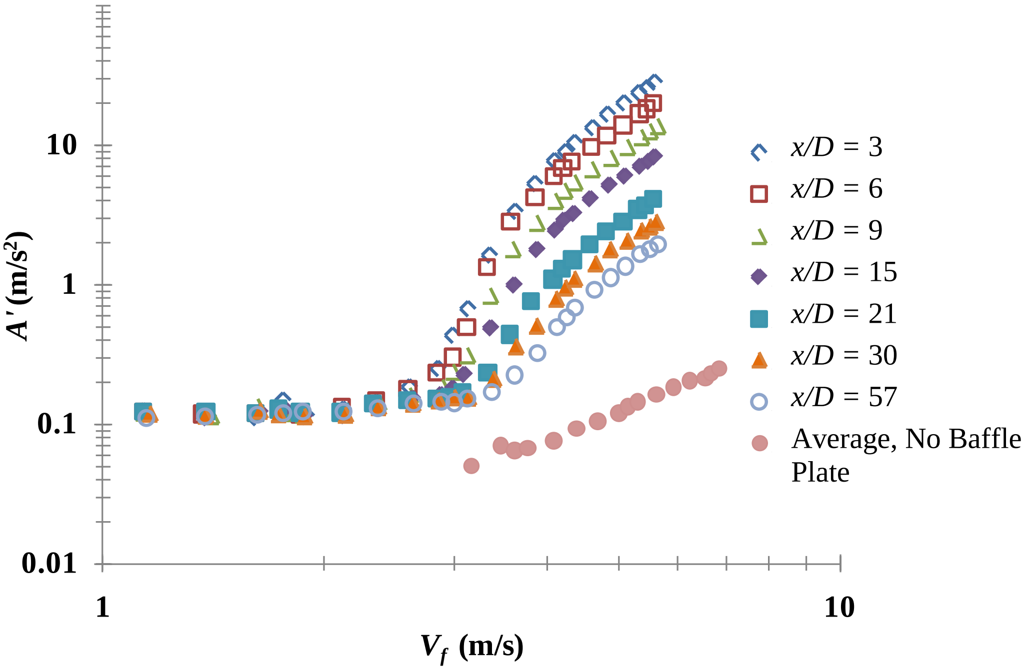

**Figure 4-31: *A'* vs. $V_f$ at seven *x/D* locations along the test section length with the 2.54 cm baffle plate. *A'* for the test section with no baffle plate has been included for reference.**

Figures 4-32 and 4-33 show *A'* as a function of $V_f$ for the 0.635 cm baffle plate ($t_{baffle}/D_{hole}$=1.0) and 0.159 cm baffle plate ($t_{baffle}/D_{hole}$=4.0), respectively. In Fig. 4-32, cavitation appears to be initiating only at the highest flow speed. Further, the magnitude of *A'* is significantly lower than what was shown for the 2.54 cm baffle plate data in Fig. 4-33. At a flow speed of nominally 5.5 m/s, *A'* is only about 10 times greater than for the no baffle plate case at $x/D$ = 3. A power law fit of the data with the exponents included in Table 4-4, shows that as $x/D$ increases the value of *m* approaches the no baffle plate case. This becomes even more apparent for the 0.159 cm baffle plate (Fig. 4-32). Here the magnitude of *A'* at $x/D$ = 3 is only about two times greater than for the no baffle plate case. The value of *m* also changes very little with $x/D$, with an average value of 2.04. These values are also included in Table 4-4. There appears to be little systematic variation in the value of *m* with $x/D$ for the 0.159 cm baffle plate scenario. However, for the 0.635 cm baffle plate scenario, the value of *m* decreases with increasing $x/D$. The values of *m* appear exhibit the same behavior for the 2.54 cm baffle plate except at the end of the test section, where the values of *m* begin to increase again. Comparing the values of *m* for the three baffle plate scenarios presented in Table 4-4 the general trend is that *m* increases with increasing baffle plate hole diameter.

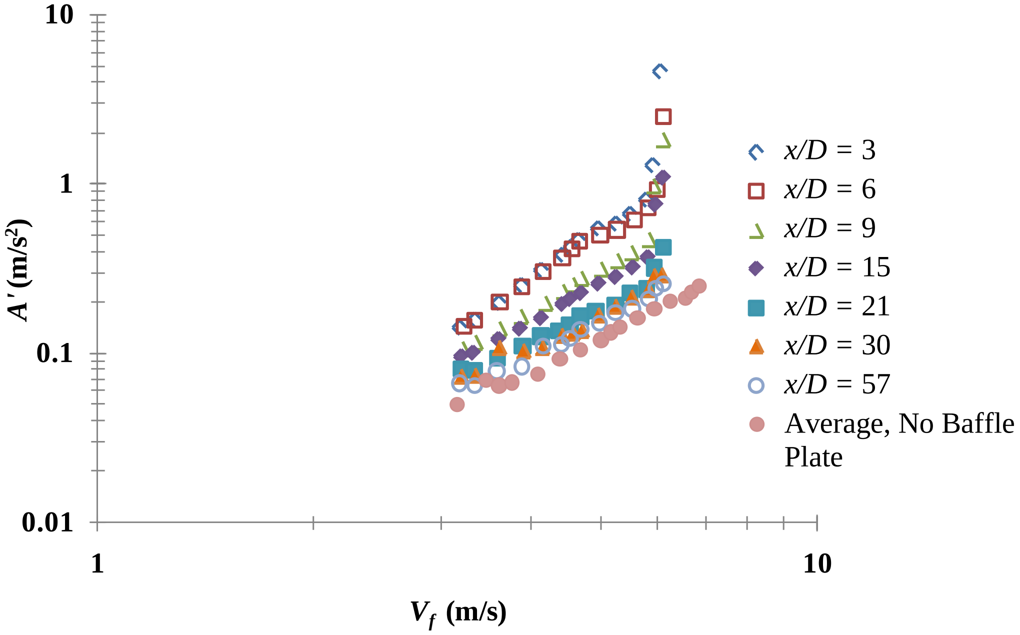

**Figure 4-32:** ***A′*** **vs.** ***$V_f$*** **at seven** ***x/D*** **locations along the test section length with the 0.635 cm baffle plate.** ***A′*** **for the test section with no baffle plate has been included for reference.**

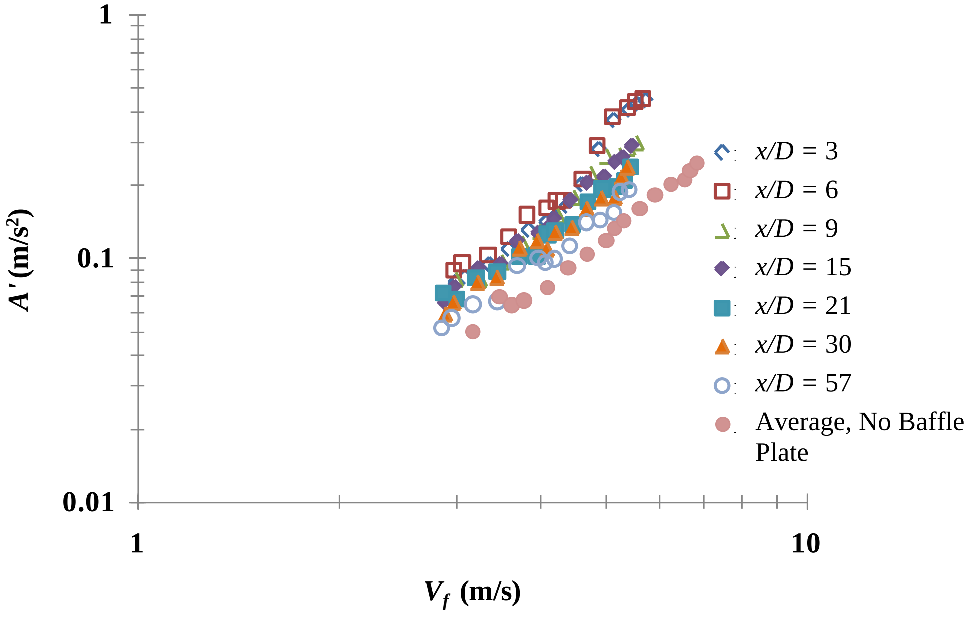

**Figure 4-33: A' vs. Vf at seven x/D locations along the test section length with the 0.159 cm baffle plate. A' for the test section with no baffle plate has been included for comparison.**

**Table 4-4: The value of *m* from a power law fit of the 2.54 cm, 0.635 cm, and 0.159 cm baffle plate data with *x/D*.**

| | Baffle Plate Hole Size | | | |
|---|---|---|---|---|
| ***x/D*** | **2.54 cm** | **0.635 cm** | **0.159 cm** | **No Plate** |
| **3** | 4.12 | 2.93 | 2.02 | 2.03 |
| **6** | 3.78 | 2.75 | 1.92 | |
| **9** | 3.54 | 2.45 | 2.29 | |
| **15** | 3.36 | 2.28 | 2.19 | |
| **21** | 3.70 | 2.03 | 1.89 | |
| **30** | 3.47 | 1.95 | 2.00 | |
| **57** | 3.85 | 2.09 | 1.98 | |
| **Average** | 3.69 | 2.35 | 2.04 | |

Figure 4-34 shows $A'$ as a function of $V_f$ for all five baffle plates at $x/D = 3$. As expected, $A'$ is greatest for the largest diameter baffle plate holes at all $V_f$. When cavitation is not occurring and as the baffle plate hole size decreases, the dependence of $A'$ on $V_f$ appears to approach the no baffle plate scenario. The primary difference is that there is an upward offset in the magnitude of $A'$ that corresponds to the size of the baffle plate holes. Cavitation exists for the 2.54 cm baffle plate above about 3 m/s and it exists for the 1.27 cm baffle plate above a speed of nominally 3.5 m/s. For the 0.635 cm baffle plate, cavitation appears to exist above 6.7 m/s.

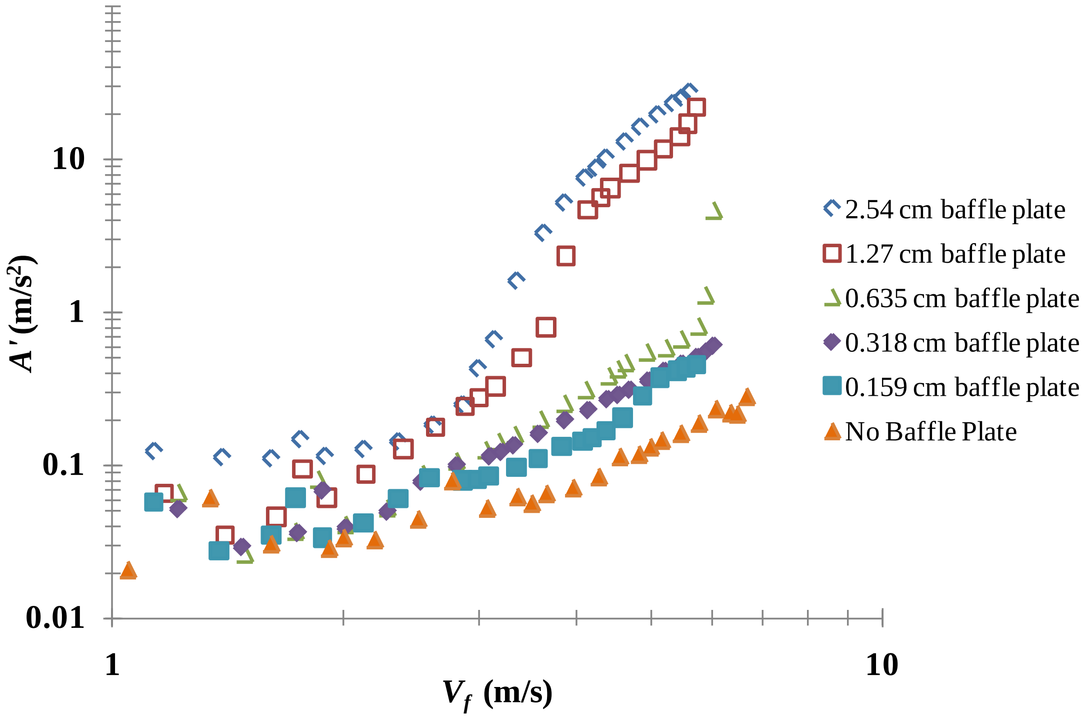

**Figure 4-34: *A'* vs. $V_f$ at *x/D* = 3 for all five baffle plates. *A'* for the no baffle plate case is included for comparison.**

Figure 4-35 presents *A'* as a function of $V_f$ at *x/D* = 30. At this streamwise position, the magnitude of *A'* has dropped nominally by a factor of 10 for all baffle plates. For the scenarios where cavitation does not exist, the magnitude of *A'* is approaching the no baffle plate case results. This indicates that *A'* decays with increasing distance from the baffle plate. Recall from equation 3-1 and section 3.1 that for turbulent pipe flow to be considered fully developed $L_e/D \sim 44$ ($\frac{L_e}{D} \approx 4.4Re^{\frac{1}{6}}$). At *x/D* = 30, this streamwise position is nearly far enough away from the baffle plates for the flow to be considered fully developed again. The implication is that sufficiently far away from a turbulence source that is not inducing cavitation, the magnitude of *A'* approaches a condition representative of the baseline fully-developed turbulent pipe flow.

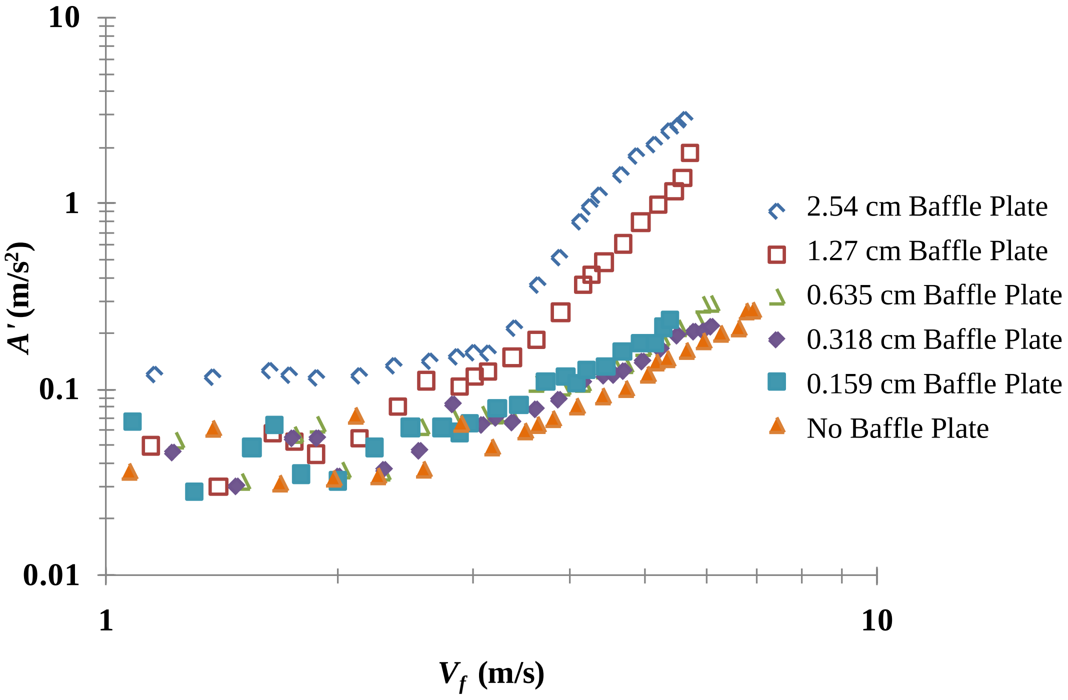

**Figure 4-35: *A'* vs. $V_f$ at *x/D* = 30 for all five baffle plates. *A'* for the no baffle plate case is included for comparison.**

Figure 4-36 illustrates how the magnitude of *A'* decays with *x/D* for each baffle plate case at a constant flow speed of 3.61 m/s. As expected, the magnitude of *A'* for the no baffle plate case is nominally flat along the test section length. Although the flow velocity is relatively low, cavitation is occurring with the 2.54 cm and 1.27 cm baffle plates. For these cases, the decay in the magnitude of *A'* appears to be steeper than for the three other scenarios. The test section may not be long enough for *A'* to return to the baseline levels characteristic of the no baffle plate case. The magnitude of *A'* for the

0.318 cm and 0.159 cm baffle plates has decayed to the no baffle plate values by nominally *x/D* = 9. For the 0.635 cm baffle plate *A'* decays to the baseline value at *x/D* = 15.

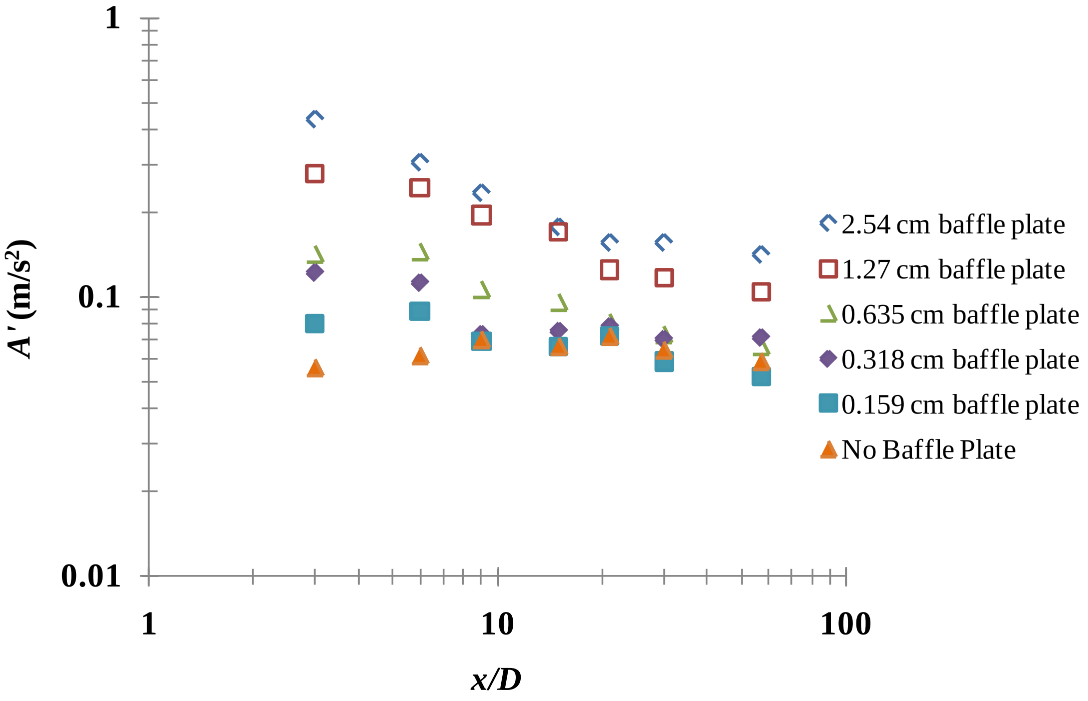

**Figure 4-36: The decay of *A'* with *x/D* for each baffle plate case at a flow speed of 3.61 m/s.**

As the flow speed increases to 6.84 m/s, as illustrated by the results of Figure 4-36, it is evident that the decay in the magnitude of *A'* is pushed further downstream. In the cases where cavitation is occurring, the magnitude of *A'* doesn't begin to level off until above *x/D* = 30. The magnitude of *A'* with the 0.318 cm and 0.159 cm baffle plate has decayed to the no baffle plate levels by *x/D* = 15, and by *x/D* = 30 for the 0.635 cm baffle plate.

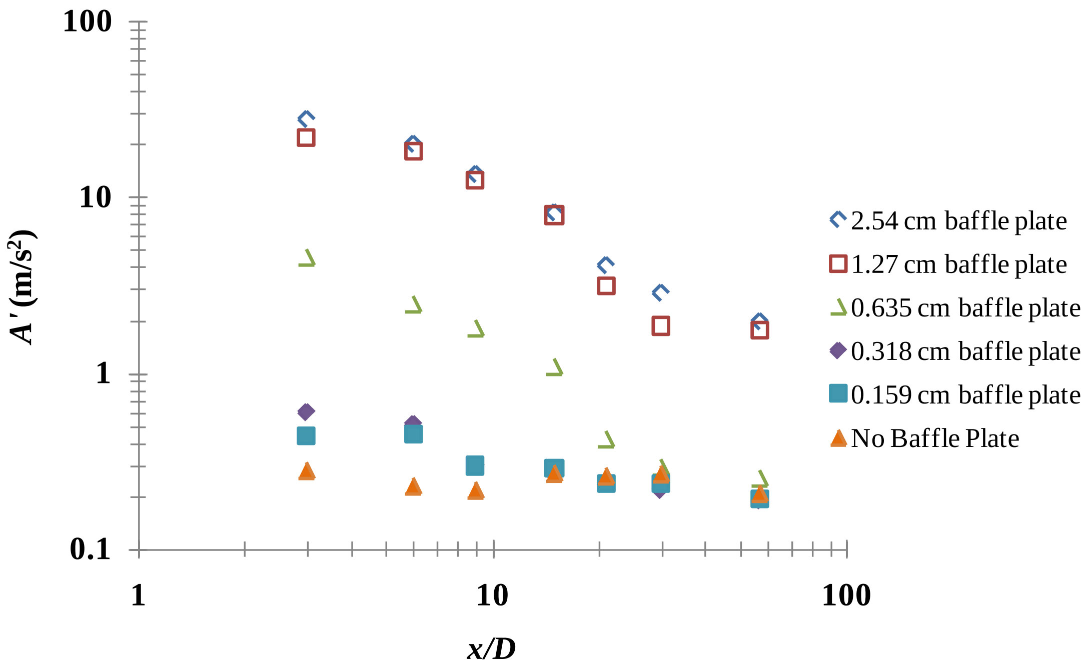

**Figure 4-37: The decay of *A'* with *x/D* for each baffle plate case at a flow speed of 6.84 m/s.**

To summarize, cavitation was observed occur with the 2.54 cm and 1.27 cm baffle plates at flow speeds as low as nominally 3 m/s. Upon initiation of cavitation, the magnitude of *A'* near the baffle plate increased by up to 300 times of the baseline no baffle plate case. As the distance from the baffle plates increased, the level of *A'* for each baffle plate case decreases toward the baseline. It was observed that the flow speed at which cavitation is initiated increases as the baffle plate hole size decreases. Also, with the baffle plates where cavitation does not occur, *A'* decays to the baseline at an *x/D* location that increases with $V_f$.

### 4.4.2 Accelerometer Spectra for Baffle Plate Scenarios

Figure 4-38 shows $\tilde{A}$ for accelerometers placed at increasing distance ($x$ = 0.305, 3.05, and 5.79 m) from the 2.54 cm baffle plate at a flow speed of 2.12 m/s. At this flow speed, cavitation is not occurring. Near the baffle plate ($x$ = 0.305 m), $\tilde{A}$ is relatively flat across the frequency spectrum. Further downstream ($x$ = 3.05 m), $\tilde{A}$ begins to decay, at $f \approx 400$ Hz, although the decay is notably steeper than the $f^{-5/3}$ decay. This steeper decay is similar to that observed at low flow speeds in the test section without a baffle plate (Fig. 4-9). With the baffle plate, however, this decay begins at a much higher frequency (nominally 400 Hz). At larger streamwise distances ($x$ = 5.79 m) the decay begins at even lower $f$ (~300 Hz). Figure 4-39 illustrates $\tilde{A}$ vs. $f$ at three $x$ locations downstream of the 2.54 cm baffle plate at a flow speed of 5.63 m/s. As the flow speed increases to 5.63 m/s (into the cavitating regime) an increase in $\tilde{A}$ is apparent at about 2.50 kHz and at $x$ = 0.305 m. This localized increase in $\tilde{A}$ appears to shift to lower frequencies at increasing $x$. It is also apparent that the decay is much steeper than $f^{-5/3}$ for all scenarios.

Recall from section 2.2.2 Qing *et al.* found that a supercavitation bubble was forming downstream of an orifice plate. The PSD of their data showed a similar local rise in $\tilde{A}$ near the orifice (Fig. 2-2), and the energy content was concentrated below 400 Hz. It was concluded that the orifice disturbance was localized to the vicinity of the orifice because less energy was concentrated below certain frequencies at increasing downstream position. It appears that similar behavior exists in Fig. 4-38 and that the cavitation disturbance is localized to near the baffle plate, however, $\tilde{A}$ over the entire frequency range is not available due to the limit in the sampling frequency for the present data.

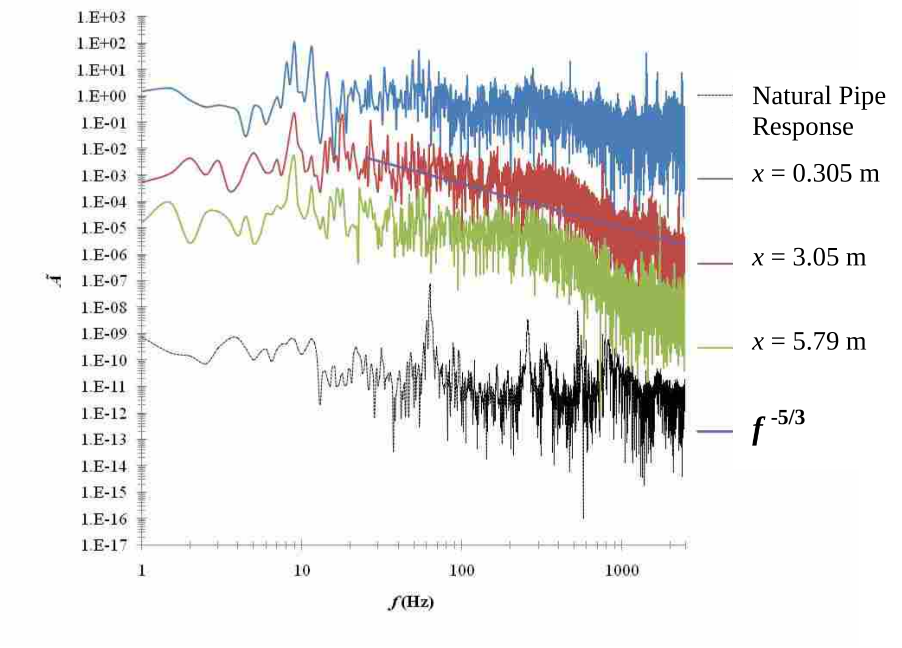

**Figure 4-38:** ***Ã*** **at three** ***x*** **locations downstream of the 2.54 cm baffle plate at a flow speed of 2.12 m/s. The sets of** ***Ã*** **data have been multiplied by 1000 (*****x*** **= 0.305 m), 1 (*****x*** **= 3.05 m), and 0.01 (*****x*** **= 5.79 m), respectively to differentiate the data sets.**

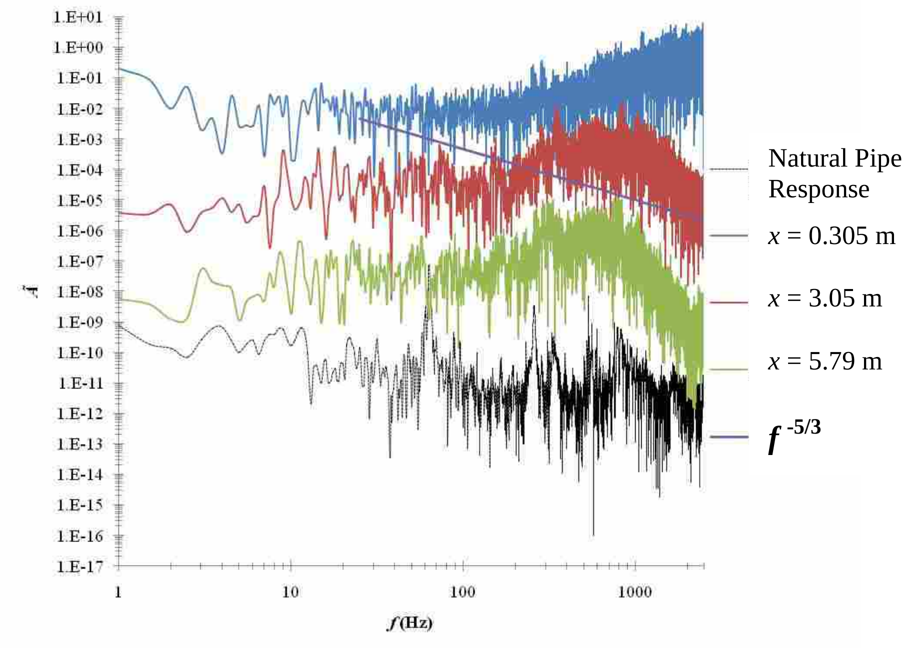

**Figure 4-39:** ***Ã*** **at three** ***x*** **locations downstream of the 2.54 cm baffle plate at a flow speed of 5.63 m/s. The sets of** ***Ã*** **data have been multiplied by 1000 (*****x*** **= 0.305 m), 1 (*****x*** **= 3.05 m), and 0.001 (*****x*** **= 5.79 m), respectively to differentiate the data sets.**

As previously noted, as the baffle plate hole size decreases, the magnitude of *A'* appears very similar to the no baffle plate case. This similarity is also present in $\tilde{A}$. Figure 4-40 shows $\tilde{A}$ at three distances from the 0.159 cm baffle plate ($x$ = 0.305, 3.05, and 5.79 m) at an average flow speed of 2.12 m/s. The roll-off in $\tilde{A}$ is steeper than $f^{-5/3}$ similar to the no baffle plate data illustrated in Fig. 4-9 for low flow speeds. There is a slight rise in $\tilde{A}$ at about 2.50 kHz near the baffle plate ($x$ = 0.305 m), but this vanishes at increasing $x$. Figure 4-41 shows $\tilde{A}$ at a flow speed of 5.63 m/s and at the same three $x$ locations. Comparing this behavior to what is shown in Fig. 4-10, demonstrates that $\tilde{A}$ approaches an $f^{-5/3}$ decay at increasing $x/D$. Near the baffle plate ($x$ = 0.305 m) there is a rise in $\tilde{A}$ at about 40 Hz that is not present at the other locations, again seeming to indicate that the disturbance induced by the baffle plate is localized to the baffle plate's vicinity. This local rise is similar to what is observed in Fig. 4-39 at the same location. Although cavitation is not occurring in the 0.159 cm baffle plate, turbulent jets exist and there is similar behavior in $\tilde{A}$ to the 2.54 cm baffle plate in the vicinity of the plate. As the distance from the 0.159 cm baffle plate increases, however, the behavior of $\tilde{A}$ becomes almost indistinguishable from the no baffle plate case.

Figures 4-42 and 4-43 compare $\tilde{A}$ at $x$ = 0.305 m and 5.79 m downstream from all five baffle plates, at a flow speed of 5.63 m/s. Each $\tilde{A}$ has been multiplied by a factor as listed in the caption so they are discernable from each other. At $x$ = 0.305 m from the baffle plates, there is a rise in $\tilde{A}$ at about 2.50 kHz, presumably as a local increase that will vanish at higher frequencies. Although cavitation is occurring only with the 2.54 cm and 1.27 cm baffle plates, the increase in $\tilde{A}$ occurs for each baffle plate and indicates that there is a turbulent disturbance in the vicinity of each baffle plate due to the turbulent jets. The data of Fig. 4-43, at $x$ = 5.79 m from the baffle plate, it shows that for decreasing baffle plate hole size, the local rise that was noted in Fig. 4-39 either shifts to higher frequencies or reduces in amplitude, and the decay in $\tilde{A}$ begins to approach the $f^{-5/3}$ behavior. It is also interesting to note in Fig. 4-42, at $x$ = 0.305 m from the baffle plates, although cavitation disappears as the baffle plate hole diameters decrease, there appears to be little difference in $\tilde{A}$ due to turbulent jets near the baffle plate, which was also observed by Qing and is mentioned in section 2.2.2.

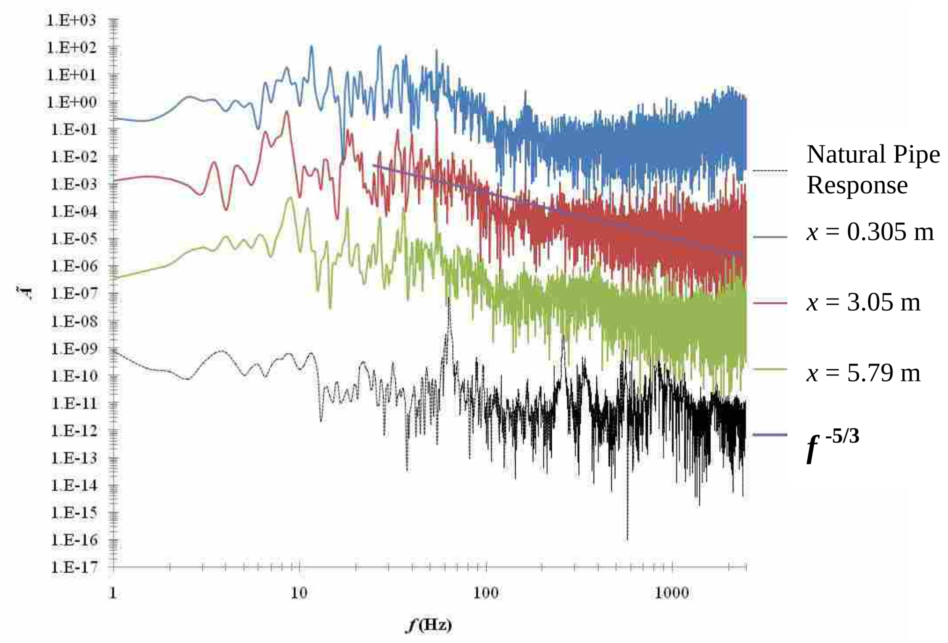

**Figure 4-40: $\tilde{A}$ at a three $x$ locations downstream of the 0.159 cm baffle plate at a flow speed of 2.12 m/s. Sets of $\tilde{A}$ data have been multiplied by $1x10^3$ ($x$ = 0.305 m), 1 ($x$ = 3.05 m), and $1x10^{-3}$ ($x$ = 5.79 m), respectively to differentiate the data sets.**

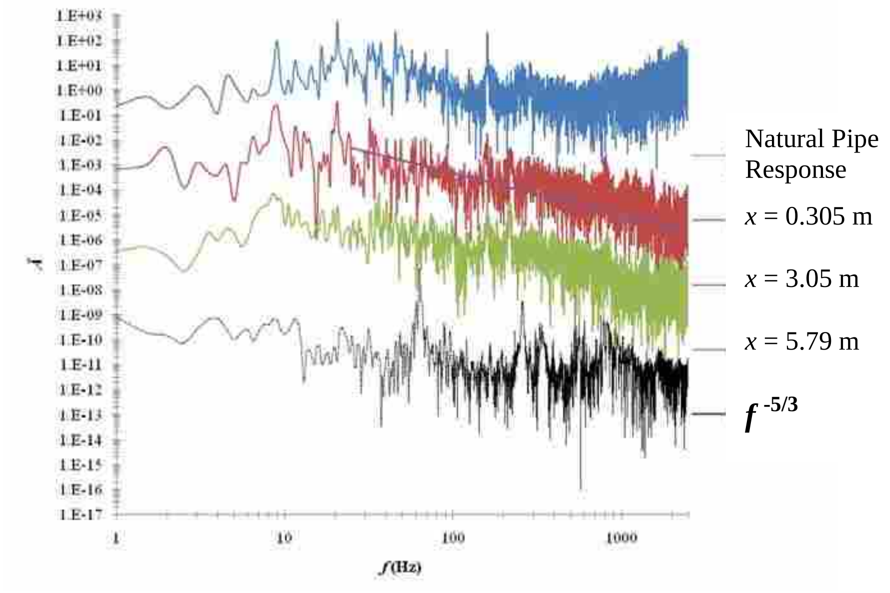

**Figure 4-41:** $\tilde{A}$ **at a three** $x$ **locations downstream of the 0.159 cm baffle plate at a flow speed of 5.63 m/s. sets of** $\tilde{A}$ **data have been multiplied by** $1\text{x}10^4$ **(**$x$ **= 0.305 m), 1 (**$x$ **= 3.05 m), and** $1\text{x}10^{-3}$ **(**$x$ **= 5.79 m), respectively to differentiate the data sets.**

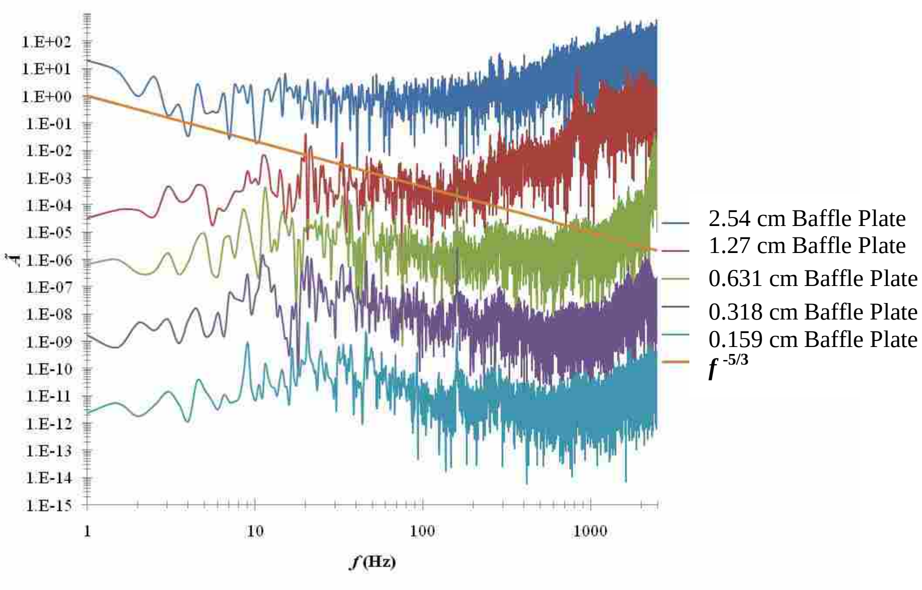

**Figure 4-42:** $\tilde{A}$ **at 0.305 m downstream of each of the five baffle plates and at a flow speed of 5.63 m/s. Sets of** $\tilde{A}$ **data have been multiplied by** $1\text{x}10^5$ **(2.54 cm baffle), 1** $\text{x}10^3$ **(1.27 cm baffle), 1 (0.635 cm baffle),** $1\text{x}10^{-4}$ **(0.318 cm baffle), and** $1\text{x}10^{-7}$ **(0.159 cm baffle), respectively to differentiate the data sets.**

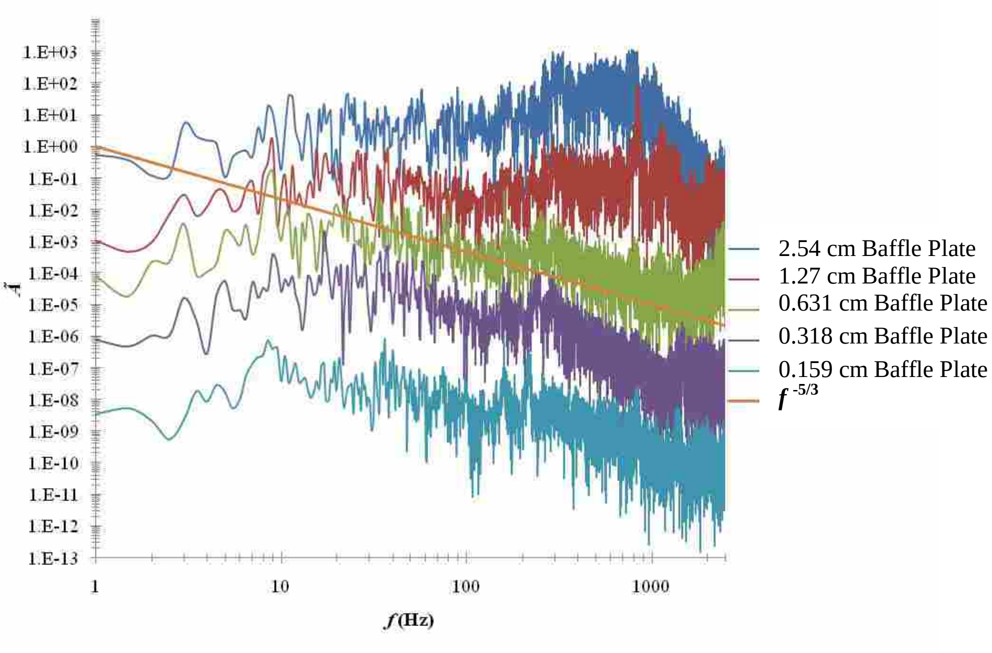

**Figure 4-43: $\tilde{A}$ at 5.79 m downstream of each of the five baffle plates and at a flow speed of 5.63 m/s. Sets of $\tilde{A}$ data have been multiplied by $1\text{x}10^{5}$ (2.54 cm baffle), 1 $\text{x}10^{3}$ (1.27 cm baffle), 1 (0.635 cm baffle), $1\text{x}10^{-2}$ (0.318 cm baffle), and $1\text{x}10^{-5}$ (0.159 cm baffle), respectively to differentiate the data sets.**

In summary far away from the baffle plates and at low flow speeds where cavitation is not occurring, $\tilde{A}$ decays steeper than $f^{-5/3}$ and is influenced more by the natural pipe response. As the flow speed increases far away from the non-cavitating baffle plates, $\tilde{A}$ decays nominally as $f^{-5/3}$ and is influenced very little by the natural pipe response. Near the baffle plates, independent of cavitation and baffle plate hole size, an increase in $\tilde{A}$ exists and indicates a turbulent or cavitation disturbance near the baffle plate. Far away from the baffle plates where cavitation is occurring, a large local rise and steep decay in $\tilde{A}$ develops that either decreases in amplitude or shifts to higher frequencies as baffle plate hole size decreases.

# 5 Conclusion

This thesis presented the results of an experimental investigation to characterize pipe vibrations induced by turbulent pipe flow. Experiments were conducted using a water flow loop to address three general phenomena related to pipe vibration: 1) How the pipe vibration depends on the average flow speed, pipe diameter, and pipe thickness for an unsupported pipe. 2) How the behavior changes if the pipe is supported at various clamping lengths. 3) How turbulence generation caused by holed baffle plates influence the pipe response.

## 5.1 Vibration Dependence on Fluid Speed and Un-Supported Pipe Parameters

When comparing a power law fit of the average of $P'$ along the pipe length to $V_f$, it was found that $P'$ scaled nearly as $V_f^2$, with the power from the experimental data varying less than 5% from an expected value of 2.0. It was determined that $A'$ for the unsupported pipe also scaled nearly quadratically with $V_f$, with an average power over all the test sections of 2.06. Also, it was shown, doing a similar analysis, that $V'$ scaled as $V_f^{1.62}$, with the power for the $V'$ relation being about 80% of the $A'$ value. Put differently, $P'$ and $A'$ are proportional to the dynamic pressure in the pipe; and $V'$ is proportional to the dynamic pressure raised to the 0.80 power.

It was observed that the magnitude of *A'* also varies modestly with inner pipe diameter (*D*) and thickness (*t*). Specifically, *A'* was observed to increase as the ratio *D/t* increases. However, the dependence on *D/t* does not appear to be constant with flow rate, with *A'* becoming less dependent on *D/t* with increasing flow rate.

When computing the PSD of the accelerometer time series data, $\tilde{A}$ was found to be sensitive to the natural pipe response at low flow speeds, with local rises in $\tilde{A}$ corresponding to natural frequencies of the system. The decay of $\tilde{A}$ was also observed to decay much steeper than $f^{-5/3}$. This sensitivity to the natural pipe response was observed to vanish as high flow speeds as the frequency content of $\tilde{A}$ shifted to higher regimes. At high flow speeds, the pipe vibrations measured by the accelerometers appear to be due to the local turbulent fluctuations at the pipe wall, which decay as $f^{-5/3}$.

## 5.2 Vibration Dependence on Fluid Speed and Clamped Pipe Parameters

Varying the distance between the clamp supports appeared to affect *A'* only modestly. Specifically, *A'* was still observed to scale nearly as $V_f^2$ for most of the clamping distances, with the dependence of *A'* on $V_f$ increasing slightly with decreasing clamping length. However, when the clamping distance became very short, *A'* was observed to scale nearly as $V_f^3$, indicating a greater dependence of *A'* on $V_f$ with decreasing clamping length. This modest clamping length dependence was also observed to not be constant with flow rate.

Clamping length exhibited a greater influence on *V'*. It was observed that *V'* became less dependent on $V_f$ as clamping length decreased. Also, the magnitude of *V'* was observed to increase with increasing clamping length, whereas the magnitude of *A'* was observed to increase with decreasing clamping length.

## 5.3 Non-Dimensionalization of *A'*

When comparing the non-dimensionalized pipe wall acceleration ($A^*$) to the non-dimensional parameters *Re*, $t^*$, $L^*$, $E^*$, $\rho^*$, and $\omega^*$, it was found that $A^*$ was weakly dependent on all of them except $\rho^*$. This was in good agreement to a parallel numerical study performed by Shurtz [24]. This strong dependence on $\rho^*$ resulted in the scaling relationship, $A' \sim V_f^2/t^*\rho^*$. This scaling relationship is a first order estimate of the expected level of pipe vibration in a long or unsupported pipe.

Where the clamping support was long, $\tilde{A}$ was observed to be very similar to the unsupported case. However, $\tilde{A}$ was observed to be more sensitive to the natural pipe response when clamping was short, even at high fluid speeds.

## 5.4 Baffle Plate Influence on Pipe Response

It was found that placing baffle plates into the flow would induce turbulence downstream of the baffle plate. For large baffle plate hole size cavitation existed at high fluid speeds. Cavitation would cause the magnitude of *A'* to increase by up to 300 times. As the baffle plate hole size decreased, it was observed that the fluid speed at which cavitation would initiate would increase to greater values. Cavitation was not prevalent at all with baffle plate hole sizes smaller than 0.635 cm. Further, it was observed that as the baffle plate hole size decreased, *A'* would approach magnitudes shown with the no baffle plate baseline. *A'* was also observed to decay to baseline levels as the distance from a non-cavitating baffle plate increased.

Away from a non-cavitating baffle plate, the decay of $\tilde{A}$ approaches the expected $f^{-5/3}$ power law relation. Cavitation was observed to cause a local rise in $\tilde{A}$ that either shifts to higher frequencies or decreases in magnitude as the baffle plate hole size decreases, with cavitation ceasing completely with the small diameter baffle plates. Near each baffle plate, a rise in $\tilde{A}$, regardless of cavitation, indicates that a turbulent disturbance exists at the plates.

## 5.5 Recommendations

This thesis presented the results of an experimental study with the purpose of characterizing turbulence induced pipe wall vibrations. Although these results were compared to the results of other researchers, namely Pittard *et al.*, this thesis examined only one pipe material (PVC), one fluid (water), and two standard thicknesses of pipe (schedules 40 and 80). Future studies should employ more pipe materials (such as aluminum or stainless steel), a fluid with a different density (such as air), and an extended range of pipe schedules (such as schedules 10 and 160).

Also, great care should be taken when drilling pressure taps. It was noted that about 72 % of the uncertainty in the pressure measurements were due to burr effects. These effects made more than general comparisons of wall pressure fluctuations between tap locations and test sections suspect. This uncertainty also obscured comparisons between the pressure measurements and acceleration measurements.

Finally, it is recognized that conducting the several experiments necessary to characterize the fluid induced pipe vibrations are limited because of the limited number of elements that can varied and due to cost both in time and money. Therefore, the experimental results presented in this thesis can be used as validation for numerical studies similar to the study completed by Shurtz [24]. The advantage of a numerical study is that it gives the ability to change the fluid and pipe parameters with relative ease

## 5.6 Publications

A publication based on part of the work presented in this thesis has been presented at the 2009 ASME fluids engineering summer meeting (FEDSM2009). This work presents a comparison between the 10.16 cm and 7.62 cm test sections and the results presented by Pittard *et al.* [2]. Correlations that collapsed the data from both sources were formulated. Subsequent journal publications of the results will be pursued.

# 6 References

1. Awawdeh, A., Bukkapatnam, S.T.S., Kumara, S.R.T., *et al.*, "Wireless sensing of Flow-Induced Vibrations for Pipeline Integrity Monitoring," *IEEE SAM 06*, Boston, July 2006.

2. Pittard, M.T., Evans, R. P., Maynes, D., Blotter, J., "Experimental and Numerical Investigation of Turbulent Flow Induced Pipe Vibration in Fully Developed Flow," *Review of Scientific Instruments*, Vol. 75, Number 7, July 2004, pp 2393-2401.

3. National Transportation Safety Board, "Pipeline Accident Brief," NTSB/PAB-01/02, Pipeline accident number: DCA-00-MP-004, May 3, 2001.

4. Figliola, R.S., Beasley, D.E., *Theory and Design for Mechanical Measurements, Second Edition*, John Wiley and Sons, Inc., 1995.

5. Evans, R.P., Blotter, J.D., Stephens, A.G., "Flow Rate Measurements Using Flow-Induced Pipe Vibration," *Transactions of the ASME*, Vol. 126, March 2004, pp 280-285.

6. Kim, Y.K., Kim, Y.H., "A Three Accelerometer Method for the Measurement of Flow Rate in Pipe," *Journal of the Acoustical Society of America*, Vol. 100, Number 2, Part 1, August 1996, pp 717-726.

7. Genscape Inc. Website: http://www.genscape.com/pages.php?uid=2

8. Blevins, R.D., "Flow-Induced Vibration in Nuclear Reactors; a Review," *Progress in Nuclear Energy*, Vol. 4, 1979, pp 25-49.

9. Paidoussis, M.P., "Fluidelastic Vibratio of Cylinder Arrays in Axial and Cross Flow: State of the Art," *Journal of Sound and Vibration,* Vol. 76, Number 3, 1981, pp 329-360.

10. Reavis, J.R., "Vibration Correlation for Maximum Fuel-Element Displacement in Parallel Turbulent Flow," *Nuclear Science and Engineering*, Vol. 38, 1969, pp 63-69.

11. Burgreen, D., Byrnes, J.J., Benforado, D.M., “Vibration of Rods Induced by Water in Parallel Flow,” *Transactions of the ASME 80,* 1958, pp 991-1003.

12. Bernard, P.S., Wallace, J.M., *Turbulent Flow Analysis, Measurement and Prediction,* John Wiley and Sons, Inc., 2002.

13. Saddoughi, S.G., “Local Isotropy in Complex Turbulent Boundary Layers at High Reynolds Number,” *Journal of Fluid Mechanics,* Vol. 348, 1997, pp 201-245.

14. Lysak, P.D., “Modeling the Wall Pressure Spectrum in Turbulent Pipe Flows,” *Transactions of the ASME,* Vol. 128, March 2006, pp 216-222.

15. “Kolmogorov Cascade,” *Encyclopedia of Non-Linear Sciences*.

16. Caillaud, S., Gibert, R., Moussou, P., Cohen, J., Millet, F., “Effects on Pipe Vibrations of Cavitation in an Orifice and in Globe-Style Valves,” *Proceedings of Pressure Vessels and Piping Conference,* July, 2006.

17. Qing, M., Jinghui, Z., Yushan, L., Haijun, W., Quan, D., “Experimental Studies of Orifice-Induced Wall Pressure Fluctuations and Pipe Vibration,” *International Journal of Pressure Vessels and Piping,* Vol. 83, 2006, pp 505-511.

18. Qing, M., Jinghui, Z., “Orifice-Induced Wall Pressure Fluctuations and Pipe Vibrations: Theory and Modeling of Fluid Excitation,” *Flow Turbulence and Combustion,* Vol. 79, 2007, pp 25-40.

19. Moussou, P., “An Attempt to Scale the Vibrations of Water Pipes,” *Transactions of the ASME,* Vol. 128, November 2006, pp 670-676.

20. Maynes, D., “Turbulence Induced Vibration in Straight Pipe Flow Considerations.”

21. Munson, B.R., Young, D.F., Okiishi, T.H., *Fundamentals of Fluid Mechanics, Fifth Edition,* John Wiley and Sons, Inc., 2006.

22. Tropea, C., Yarin, A.L., Foss, F.F., *Springer Handbook of Experimental Fluid Mechanics,* 2007, pp 180-185.

23. Brown, J.W., Churchill, R.V., *Fourier Series and Boundary Value Problems, Sixth Edition,* McGraw Hill, 2001.

24. Shurtz, T.P., *Analysis of Induced Vibrations in Fully-Developed Turbulent Pipe Flow Using a Coupled LES and FEA Approach,* Brigham Young University, Provo, UT, USA, Master’s Thesis, 2009.

# Appendix A: MatLab rms Code

The following is the MatLab code was used to calculate the rms values of the time series data that was collected.

```
clear; close;
clear filename
n = 22; % number of files
%

%Filename Convention is: D:\Pipe diameter and schedule\Diameter of
%developing region if different than 4 inch\Which baffle plate was
inserted
%and the units acceleration is measured in\Which LabView VI was
used\Which
%experiments were run and support location\Accelerometer and Pressure
%transducer location\Pressure transducer x/D
%location\PipeDiameter_PipeSchedule_PumpSpeed_0001.txt
intro = 'D:\2 inch Schedule 40\2 inch Developing Region\No Baffle Plate
Accel in Gs\New VI\ApPp_xod_no sup\Same Location Opposite Sides
P1A1_West_P2A2_East\PA_18ft\2in40_';
%
%
samples = 50000;
time = 1/5000;

%Structures were used for ease of manipulating the data.


for i = 1:n
    istring = int2str((i-1)*2);
    if 2*(i-1) < 10
        filename(i).name = strcat(intro,'0',istring,'Hz_0001.txt');
    else
        filename(i).name = strcat(intro,istring,'Hz_0001.txt');
    end
    Data = load(filename(i).name);

% Picks the corresponding data from the following columns.
    filename(i).tyme=Data(:,1);
    filename(i).ua1=Data(:,2);
    filename(i).ua2=Data(:,3);
```

```
    filename(i).v1=Data(:,4);
    filename(i).v2=Data(:,5);
    filename(i).disp1=Data(:,6);
    filename(i).disp2=Data(:,7);
    filename(i).flow=Data(:,8);
    filename(i).p1=Data(:,10);
    filename(i).p2=Data(:,11);
    filename(i).pdif=Data(:,12);
    filename(i).p1f=Data(:,13);
    filename(i).p2f=Data(:,14);
    filename(i).pdiff=Data(:,15);



%     Calculates the RMS values
        filename(i).ua1rms=sqrt(mean(filename(i).ua1.^2));
        filename(i).ua2rms=sqrt(mean(filename(i).ua2.^2));

        filename(i).vel1rms1000=sqrt(mean(filename(i).v1.^2))*1000;
        filename(i).vel2rms1000=sqrt(mean(filename(i).v2.^2))*1000;

        filename(i).disp1rms1000=sqrt(mean(filename(i).disp1.^2))*1000;
        filename(i).disp2rms1000=sqrt(mean(filename(i).disp2.^2))*1000;

        filename(i).flowrms = sqrt(mean(filename(i).flow.^2));

        filename(i).p1rms = sqrt(mean(filename(i).p1.^2));
        filename(i).p2rms = sqrt(mean(filename(i).p2.^2));
        filename(i).pdifrms = sqrt(mean(filename(i).pdif.^2))/sqrt(2);

        filename(i).p1frms = sqrt(mean(filename(i).p1f.^2));
        filename(i).p2frms = sqrt(mean(filename(i).p2f.^2));
        filename(i).pdiffrms =
sqrt(mean(filename(i).pdiff.^2))/sqrt(2);

    i
end
% Builds a table of the rms values.
RMS = zeros(n,13);
for i = 1:n
        RMS(i,1) = filename(i).ua1rms;
        RMS(i,2) = filename(i).ua2rms;
        RMS(i,3) = filename(i).vel1rms1000;
        RMS(i,4) = filename(i).vel2rms1000;
        RMS(i,5) = filename(i).disp1rms1000;
        RMS(i,6) = filename(i).disp2rms1000;
        RMS(i,7) = filename(i).flowrms;
        RMS(i,8) = filename(i).p1rms;
        RMS(i,9) = filename(i).p2rms;
        RMS(i,10) = filename(i).pdifrms;
        RMS(i,11) = filename(i).p1frms;
        RMS(i,12) = filename(i).p2frms;
        RMS(i,13) = filename(i).pdiffrms;
end
```

# Appendix B: MatLab Ã Code

The following code was used to calculate the normalized PSD of the pipe acceleration time series (*Ã*).

```
clear; %close;

n = 24; % number of files

%Naming Convention: E:\Pipe diameter and schedule\Baffle plate case and
%units acceleration is measured in\Which LabView VI was used\Wall
support
%locations_Accelerometer
% locations\PipeDiameterPipeSchedule_PumpSpeed_0001.txt
intro = 'E:\4 inch Schedule 40\No Baffle Plate Accel in Gs\New
VI\Quarter Wall Support_A1_0.125_A2_0.0625\4in40_';

samples = 50000;
time = 1/5000;
sampfreq = 5000;
for i = 8
    for j = 1:5
        istring = int2str(2*(i-1));

        if 2*(i-1) < 10
            filename(i).name =
strcat(intro,'0',istring,'Hz_0001','.txt');
        else
            filename(i).name = strcat(intro,istring,'Hz_0001','.txt');
        end
        Data = load(filename(i).name);


    filename(i).tyme=Data(:,1);

%     Breaks data into 2 second chunks
    filename(i,j).ua1=Data(10000*j-9999:10000*j,2);

    %    Calculates RMS values of the chunks
    filename(i,j).ua1std=std(filename(i,j).ua1);
    filename(i,j).ua1norm = filename(i,j).ua1/filename(i,j).ua1std;
```

```
%     FFT of the acceleration
% Takes the FFT of each chunk
    filename(i,j).afft = abs(fft(filename(i,j).ua1norm));

%     Calculates the PSD of each chunk.
    filename(i,j).apsd = (filename(i,j).afft).^2;

    freq = 0:1/2:5000/2-1/2;

%     Averages the FFT of each chunk
    filename(i).afftavI = mean(filename(i,j).afft,2);
    filename(i).afftav = filename(i).afftavI(1:5000);

%     Averages the PSD of each chunk
    filename(i).apsdavI = mean(filename(i,j).apsd,2);
    filename(i).apsdav = filename(i).apsdavI(1:5000);
    filename(i).apsdavnorm =
filename(i).apsdavI(1:5000)/(length(filename(i).apsdav))^2;
    end

%     Parseval's Theorem, integrating the PSD and dividing by the
length of
%     the PSD. This normalized integral should be equal to 1.

    filename(i).IntPSDav =
sum(filename(i).apsdavI)/((length(filename(i).apsdavI))^2);
    Parseval = filename(i).IntPSDav
end


% Plots the PSD

figure
loglog(freq(1:5000),filename(8).afftav(1:5000),'r-')
hold on
loglog(freq(1:5000),filename(8).apsdav(1:5000),'g-')
% loglog(freq2,respfftave(1:size(freq2,1)),'b-')
hold off
```

# Appendix C: Pipe Scaling Estimations

The following document outlines how pipe displacement, velocity, and acceleration fluctuations are expected to scale with various fluid and pipe characteristics. The first segment of the document assumes elastic behavior in bending of the pipe due to unsteady loading. The second segment assumes that the pipe is constrained from bending, as a buried pipe. This document was developed by Maynes [21].

[redacted]

$$\frac{V_p'}{V_f} \sim \left(\frac{V_f}{\sqrt{E/\rho}}\right)\left(\sqrt{\beta}\right)\left(\frac{DL}{\sqrt{I}}\right) \tag{5}$$

Note that the final four terms in Eq. 5 are all dimensionless and each represents physically important ratios. The parameter $\beta$ is the ratio of fluid mass per unit length to the total mass per unit length of the combined fluid and pipe ($\beta = \rho A \big/ \left(\rho A + m_{pipe}\right)$.

The fluctuations in the pipe wall acceleration ($A'$) will scale with the pipe wall velocity fluctuations multiplied by the natural frequency of vibration. Upon substitution one obtains the following scaling for $A'$

$$A_p' \sim \left(\frac{V_f^2 \beta}{L}\right) \text{ or } \frac{A_p' L}{V_f^2} \sim \beta \tag{6}$$

Results from previously obtained data are compared to this expression in the figure below. The data correspond to flow through 4 pipes of three different materials.

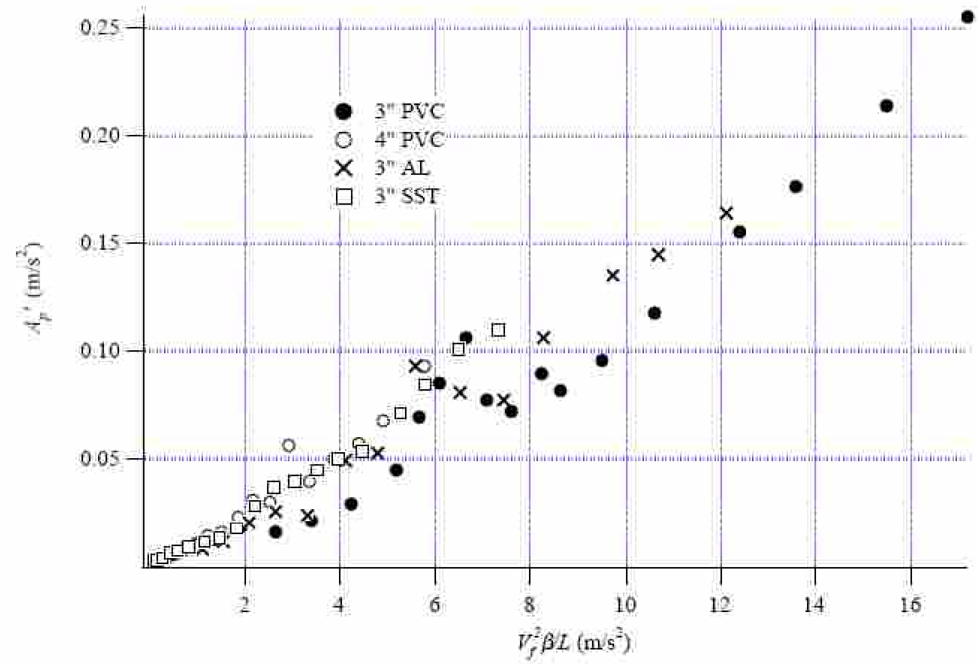

***Expansion/Compression Mode***

Reconsider the scenario described only now for the situation where the pipe is constrained from bending (i.e. buried). Classical analysis of this scenario shows that the fluctuations in the outer pipe wall should be

$$\delta_p{}' = \frac{R_i^2 R_o P_i'}{\left(R_o + R_i\right)tE} \tag{7}$$

where $R_o$ and $R_i$ are the outer and inner radii of the pipe. In the limit as the pipe wall becomes thin compared to the radius and $R_i \approx R_o \approx R$

$$\delta_p{}' \approx \frac{R^2 P_i'}{2tE} \tag{8}$$

Again assuming that the pressure fluctuations will scale (to a first order) with the square of the fluctuations in the velocity field, multiplied by the fluid density (i.e. turbulent dynamic pressure), $P' \sim \rho V'^2$ yields

$$\delta_p{}' \sim \frac{D^2 \rho V_f^2}{tE} \text{ or } \frac{\delta_p{}'}{D} \sim \frac{V_f^2}{E/\rho}\frac{D}{t} \tag{9}$$

A first order force analysis also suggests that the fluctuations in acceleration of the pipe wall (multiplied by the mass of the pipe and containing fluid) should scale directly with the pressure fluctuations (multiplied by the area over which they are acting $DL$)

$$A' \sim \frac{P'D}{m} \tag{10}$$

$$A' \sim \frac{\rho V_f^2 D}{m} \text{ or } \frac{A'D}{V_f^2} \sim \beta \tag{11}$$

Assuming that the fluctuations in the pipe wall velocity will scale as the product of $\delta'$ and $\omega_n$ ($V_p{}' \sim \delta'\omega_n$) where $\omega_n \sim \sqrt{tE/Dm}$ for the radial mode yields the following

$$V_p{}' \sim \frac{V_f^2}{\sqrt{E/\rho}}\sqrt{\beta}\sqrt{D/t} \text{ or } \frac{V_p{}'}{V_f} \sim \frac{V_f}{\sqrt{E/\rho}}\sqrt{\beta}\sqrt{D/t} \tag{12}$$

The variables are defined as:

$D$ – Pipe internal diameter (m)
$R_i$ – Inner pipe radius (m)
$R_o$ – Outer pipe radius (m)

t = Pipe wall thickness (m)

L = Pipe length between supports (m)

F = [illegible] (N)

D = Pipe [illegible] (m)

ρ = Fluid density (kg/m³)

[illegible]

[illegible]

m = [illegible] pipe per unit length (kg/m)

[illegible] of the pipe [illegible]

Observations

1. Regardless of the mode considered [illegible] dependence.

2. Regardless of the mode considered [illegible]

3. Regardless of the mode considered [illegible] The dependence [illegible] slightly [illegible]

4. Regardless of the mode considered [illegible] The [illegible] pipe diameter [illegible]

5. The length of the pipe between supports is quite important [illegible] the bending mode [illegible] The dependence on [illegible] highly constrained pipe [illegible] greater [illegible]

Results from the Literature

Many years ago (1960's) there was a significant amount (6 independent studies) of related work that was performed with one major difference. It addressed turbulent flow parallel to cylinders with the flow on the outside of the cylinders (rather than inside a pipe). Although there is significant problem with all of the correlations developed by previous investigators (primarily due to the fact that dimensional homogeneity is not maintained and exponents were varied indiscriminately) many insights are gained by the several investigators conclusions and are of relevance to the present work. Specifically correlations were developed that correlated the rms of the cylinder displacement to the variables $\rho$, $V_f$, $D$, $m$, etc. The exponent range for each variable and average value of the exponent from these previous works were as follows:

$\rho$ - Ranged from 0.0 to 1.0 with several investigators (3) placing the value at 1.0. The scale analysis here suggests a value of 1.0.

$V_f$ – Ranged from 1.5 – 2.6 with an average value of 1.98. The scale analysis here suggests a value of 2.0.

$D$ – Ranged from -0.5 to 2.2. Only one investigator suggested a negative value and the average value of the others was 1.4. The scale analysis here suggests a value of 2.0

$m$ – Ranged from -0.25 – -1.0. The scale analysis here suggests a value of 0 with regard to displacement

The bulk Modulas, $E$, was not considered, nor was the thickness of the cylinder wall in these previous studies of slightly different flow configuration.